INFORMATION TO USERS

This manuscript has been reproduced from the microfilm master. UMI films the text directly from the original or copy submitted. Thus, some thesis and dissertation copies are in typewriter face, while others may be from any type of computer printer.

The quality of this reproduction is dependent upon the quality of the copy submitted. Broken or indistinct print, colored or poor quality illustrations and photographs, print bleedthrough, substandard margins, and improper alignment can adversely affect reproduction.

In the unlikely event that the author did not send UMI a complete manuscript and there are missing pages, these will be noted. Also, if unauthorized copyright material had to be removed, a note will indicate the deletion.

Oversize materials (e.g., maps, drawings, charts) are reproduced by sectioning the original, beginning at the upper left-hand corner and continuing from left to right in equal sections with small overlaps. Each original is also photographed in one exposure and is included in reduced form at the back of the book.

Photographs included in the original manuscript have been reproduced xerographically in this copy. Higher quality 6" x 9" black and white photographic prints are available for any photographs or illustrations appearing in this copy for an additional charge. Contact UMI directly to order.

UMI

A Bell & Howell Information Company
300 North Zeeb Road, Ann Arbor MI 48106-1346 USA
313/761-4700 800/521-0600

INVESTIGATION OF THE NUCLEAR EQUATION OF STATE AND DIELECTRON PRODUCTION IN HEAVY ION COLLISIONS

Jianming Zhang

Physics Department
McGill University
Montréal

A thesis submitted to the Faculty of Graduate Studies and Research in partial fulfillment of the requirements for the degree of Doctor of Philosophy.

Nov 4, 1996

0-612-30428-0

Abstract

Several investigations involving strongly interacting matter at high temperature and density are pursued. First concentrating on relativistic heavy ion collisions slightly below the GeV/nucleon range, we perform studies of the equation of state (EOS) for nuclear matter. The non-equilibrium aspects of such collisions are simulated by the Boltzmann-Uehling-Uhlenbeck transport model with a momentum-dependent nuclear mean field. The EOS effects on the collective flow observables and dielectron spectra have been systematically and quantitatively examined by comparing with the experimental data gathered by the DIOGENE, Streamer Chamber, Plastic Ball, EOS TPC, E848H and DLS collaborations. The importance of the precise functional dependence of the nuclear mean field on the particle momentum, and the compressibility coefficient K of the nuclear matter are addressed. Using a simple coalescence model, we show that a quantitative connection between the composite flow and K can be established. In such nucleus-nucleus collisions, we also consider and discuss lepton pair production mechanisms. These include nucleon-nucleon bremsstrahlung, Δ decay, η decay, and pion-pion annihilation. We then turn to lepton pair production in ultrarelativistic heavy ion collisions. We concentrate on pion-pion virtual bremsstrahlung in the soft limit $M < 300$ MeV, and we make a quantitative comparison of various soft-photon-approximation(SPA) formulae with a full one-boson-exchange(OBE) calculation.

Résumé

Nous faisons plusieurs études concernant la matière en intéraction forte à des températures et des densités élevées. Nous étudions tout d'abord l'équation d'état de la matière nucléaire, en considérant les collisions d'ions lourds aux énergies intermédiaires. Les aspects hors d'équilibre sont inclus dans un modèle de transport dit de Boltzmann-Uehling-Uhlenbeck. Nous déterminons les effets de l'équation d'état sur les observables de flot collectif en examinant des résultats d'expériences faites par les collaborations DIOGENE, Streamer Chamber, Plastic Ball, EOS TPC et E848H. Nous établissons un lien quantitatif entre le flot des noyaux légers et le coefficient de compressibilité de la matière nucléaire. Nous abordons ensuite le phénomène de la production de paires de leptons et nous comparons avec des résultats de l'expérience DLS, réalisée au Bevalac. Finalement les collisions d'ions lourds aux énergies ultrarelativistes sont examinées. A ces énergies nous nous intéressons aux mécanismes de production de paires de leptons de petite masse invariante. Plus particulièrement, les résultats d'un calcul exact de bremmstrahlung pion-pion dans un modèle d'échange de bosons sont comparés à ceux obtenus dans plusieurs types d'approximations dites des photons mous.

Preface

I am especially grateful to my supervisor Professor C. Gale, not only for suggesting the topic of this thesis but also for his patient guidance and encouragement. Without his always available help this work would have been impossible. I also highly appreciate the stimulating discussions, encouragement and guidance from Professor S. Das Gupta. I am particularly thankful to Professors J. Barrette, S.K. Mark and N.B. de Takacsy for their encouragement. The useful communications and discussions I have had with Drs. J. Carroll, P. Danielewicz, H. Eggers, K. Haglin, M.M. Htun B.K. Jennings, B. Kamal, D. Keane, R. Madey, V. Metag, J. Pan, Q. Pan, J. Porter, G. Roche, D. Seibert, I. Towneri, K. Wilson and W.M. Zhang are also appreciated.

I am indebted to all my colleagues and staff who have made my stay at McGill University memorable. In particular J. Anglin, M. Chiao, Y. Dai, Y. Feng, O. Hamadi-Ravari, A. Hares, M. Kamela, I. Kvasnikova, G. Michaud, D. Persram, J. Peralta, Y. Qi, C. Roderick, and R. Tabti. I should like to thank N. Brown and P. Domingues for all the assistance they provided, and J. Gallego and P. Mercure for bearing my heavy computer uses.

I also would like to express my gratitude to my wife, Shu, for her patience, constant help and endless encouragement.

Statement of Originality

This thesis is divided into four chapters. Chapter 1 is a general introduction. Chapter 2 discusses the relationship between the baryon flow and the nuclear equation of state in heavy ion collisions. The material covered in this chapter represents original contribution from four papers: J. Zhang, S. Das Gupta, and C. Gale, Phys. Rev. **C 50**, 1617-1625 (1994); J. Zhang and C. Gale, Phys. Rev. **C 51**, 1425-1432 (1995); W.M. Zhang, R. Madey, J. Schambach, M. Elaasar, D. Keane, B.D. Anderson, A.R. Baldwin, J.W. Watson, G.D. Westfall, G. Krebs, H. Weiman, J. Zhang and C. Gale, Phys. Rev. **C 52**, 2643-2651 (1995); and M.M. Htun, R. Madey, W.M. Zhang, M. Elaasar, D. Keane, B.D. Anderson, A.R. Baldwin, J. Jiang, A. Scott, Y. Shao, J.W. Watson, K. Frankel, L. Heilbronn, G. Krebs, M.A. McMahan, W. Rathbun, J. Schambach, G.D. Westfall, S. Yennello, C. Gale and J. Zhang. submitted to Physics Review C (1996). All the calculations included in this chapter were done by myself. Professor C. Gale provided guidance and some verification of results. The experimental group at Kent State University provided me with detailed information about E848H data. Chapter 3 studies dielectron production in nucleus-nucleus collisions at DLS energies. The material there also is original. The derivation of the formulae and the calculations were done by me. Some nucleon-nucleon bremsstrahlung results are from the paper: J. Zhang, R. Tabti, C. Gale, and K. Haglin, Int. J. Mod. Phys. E, in press. Chapter 4 contains pion-pion virtual bremsstrahlung. This work was done by myself.

Contents

Chapter 1

Introduction

It is fair to say that the field of heavy ion collisions is a flourishing area of contemporary research in physics. In its higher energy extension, it straddles high energy and nuclear physics. The main objectives there are to create higher energy densities than ever attained in terrestrial accelerators before. In this pursuit, one will surely learn a great deal about the behavior of strongly interacting matter at high temperatures and densities. Ultimately, one will want to verify experimentally one of the most intriguing predictions of QCD: the formation of a plasma of quarks and gluons, deconfined over macroscopic portions of time and space. A vigorous experimental program is presently under way and the theoretical interest, both direct and indirect, being generated is considerable [1, 2, 3].

Heavy ion collisions can roughly be divided in a few broad regions, depending on the physics goals being pursued. The theoretical methodology and collision mechanism also vary from one region to the other. In the so-called intermediate energy regime (from $\approx$ 100 MeV/nucleon to a few GeV/nucleon), one main axis of research consists of the investigation of complex nuclear reaction dynamics. As one goes beyond the Fermi energy in kinetic energy per projectile nucleon, the phase space accessible to nucleons in microscopic two-body collisions opens up dramatically, owing to the disappearance of Pauli blocking effects. This area thus offers the intriguing possibility of studying the competition and the individual effects of the nuclear mean field and two–body collisions. In other words, the intermediate energy region stretches from a domain where mean field dynamics dominate to a regime where microscopic nucleon-nucleon collisions play a major role. One of the main goals of this line of research is an accurate determination of the bulk properties of nuclear matter as characterized by the nuclear equation of state (EOS). The EOS plays a crucial role in the dynamics of heavy ion collisions and also has a major influence in the theory of supernovæ explosions and neutron star properties. One realizes the many facets of the nuclear EOS, thumbing through the proceedings of recent dedicated conferences [4]. Information on the EOS, as characterized generally by the coefficient of compressibility for nuclear matter in its ground state, K, can also be deduced from detailed Hartree–Fock plus RPA analyses of giant monopole resonances in finite nuclei [5]. These lower energy experiments probe regions of excitation energy adjacent to the nuclear ground state while intermediate energy heavy ion collisions will create zones of high density and temperature. Consistency requires that the value of the nuclear compressibility coefficient of equilibrium nuclear matter deduced from both sets of experiments be compatible with one another. Happily, after a period of apparent disagreement, this goal seems on the verge of being fulfilled. It now seems that the analysis of giant monopole resonances and of heavy ion flow data can both accommodate a value of $K \approx 210$ MeV [6, 7]. We will elaborate in detail on this in the current thesis.

The extraction of the nuclear EOS from heavy ion flow data at the microscopic level is normally based on the Boltzmann-Uehling-Uhlenbeck(BUU) transport equation [8]. This one-body theory includes the effects of Fermi motion, the nuclear mean field, nucleon-nucleon collisions and Pauli blocking, and has been quite successful in modeling the six dimensional one-body phase space distribution and its time evolution. In the next chapter, we will systematically establish a relationship between the so-called flow observables and the nuclear EOS within this model. Note in passing that the BUU equation without its hard collision component is often called Vlasov equation [8], and without the mean field, Pauli blocking and Fermi motion is labeled the intranuclear cascade model [9]. As we will see, the produced flow from BUU is not a simple matter of the sum of the Vlasov contribution and the cascade contributions.

During nucleus-nucleus collisions, the initial longitudinal energy of the projectile nucleus is converted into thermal and compression energy by the nucleon-nucleon collisions and the nuclear mean field. The collided nuclei are compressed and heated. At the intermediate energy regime, the nuclear density may reach values of more than three times equilibrium nuclear matter density. After the nuclear matter reaches the highest density and temperature, it then expands and cools down. The energy is carried partly in the nuclear flow, and partly by the emission of secondary particles, such as pions, etas, direct photons, dileptons, kaons etc.. These particles represent probes of the collision dynamics and will carry important information about the compressed nuclear matter. A lot of effort has been devoted to this subject in the past decade. A detailed description can be found in several recent review papers [10, 11]. In this work, we will discuss the production of dileptons, together with the creation of other particles, such as pions and etas.

Dileptons are pairs of particles interacting via the electromagnetic interaction: once they are produced, they will not be affected much by final state interactions. Thus, they can directly go from the produced point to the detector. This unique property [1] implies that by studying dileptons, we may be able to understand the history of the whole collision process, especially in the earliest and hottest stages. The production rates are maximum in the hot and dense phases.

It is of high interest to try and understand theoretically the lepton spectra measured by the DLS collaboration at energies around, and less than, 1 GeV/nucleon. This statement is true for several reasons. First, a quantitative connection between the high density EOS and the measured spectrum of produced electron-positron pairs is still lacking. Second, a recent re-analysis of the dielectron spectrum produced in Ca + Ca collisions at 1 GeV/nucleon shows that the previously released data needs to be scaled upwards by a factor of roughly 6 [12]. Finally, some previous calculations [13, 14, 15] have been able to reproduce the old data, but some assumptions need to be clarified and the recent data certainly needs to be considered. We feel that a careful study of the dielectron production

---

[1] Photons also have this property.

mechanisms, combined with our state-of-the-art BUU modeling can fill this gap. The first iteration of such a calculation is presented in chapter **3**. It is also extremely relevant for the HADES experiment, in construction at the GSI. The motivation of the HADES experiments is to understand possible in-medium modifications of vector meson properties by measuring leptons. It may well be that nuclear collisions in the GSI energy range represent an arena of choice for such manifestations, as relatively high baryon densities can be attained while the dynamics are still within the realm of BUU approaches.

In the ultrarelativistic energy domain, a qualitative picture of lepton pair production can be drawn as follows: for dilepton invariant mass $M > m_{J/\Psi}$, the spectrum is dominated by Drell-Yan production [16], with a contribution from $D\bar{D}$ decays [17]. The spectrum around $M \approx 1$ GeV is dominated by the radiative and direct decays of ρ, ω and ϕ, while two-body [18] and many-body reactions [19] will also have contributions in this region. For the so-called soft dileptons [20], $M < m_\rho$, the dominating sources are Dalitz decay, and virtual bremsstrahlung from meson-meson reactions. If there is a phase transition from the hadron matter to quark matter, the quark interactions may contribute to this region as well. On the final part of this work, we will focus on pion-pion virtual bremsstrahlung in the soft dielectron limit $M < 300$ MeV. Note that the dynamics of collisions at these energies is meson dominated.

In hadron-hadron collisions, bremsstrahlung is usually calculated with the soft photon approximation(SPA). In this limit, the radiation from the external legs of Feynman graphs dominates the bremsstrahlung amplitude. At the energies we are interested in, we need to study corrections to this approximation. Different formalisms have been developed to study real situations [21]. As a fundamental physical rule, all the approximation formulae should satisfy symmetry requirements such as gauge-invariance and Lorentz-covariance. But for most formulae, it is not the case as pointed out by Lichard [21]. The basic Rückl formula [22] violates these requirements. We have compared [23] different formalisms for nucleon-nucleon bremsstrahlung. Our goal there is to investigate how good (or bad) the often-used Rückl formalism is, when we compare it with an approach that is acceptable in the appropriate limits and satisfies symmetry requirements. In the DLS energy regime, the Rückl approach has been compared with one-boson-exchange(OBE) model calculations for nucleon-nucleon reactions [24, 25, 26]. We will update this situation in chapter **3**. In chapter **4**, based on an OBE model, we have done a full-T-matrix calculation for pion-pion bremsstrahlung. The formalism will be clearly derived, and the assumptions and approximations used to recover the SPA formulae we used in chapter **3** will be clearly stated. The results of using different formulae will be compared. This is also relevant for the CERES experiments at the CERN SPS: before claims can be made about the modification of meson mass in the medium and the possible presence of the quark-gluon-plasma(QGP), background calculations have to be performed carefully. In chapter **5**, I will make a simple summary, followed by appendices.

Chapter 2

Collective Flow And The Nuclear Equation of State In Heavy-ion Collisions

2.1 Introduction

In the framework of heavy ion collision physics in the 100 MeV/nucleon $\sim$ 2 GeV/nucleon energy regime and its relation to the nuclear equation of state, the measurement and theoretical interpretation of collective flow observables have been vital [27]. Among the many models suggested to describe theoretically heavy ion collisions at such energies, the Boltzmann-Uehling-Uhlenbeck (BUU) approach has proven to be very successful [8]. In BUU simulations, nucleons can suffer hard collisions and can also move on curved trajectories, owing to interaction with the self-consistent nuclear mean field. The properties of the mean field are crucial to such calculations and can also be directly related to the nuclear equation of state. Some effort needs to be devoted to obtain realistic nuclear mean fields that can be used in practice within such numerical approaches.

Early on in microscopic analyses, it appeared that the data on nuclear flow, as characterized by transverse momentum plots [28, 29] and flow angle distributions [30] demanded an equation of state with a high compressibility coefficient (K $\approx$ 380 MeV) [31]. However, it was later shown that if a reasonable momentum dependence was introduced in the nuclear mean field, a lower compressibility would be favored in the interpretation of the experimental data [32, 33, 34, 35]. Finally, it is clear that the momentum dependence of the nuclear mean field is an unavoidable feature for a fundamental understanding of nuclear matter properties [36] and for the successful interpretation of current heavy ion data.

Additional properties of momentum dependent mean fields have also emerged in the BUU analysis of heavy ion collisions. Different sets of momentum dependent parametrizations sharing a common compressibility coefficient have been used. We will concentrate on two of those. We label them GBD [32] and MDYI [37], in accordance with the articles in which they have been introduced. Another momentum dependent potential used in one-body numerical simulations is associated with the Gogny interaction [38]. The properties of the GBD and MDYI potentials are somewhat similar in the ground state, but they will have different behaviors in actual dynamical situations [37, 39]. We shall discuss this aspect in the present work.

We have analyzed the quantitative differences between GBD and MDYI type approaches. We also give our own opinion as to which parametrization should be used in calculations where nonequilibrium effects can be important, as in intermediate energy heavy ion collisions. We further explore the impact of our conclusions on the determination of the nuclear EOS, by comparing with current pseudo-nucleon heavy ion data. We perform BUU calculations for symmetric and asymmetric projectile–target combinations, at various colliding energies. We also comment on the quantitative importance of angular momentum conservation as well as the Coulomb effects at the microscopic level in the interpretation of nuclear transverse momentum data.

Following Ref. [40], we further address the azimuthal distributions [37, 41] for free neutrons measured by the E848H collaboration [42, 43, 44] at the Bevalac. Calculations done with the BUU model [8] have reported that the azimuthal anisotropy ratio [37] was an observable sensitive to the value of K used in the theory. We will explore in this work the issue of the sensitivity of this particular observable to the nuclear equation of state. As the BUU is a one-body theory, we apply a simple phenomenological coalescence prescription to differentiate free particles and composites. The complexity in theory of the cluster formation will be also explored.

This chapter is organized in the following way. In the next section, we will give a very simple description of the BUU model. Following a detailed presentation of nuclear mean-fields used in the microscopic numerical calculations, section **4** is decidated to the evaluation of transverse momentum generation from several different sources. We then compare our results with experimental data for pseudo-nucleons in section **5**. After introducing the coalescence prescription in section **6**, we compare the simulation results to E848H free neutron data in section **7**. We also wish to provide a quantitative connection between composite flow and the coefficient of compressibility for equilibrium nuclear matter in the framework of the BUU model. This is presented in section **8**. We finally summarize.

2.2 The BUU microscopic Model

We study the dynamics of heavy ion collisions by use of the BUU transport equation:

$$[\frac{\partial}{\partial t} + (\frac{\vec{p}}{m} + \nabla_{\vec{p}} U(\vec{r},\vec{p}))\,\nabla_{\vec{r}} - \nabla_{\vec{r}}\, U(\vec{r},\vec{p})\nabla_{\vec{p}}] f(\vec{r},\vec{p},t) = I[f] \tag{2.1}$$

where $f(\vec{r}.\vec{p}.t)$ is a semi-classical phase space density. In this approach, the particles occasionally collide and in between collisions, they are propagated by solving Hamilton's equations:

$$\begin{aligned} \dot{\vec{p}} &= -\vec{\nabla}_{\vec{r}} U(\vec{r},\vec{p}) \\ \dot{\vec{r}} &= \frac{\vec{p}}{m} + \vec{\nabla}_{\vec{p}} U(\vec{r},\vec{p}) \end{aligned} \tag{2.2}$$

The $U(\vec{r},\vec{p})$ will affect the behavior of the particles and needs to be evaluated self-consistently. As mentioned previously, the one-body potential is phenomenological and will depend on the nuclear density as well as on the particle momentum. The various potentials, which may yield different nuclear matter equations of state, will be addressed in detail in the next section.

The effect of the two body collisions can be handled by considering the average rate of change of the occupancy f_1 at a given phase space point (r_1, p_1). It reads

$$I[f] = \int \frac{d^3p_2}{h^3} v_{12} \int d\Omega'_{12} \frac{d\sigma(12 \leftrightarrow 1'2')}{d\Omega'_{12}} (\bar{f}_1 \bar{f}_2 f'_1 f'_2 - f_1 f_2 \bar{f}'_1 \bar{f}'_2) \tag{2.3}$$

where a Pauli blocking factor $\bar{f}(r,p)$=1-$f(r,p)$ is included and v_{12} is the relative speed of the two colliding particles. The total elastic nucleon-nucleon cross section $\sigma(12 \leftrightarrow 1'2')$ is parametrized in the following way:

$$\begin{array}{ll} 55 \quad [mb] & for\ \sqrt{s} \leq 1.893 GeV \\ \frac{35}{1+100(\sqrt{s}-1.893)} + 20 \quad [mb] & for\ 1.893 < \sqrt{s} \leq 2.255 \\ \frac{17}{s-3.52} + 10 pace.2in [mb] & for\ \sqrt{s} > 2.255 GeV \end{array} \tag{2.4}$$

which is different from a previous parametrization [8]. The modification is motivated to improve the fit to data for kinetic energy over 1 GeV (see Fig. 3.8). For the inelastic total cross section, we use

$$\sigma^{in}_{nn\to n\Delta} = \frac{20(\sqrt{s}-2.015)^2}{0.015+(\sqrt{s}-2.015)^2} \quad if \sqrt{s} \geq 2.015 GeV \tag{2.5}$$

otherwise it is zero. And $\sigma^{in}_{n\Delta\to nn}$ is related to $\sigma^{in}_{nn\to n\Delta}$ by detailed balance, as described in the next chapter. In the collision term I[f], we include elastic collisions for NN→NN, $\Delta\Delta \to \Delta\Delta, N\Delta \to N\Delta$, and the inelastic reactions of N$\Delta \to NN, NN \to N\Delta$. The extension to handle the pions explicitly will be presented in the next chapter. The dynamical consequence on the collective flow of the pions will be also addressed there.

The BUU equation is solved numerically with a test-particle method. The initial momentum distributions of the test particles are determined by a local-density approximation. The dynamical evolution of the collisions is divided into time steps of length 0.3 fm/c. Within each time step, the elastic or inelastic collisions between the test particles are simulated by Monte-Carlo. The collision probability between two particles is proportional to the nucleon-nucleon cross section σ_{nn}. The density of final state is then inspected for Pauli blocking.

A alternative way to solve the BUU equation is the Lattice-Hamiltonian method developed by Lenk and Pandharipande [45]. This method can conserve the total energy exactly and currently is only used for momentum independent potentials. But with a momentum dependent potential, this method requires the calculation of an average density ρ_L at the sites of a six-dimensional lattice. The computer memory and the CPU time will increase drastically. For actual such simulations, this method currently is unpractical [46].

2.3 The Nuclear Equation of State(EOS)

As shown in appendix A, the nuclear potential is directly related to the nuclear equation of state. Since full G-matrix calculations are still absent for such a potential, different forms of phenomenological momentum dependent potentials are found in BUU applications. Gale, Bertsch and Das Gupta employed a parametrization of the potential energy density that can be written as [32]

$$V_{\mathrm{GBD}}\left(\rho(\vec{r})\right) = \frac{A}{2}\frac{\rho^2(\vec{r})}{\rho_0} + \frac{B}{\sigma+1}\frac{\rho^{\sigma+1}(\vec{r})}{\rho_0^{\sigma}} + \frac{C\rho(\vec{r})}{\rho_0}\int d^3p\,\frac{f(\vec{r},\vec{p})}{1+\left[\frac{\vec{p}-<\vec{p}>}{\Lambda}\right]^2} \tag{2.6}$$

The corresponding mean field is obtained by taking a functional derivative with respect to the single–particle occupation function; $U = \frac{\delta V}{\delta f}|_{\vec{p}}$. One then obtains

$$U_{\mathrm{GBD}}\left(\rho(\vec{r}),\vec{p}\right) = A\left(\frac{\rho(\vec{r})}{\rho_0}\right) + B\left(\frac{\rho(\vec{r})}{\rho_0}\right)^{\sigma} + \frac{C}{\rho_0}\int d^3p'\,\frac{f(\vec{r},\vec{p}\,')}{1+\left[\frac{\vec{p}\,'-<\vec{p}>}{\Lambda}\right]^2} + \frac{C}{\rho_0}\frac{\rho}{1+\left[\frac{\vec{p}-<\vec{p}>}{\Lambda}\right]^2}\,, \tag{2.7}$$

where $\vec{p}$ is the momentum of the particle, $<\vec{p}>$ is a local momentum average, and $f(\vec{r}.\vec{p})$ is the phase space occupation density . This quantity is normalized such that the nuclear density $\rho(\vec{r}) = \int d^3p\ f(\vec{r}.\vec{p})$. In cold nuclear matter, $f(\vec{r},\vec{p}) = (4/h^3)\theta(p_F - p)$ and $<p>=0$. In a collisional case, $f(\vec{r},\vec{p})$ will deviate from its zero temperature value. Thus

$$<\vec{p}>=\frac{\int d^3p\,\vec{p}\,f(\vec{r},\vec{p})}{\int d^3p\,f(\vec{r},\vec{p})} = \frac{\int d^3p\,\vec{p}\,f(\vec{r},\vec{p})}{\rho(\vec{r})} \tag{2.8}$$

will not in general be zero. There are five parameters to be determined in $U_{\mathrm{GBD}}(\rho(\vec{r}),\vec{p})$. Previously [32], one of them was chosen arbitrarily: the momentum scale $\Lambda = 400$ MeV. We require the following at the saturation density: (i) the effective mass m^*/m is set to 0.7 at the Fermi surface, and (ii) the total energy per nucleon is adjusted to reproduce the volume term of the semi–empirical mass formula, E/A = −16 MeV. We use $\rho_0 = 0.163\ fm^{-3}$ and thus obtain K = 215 MeV, for $\sigma = \frac{7}{6}$. This exponent has a large influence on K.

Some subsequent work by Welke et al. [37] used an improved functional

$$V_{\mathrm{MDYI}}(\rho(\vec{r})) = \frac{A}{2}\frac{\rho^2(\vec{r})}{\rho_0} - \frac{B}{\sigma+1}\frac{\rho^{\sigma-1}(\vec{r})}{\rho_0^{\sigma}} + \frac{C}{\rho_0}\int\int d^3p\, d^3p' \frac{f(\vec{r},\vec{p})f(\vec{r},\vec{p}\,')}{1+\left[\frac{\vec{p}-\vec{p}\,'}{\Lambda}\right]^2} \tag{2.9}$$

which leads to the other form of the momentum dependent potential we shall consider:

$$U_{\mathrm{MDYI}}(\rho(\vec{r}),\vec{p}) = A\left(\frac{\rho(\vec{r})}{\rho_0}\right) + B\left(\frac{\rho(\vec{r})}{\rho_0}\right)^{\sigma} + 2\,\frac{C}{\rho_0}\int d^3p' \frac{f(\vec{r},\vec{p}\,')}{1+\left[\frac{\vec{p}-\vec{p}\,'}{\Lambda}\right]^2}\ . \tag{2.10}$$

The five constants A, B, C, σ, and Λ in $U_{\mathrm{MDYI}}(\rho(\vec{r}),\vec{p})$ were set by demanding that, at saturation: E/A = −16 MeV, K = 215 MeV, the real part of the optical potential $U(\rho_0,\ p = 0) = -75$ MeV and $U(\rho_0,\ \frac{p^2}{2m} = 300\ \mathrm{MeV}) = 0$. It then follows that $U(\rho_0,\ p \rightarrow \infty) = 30.5$ MeV and that the effective mass $m^*/m = 0.67$, at the Fermi surface. The agreement of U_{MDYI} with the real part of the optical potential as extracted from experiment is remarkable, at both low and high energies [47, 48]. To clarify the origins of these parametrizations, we state here that a Yukawa interaction would have a mean field whose exchange term would be a momentum dependent expression of the MDYI type. The GBD energy density can be obtained from its MDYI counterpart by replacing $\vec{p}\,'$ in the denominator of the integrand of Eq. (2.9) by its average, $<\vec{p}\,'>$. The momentum dependent term of the MDYI mean field is attractive and important at low momentum, but it weakens and disappears at very high momentum. Even though both of the above parametrizations (GBD and MDYI) can share the same compressibility K, the quantities $U(\rho_0,\ p \rightarrow \infty)$ and the effective mass m* can be different. The value of $U(\rho_0,\ p \rightarrow \infty)$ has important consequences for the modeling of nuclear collisions at high energies, as we shall see.

In this work, for the sake of consistency and for the purpose of a quantitative comparison, we reset the five constants in our GBD and our MDYI potentials. The detailed procedure of the parametrizations is presented in appendix A. For both parametrizations we require that $\sigma = 12/11$, E/A = −16 MeV, $\rho_0 = 0.15\ fm^{-3}$, $U(\rho, p \to \infty) = 30.5$ MeV, and $m^*/m = 0.67$. We then obtain K = 210 MeV, for both potentials. We call these the new MDYI (NMDYI) and new GBD (NGBD), respectively, to distinguish these new parameter sets from the previous ones. We further note that both NGBD and NMDYI give a similar excellent fit of the optical potential (defined at saturation density), a desirable and important feature.

If one neglects the momentum dependent term, which means C=0, the mean field is a function of the nuclear density ρ alone. This simple Skyrme parametrization has the form (making the $\vec{r}$ dependence implicit):

$$U(\rho) = A\ (\frac{\rho}{\rho_0}) + B\ (\frac{\rho}{\rho_0})^{\sigma}\ . \tag{2.11}$$

We may thus further define two additional parameter sets. The first is a Hard potential (K = 373 MeV) and the second a Soft potential (K = 200 MeV). The parameters for the GBD, MDYI, NGBD, NMDYI, and momentum independent Hard and Soft potentials are summarized in Table 1, together with a hard MDYI potential(HM), which has K = 373 MeV. The parameters for the MDYI interaction with K=100, 150 and 250 MeV are also presented for completeness. Note that for all those potentials $P(\rho_0, T = 0) = 0$ and $E/A(\rho_0, T = 0) = -16$ MeV.

Fig. 2.1(a) shows the difference between the NGBD and NMDYI single–particle potentials. Both those potentials produce the same bulk nuclear matter properties at equilibrium. We plot the potentials as a function of wave vector k, for densities ranging from 0.1 to 0.5 fm^{-3}, in units of 0.1 fm^{-3}. Both potentials have a somewhat similar momentum dependence, but for higher densities the NGBD is more attractive at values of $k \leq k_F$ and notably more repulsive at $k \geq k_F$. We thus insist on the following important fact: even though the two interactions have an identical high–momentum behavior for $\rho = \rho_0$, the similarity in their asymptotic values is not guaranteed for densities other than equilibrium

Table 2.1: We write here the parameters and characteristics of the single–particle potentials we have introduced in the main text.

Model	A	B	σ	C	Λ	$m*/m$	$U(\rho_0,\infty)$	K
	(MeV)	(MeV)		(MeV)	(MeV)		(MeV)	(MeV)
Soft	−351.3	300	7/6	0		1	−51.3	200
Hard	−120.5	69.2	2	0		1	−51.3	373
GBD	−144.9	203.3	7/6	−75	400	0.7	−1.34	215
MDYI	−110.44	140.9	1.24	−64.95	415.7	0.67	30.5	215
NGBD	−227.5	347.7	12/11	−103.9	495.4	0.67	30.5	210
NMDYI	−322	352.5	12/11	−62.75	417	0.67	30.5	210
HM	−9.0	39.5	2.27	−62.75	417	0.67	30.5	373
MDYI1	66.13	−35.78	0.404	−64.95	417.5	0.67	30.5	100
MDYI2	146.6	−116.21	0.769	−64.95	417.5	0.67	30.5	150
MDYI3	−52.62	83.11	1.451	−64.95	417.5	0.67	30.5	250

nuclear matter density. The influence on the collective observables will be discussed in the following sections. As an additional comparison, we also show the momentum dependence of the GBD and NGBD parametrizations in Fig. 2.1(b). The two parametrizations yield almost identical compressibilities (c.f. Table 1), but the high momentum NGBD is much more repulsive owing mainly to its asymptotic optical potential: $U(\rho, p \to \infty)$. Also, comparing with Wiringa's microscopic calculations [49] one realizes that NMDYI is very close in behavior to that of the UV14 + UVII interaction, over a wide range of momenta and densities. On the other hand, the high momentum part of NGBD reaches values closer to that of the UV14 + TNI potential. The potentials described by Wiringa are known to provide a good description of light nuclei (they also can reproduce nucleon-nucleon scattering and few–body data) and bulk nuclear matter properties and have a nuclear compressibility K=210 MeV consistent with nuclear breathing mode analyses.

2.4 Transverse Momentum

One important technique proposed to quantify the flow of nuclear matter is the transverse momentum analysis [28]. The basic idea involves estimating the orientation of the

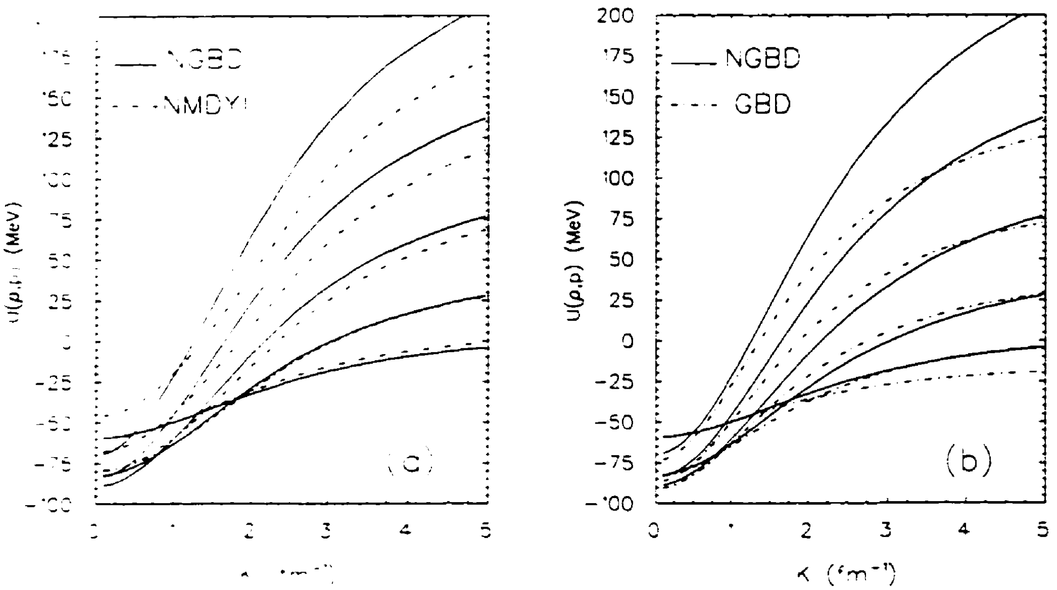

Figure 2.1 (a): A comparison of the momentum dependent NMDYI and NGBD potentials, adjusted to produce identical bulk properties in cold nuclear matter. The abscissa shows the wave number. Starting from the bottom, the different curves are for densities of 0.1, 0.2, 0.3, 0.4 and 0.5 fm^{-3}. (b): the same as in (a), but with the GBD and NGBD potentials.

reaction plane for each event by using the beam direction and the constructed vector $\vec{Q} = \sum_\nu \omega(y_\nu)\vec{p_{\nu\perp}}$, where $\vec{p_{\nu\perp}}$ is the transverse momentum of the νth outgoing particle, $\omega_\nu = 1$ for $y_\nu > 0$ and $\omega_\nu = -1$ if $y_\nu < 0$. Here y is the rapidity. Within each rapidity bin, the average transverse momentum $< P_x'(y_\nu) >$ in this estimated reaction plane is then defined as

$$< P_x'(y_\nu) >= p_\nu \frac{\vec{Q}_v}{|\vec{Q}_v|}, \qquad \vec{Q}_v = \sum_{\mu \neq \nu} \omega_\mu p_{\mu\perp} \tag{2.12}$$

The autocorrelations are removed by calculating $\vec{Q}_\nu$ individually for each particle without including that particle($\mu \neq \nu$). Since this estimated reaction plane is not the true reaction plane, the in-plane average transverse momentum $< P_x(y_\nu) >$ is obtained by correcting the measured value of the $< P_x'(y_\nu) >$ for dispersion [29] . In our theoretical calculations, the reaction plane is always known as the plane formed by the impact parameter (x-direction) and the beam direction (z-direction). This analysis method has also been used to clarify the transverse momentum generating features of different nuclear mean fields in the BUU approach to nucleus–nucleus dynamics. In the framework of such studies it has been shown that under certain circumstances, a soft momentum dependent potential can produce about the same transverse momentum as that of a hard momentum independent–interaction [32, 33]. In order to further highlight the behavior in a dynamical situation of the Hard, GBD, NGBD and NMDYI potentials, we plot in Fig. 2.2(a) the time evolution of the average transverse momentum for a symmetric Nb + Nb collision at projectile kinetic energy E = 400 MeV/nucleon at an impact parameter b = 2.1 fm. A sizeable difference in the saturated transverse momentum is observed. The hard momentum independent potential follows the behavior of the soft momentum dependent one quite closely, at this impact parameter. The asymptotic values of their average transverse momentum are only 4 MeV/c apart. We comment on the behavior of the momentum dependent interactions below.

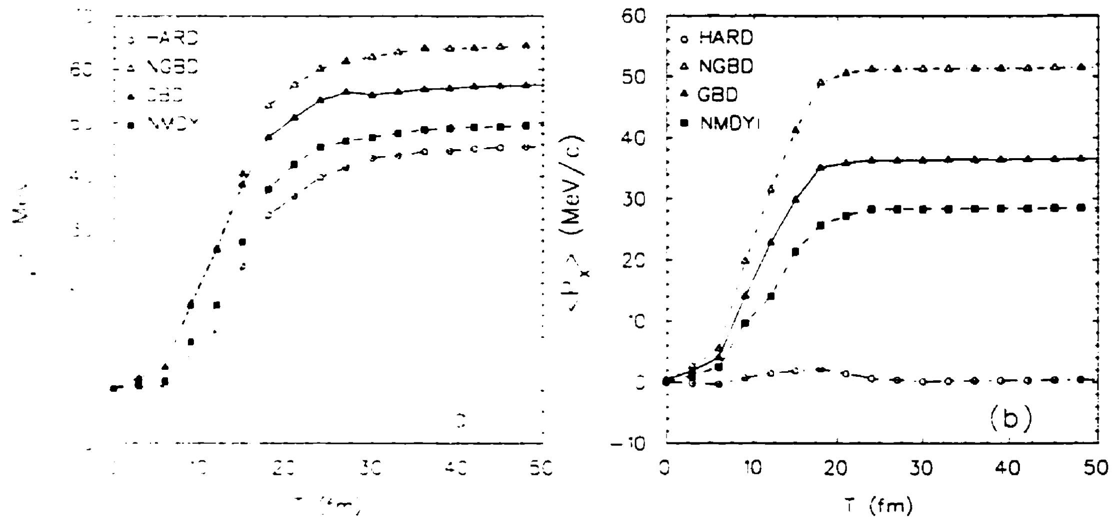

Figure 2.2: (a): Average in plane transverse momentum per nucleon versus time for BUU calculations; (b) Average in plane transverse momentum per nucleon versus time for Vlasov calculations; of Nb + Nb at 400 MeV/nucleon, at an impact parameter b = 2.1 fm. The results are for the Hard, GBD, NGBD and NMDYI potentials.

By setting the collision term in the BUU equation to zero, one can study the Vlasov behavior of the Hard, GBD NGBD and NMDYI potentials. From Fig. 2.2(b) one realizes that the momentum dependent single particle potentials alone can generate large transverse momenta, whereas the Hard potential can only yield very small transverse momenta. Comparing Figs. 2.2(a) and 2.2(b), we can further deduce another important fact: the role of hard two-body collisions is quite different, depending on whether the nuclear mean field is momentum dependent or not. Comparing the Hard and NMDYI potentials, the fraction of the net average transverse momentum generated by adding the collision term to the Vlasov equation is ≈ 100 % and ≈ 42 %, respectively. However, it is important to point out that the transverse momentum is generated by the nuclear mean field and the hard two body collisions in a highly non–linear fashion. From Fig. 2.3, the pure cascade simulation results, Figs. 2.2(a) and 2.2(b), one can readily deduce this important argument. Fig. 2.2(b) also tells us that, even though the GBD and NGBD potentials have the same functional dependence on momentum and almost identical compressibilities, they produce net transverse momenta that are very different from each other. As discussed in the above section, this result can be understood simply in terms of the different asymptotic values of the respective one–body potentials. Continuing our interpretation of the results in Fig. 2.2(b), we find the following interesting fact: the NGBD and NMDYI potentials produce average transverse momenta in the Vlasov model that differ by ≈ 10 MeV/c. Both these parametrizations share the same $U(\rho_0, \infty)$ and K. As mentioned previously, fitting the static nuclear matter properties and optical potential is not enough to predict unambiguously the consequences of the different interactions in nonequilibrium situations. It is also likely that realistic cases will also carry the added complication that

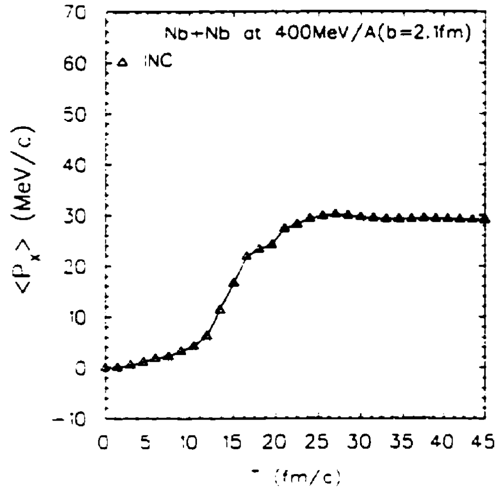

Figure 2.3: Average in plane transverse momentum per nucleon versus time for Cascade calculations of Nb − Nb collisions at 400 MeV/nucleon, at an impact parameter b = 2.1 fm

generally, $< \vec{p} > \neq 0$ in the GBD formulation of the one–body potential.

Fig. 2.4 shows the average in–plane transverse momentum, calculated in the BUU model, as a function of centre of mass rapidity. From this figure (a), it is also clear that NGBD is more repulsive than NMDYI. we also plot the results with the GBD and MDYI potentials in Fig. 2.4(b), and the GBD and NGBD results in Fig. 2.4(c). It shows that the GBD and MDYI potentials produce almost exactly the same results. The NGBD potential produces larger transverse momenta than the GBD potential. This feature has already appeared in both Figs. 2.2(a) and 2.2(b).

Another aspect we need to address here, is the importance of Coulomb effects. When the nuclei are large, such effects could play a large role in the heavy ion dynamics. To settle this issue, we solve the Poisson equation on a grid, using fast relaxation methods [50]. The results of our dynamic calculations, with and without the Coulomb interaction, are displayed in Fig. 2.5. One can see that the effect on transverse momentum, in the energy region relevant to our studies is not very important. Nevertheless, these factors need to be consistently taken into account. We do so in our calculations.

2.5 Comparison With Pseudo-nucleon Flow Data

2.5.1 Ar+Pb Data

In this section and the following, we compare BUU calculations with experimental data. We will first concentrate on values of the flow parameter F and transverse momentum distributions, as measured in asymmetric heavy ion reactions by the DIOGENE collaboration [51] and by the Riverside/GSI/LBL Streamer chamber group [52]. The flow parameter F is defined as

$$F = \left[\frac{d < P_x/m >}{dy} \right]_{y=y_0} . \qquad (2.13)$$

Here $< P_x >$ is the average value of the transverse momentum projection on the reaction plane and y_0 is the rapidity at the intercept: $< P_x >|_{y_0} = 0$. Since the experimental

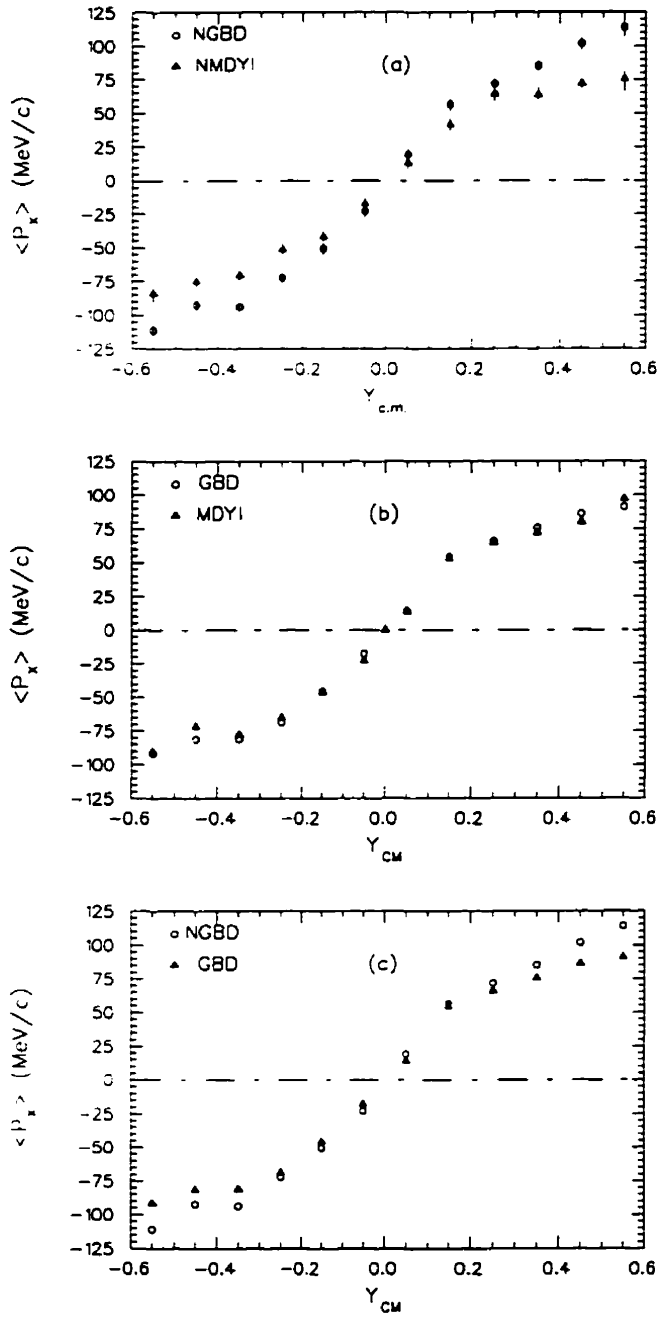

Figure 2.4: Average in plane transverse momentum distributions versus centre of mass rapidity for Nb + Nb for b = 2.1 fm and beam energy 400 MeV/nucleon. The results are (a) for the NGBD and NMDYI; (b) for the GBD and MDYI; (c) for the GBD and NGBD interactions.

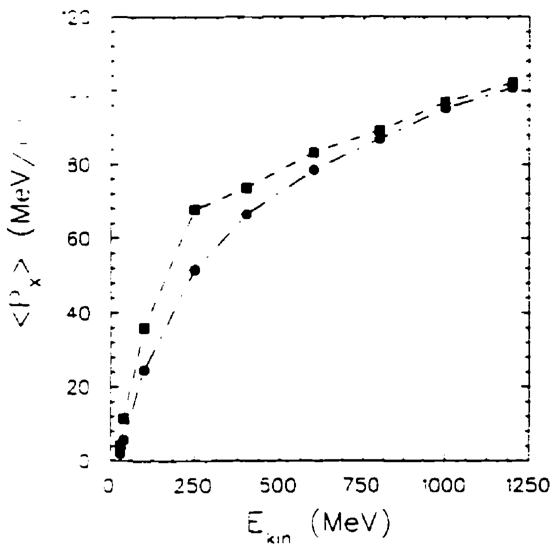

Figure 2.5: The average in-plane transverse momentum in the forward direction as a function of the kinetic energy for $^{197}Au + ^{197}Au$ collisions at impact parameter b=4.8 fm with NMDYI potential. The square and circle symbols represent with and without Coulomb effect, respectively.

[illegible] cuts influence the observables, corresponding restrictions have to be applied to the theoretical calculations in order to compare with measured values.

We first turn to measurements by the DIOGENE collaboration. There, the laboratory polar angle of the particles is limited to

$$20^\circ \leq \theta \leq 132^\circ \ . \tag{2.14}$$

The transverse momentum $P_\perp$ of the particles have to satisfy

$$P_\perp/m > 0.36 + 0.72y \qquad \text{if } y < 0 \tag{2.15}$$

$$P_\perp/m \geq 0.36 - 0.8y \qquad \text{if } y \geq 0 \ . \tag{2.16}$$

The measurements of rapidity distribution for "pseudo–protons" [1], around y_0 are plotted in Fig. 2.6 (a) for Ar – Pb at 400 MeV/nucleon at an impact parameter b=4.5 fm. Well-known geometrical arguments are used to estimate the impact parameter [53]. The data shows a linear rapidity dependence of $< P_x >$, in the interval [0, 1]. The flow parameter F is obtained by fitting the data to a straight line in the appropriate interval, as shown

---

[1] All protons, whether free or bound in clusters, are included.

on Fig. 2.6. The BUU calculations were performed with 120 parallel events to minimize numerical fluctuations, and with free space nucleon-nucleon scattering cross sections. We note in passing that since the two-body collisions contribute more to the transverse flow with a momentum independent potential than with a momentum dependent potential as discussed previously, this observable is not expected to be greatly sensitive to reasonable variations in the in-medium cross sections. To illustrate this point, compare Fig. 2.2(a) with Fig. 2.2(b).

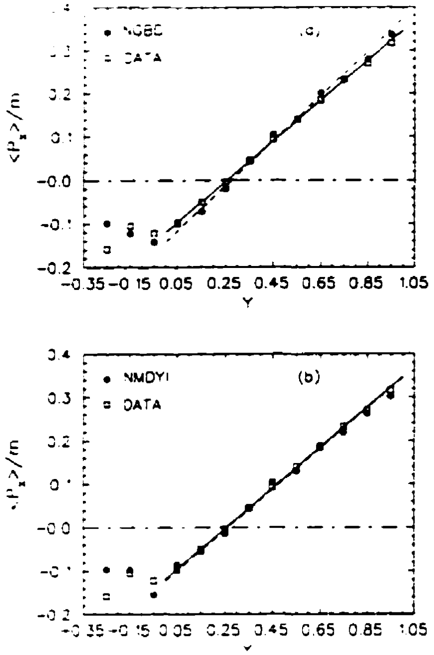

Figure 2.6: Average in plane transverse momentum (divided by the proton mass) as a function of rapidity in the Ar + Pb reactions at 400 MeV per projectile nucleon at an impact parameter b=4.5 fm. The solid and dashed lines represent linear fits through data[51] and calculation, respectively.

Our results also show that the transverse momentum $< P_x >$ depends linearly on the rapidity around $< P_x >=0$ with both NGBD and NMDYI potentials. Fig. 2.6 clearly shows this. The fit to the experimental data is quite good with both interactions. To increase data sensitivity to the model parameters, the extracted values of the flow parameter, F, are plotted as a function of the impact parameters b in Fig. 2.7, together with the relevant data. We see that the overall agreement is quite remarkable with the NMDYI potential whereas the NGBD potential gives a larger values than the experimental measurements. The momentum independent potential fails completely to reproduce the data. We show the important point that the asymmetric system can nicely separate out interactions of a similar compressibility but with a different momentum dependence. The results associated with the hard and soft interactions of the MDYI type do not differ much in this plot.

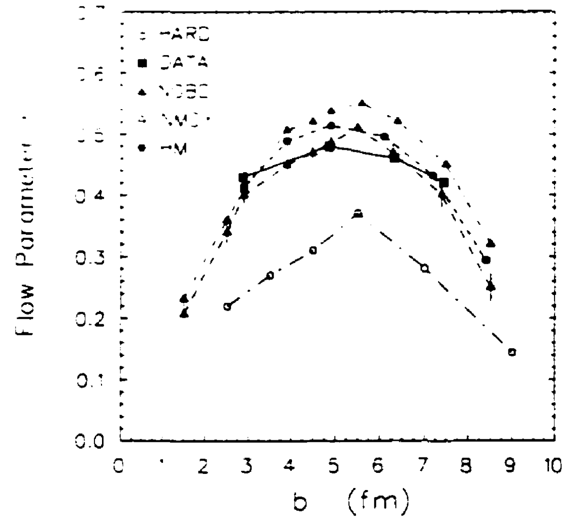

Figure 2.7: Impact parameter dependence of the flow parameter F for Ar+Pb reactions at 400 AMeV. The results of BUU calculations with different single particle potentials, Hard, NGBD, NMDYI and HM, are compared with the data of Ref. [51]. Error bars in the theory reflect statistical errors and are only given for one set of calculations.

Now we turn to rapidity distributions as measured by the Streamer Chamber. The results of the analysis are presented in terms of the mean in-plane transverse momentum for pseudo-protons as a function of normalized rapidity in Ar + Pb central collisions at 400 and 800 MeV/nucleon, respectively. Fig. 2.8 shows the calculation results of rapidity distributions with the NMDYI and NGBD potentials at 400 MeV/nucleon in comparison with the data. The behavior differs slightly from the common S shape [29] due to the asymmetry in collision geometry. It also differs from the linear DIOGENE data as the two detectors have widely different acceptances. In the calculation, the maximum impact parameter was evaluated within a geometrical clean cut model. Our calculations with the NMDYI potential reproduce the data very well. A considerably larger transverse momentum transfer was generated by the NGBD potential. In Fig. 2.9 we compare the results obtained with the two potentials with data obtained with the same projectile–

target combination, at 800 MeV/nucleon. We reach similar conclusions as in the 400 MeV/nucleon case.

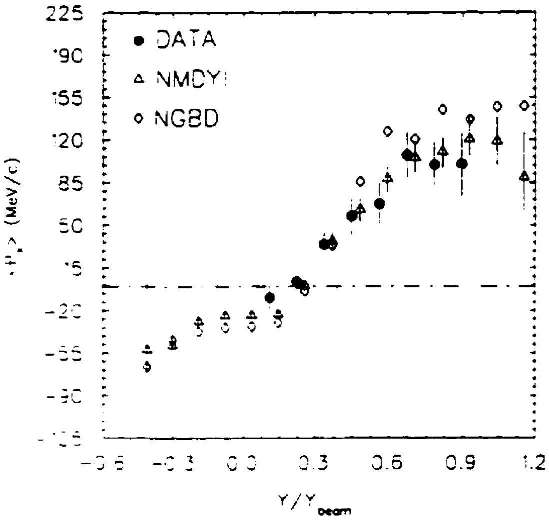

Figure 2.8: Average in plane transverse momentum as a function of normalized rapidity in central Ar + Pb collisions at 400 MeV per projectile nucleon. The data of Ref. [52] are compared with BUU calculations with the NMDYI and NGBD potentials. Errors bars in the theory reflect statistical errors only and are given for one set of calculations.

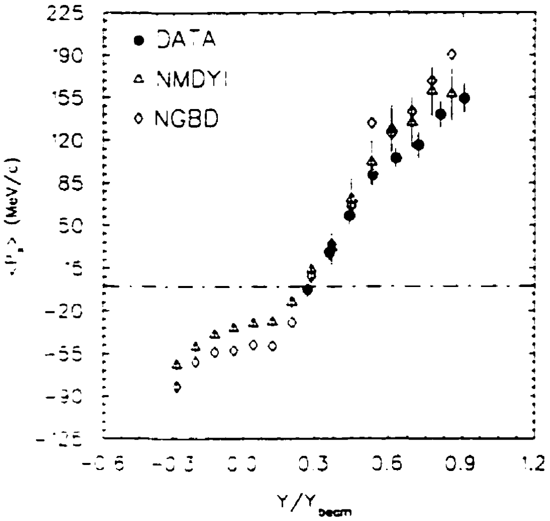

Figure 2.9: Same caption as in Fig. 2.8 but with incident kinetic energy 800 MeV/nucleon.

Fig. 2.10 presents the excitation function of the average in–plane transverse momentum in Ar + Pb collisions. The average transverse momentum per nucleon is evaluated from protons with rapidities in the c.m. system greater than 0.1, 0.15, 0.2 and 0.3 for beam energies 400, 800, 1200 and 1800 MeV/nucleon, respectively. The average BUU transverse momentum with the NGBD and hard MDYI(HM) potentials are much larger than the data. The only good fit is provided by the NMDYI potential. There, the agreement is striking at all energies. Again, a hard momentum independent potential is completely ruled out by this data.

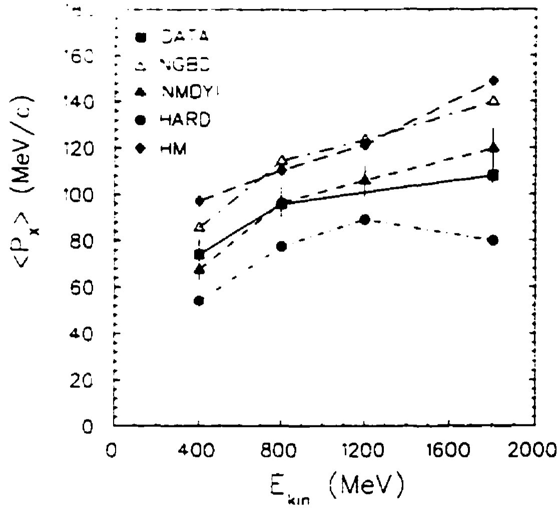

Figure 2.10: We plot the excitation function of the average transverse momentum per nucleon in the reaction plane for the forward centre of mass hemisphere as a function of beam energy for Ar+Pb reactions. The data of Ref. [52] are compared with the BUU calculations with the Hard, HM, NGBD and NMDYI potentials. Errors bars in the theory reflect statistical errors only and are given for one set of calculations.

Summarizing this section so far, we reproduce both the DIOGENE and the Streamer Chamber measurements quite well in terms of BUU microscopic simulations with the MDYI type momentum dependent potential, with a compressibility K = 210 MeV. A GBD type momentum dependent potential with the same K value is not so successful and a momentum independent interaction fails completely. The flow data for asymmetric systems is quite efficient in separating interactions that are momentum dependent from those that are momentum independent, even though their compressibility coefficient are the same.

2.5.2 Au+Au Data

EOS Flow Parameter F

We now turn to a set of data on symmetric systems [54], as measured by the EOS TPC Collaboration. Such data are of high quality, virtually free of experimental biases. The EOS Time Projection Chamber, with its simple and seamless acceptance, good particle identification and high statistics, was designed to overcome the limitations of the previous generation of 4π detectors. The Plastic Ball detector, even though having provided a seminal contribution to the field, had a complex acceptance that was not so easily simulated. The Streamer Chamber was somewhat limited by its particle identification capabilities. In the EOS TPC measurements we shall consider, all nuclear fragments species up to ^{4}He are included. The multiplicity trigger was set in order to select an interval centered about the value where the flow has its maximum. This multiplicity interval corresponds to baryon multiplicities $0.6M^{\max} \leq M \leq 0.9M^{\max}$. $M^{\max}$ is a value near the upper limit of the multiplicity spectrum where the height of the distribution has fallen to half its plateau value. In our BUU calculations, we have adjusted our impact parameter limits to reproduce the multiplicity cuts, in a geometrical clean–cut model. The integration was then carried out by sampling impact parameter values between those two limits. The data are in–plane transverse momentum measurements as a function of rapidity. The flow parameter F can then be evaluated. Fig. 2.11 shows the TPC data, together with our calculated results. Measurements were made for Au + Au at beam energies 250, 400, 600, 800 and 1200 MeV/nucleon. We display results of calculations with a soft (NMDYI) and a stiff (HM) momentum dependent potential. Calculations done with the NMDYI interaction reproduce the data exactly. Both the data and the results display that this flow parameter F from Au + Au symmetric systems is energy independent. It would be very interesting to see at higher energies, such as the AGS, if such a feature is still there. Since the HM potential produces much larger results, it shows that these symmetric EOS data have much larger sensitivity to the nuclear compressibility than the asymmetric Ar + Pb data.

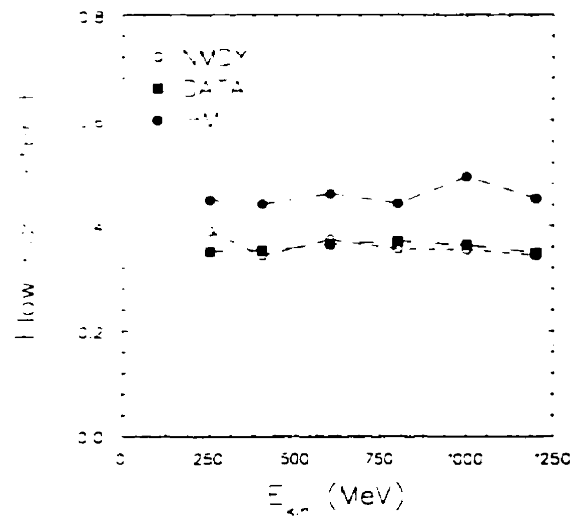

Figure 2.11: We plot the excitation function of the flow parameter F , where F is defined in the main text. The solid squares refer to Au + Au data as measured by the EOS TPC Collaboration [54], the circles are calculations done within the BUU approach, with a soft and stiff compressibility coefficient. The numerical uncertainties in the calculations are less than 10%, as previously.

Therefore, the different characters of the DIOGENE asymmetric data and the EOS symmetric data imply that the asymmetric systems may be used to appreciate the importance of the momentum dependence of the nuclear interaction. For the study of the nuclear compressibility, one needs to focus on symmetric systems. However, it is also very important to point out that at low energies, e.g. $E_{kin} < 150$ MeV, the flow parameter F derived from the symmetric systems may not discriminate between a soft (NMDYI) and hard(HM) nuclear equation of state, as displayed by Fig. 2.12. As at such low energies, the fragment contamination complicates the situation.

Angular Momentum Conservation

Au + Au is a reasonably large system and it might be that there exists effects that could safely be neglected for smaller nuclei at lower energies that are important here. It was brought up recently that an improvement in the angular momentum conservation in the microscopic models could perhaps lead to a re-evaluation of the role played by the nuclear mean field in generating transverse momentum in heavy ion collisions [55]. The

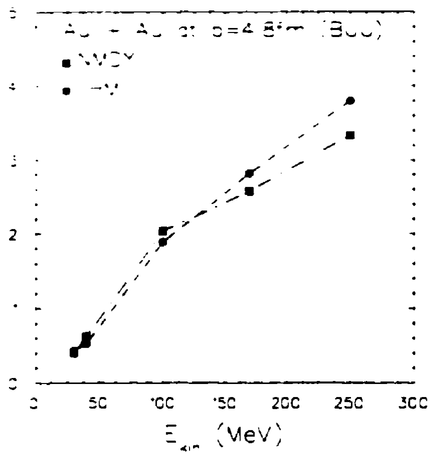

Figure 2.12: The flow parameter $F' = F \cdot (Y_{beam})_{cm}$ as a function of kinetic energy for NMDYI and HM potentials. The flow values are extracted from Au + Au collisions at the impact parameter b=4.8 fm with the rapidity coverage $(Y/Y_{beam})_{cm}$ from -0.4 to 0.4. The flow parameter F is defined in the text.

quantitative importance of conservation laws in microscopic models of heavy ion collisions has been investigated before [56, 57]. In the case at hand, the only difference might come from the fact that we are dealing here with very heavy systems at high energies. Thus the respective role played by two–body scattering and mean field effects might be modified. We have considered two independent algorithms. In the first approach, whenever two–body scattering occurred at the microscopic level we made sure that the direction of the reaction plane was unchanged in the centre of mass of the colliding nucleons. The other algorithm made sure that angular momentum was conserved *exactly*. The latter algorithm can however only be practically applied in a cascade calculation. This does not affect our general conclusion.

Fig. 2.13(a) displays the effects of reaction plane conservation on the results of BUU calculations. for Au + Au collisions at 1 GeV/nucleon. The impact parameter range and kinematical cuts were adjusted to match those of the TPC. Fig. 2.13(b) shows the consequences of reaction plane and exact angular momentum conservation on cascade simulations of the same nuclear reaction. The imposition of exact angular momentum conservation increases the flow parameter by roughly 23% in cascade simulations. We can also see that the dominant effect in angular momentum conservation comes from keeping the direction of the reaction plane constant in individual two–body collisions. In the BUU calculations, reaction plane constraints raise the flow by only 8%. The net effect on the transverse momentum can readily be appreciated in those two figures. Basically, the effect on BUU calculations is considerably smaller than in cascade approaches.

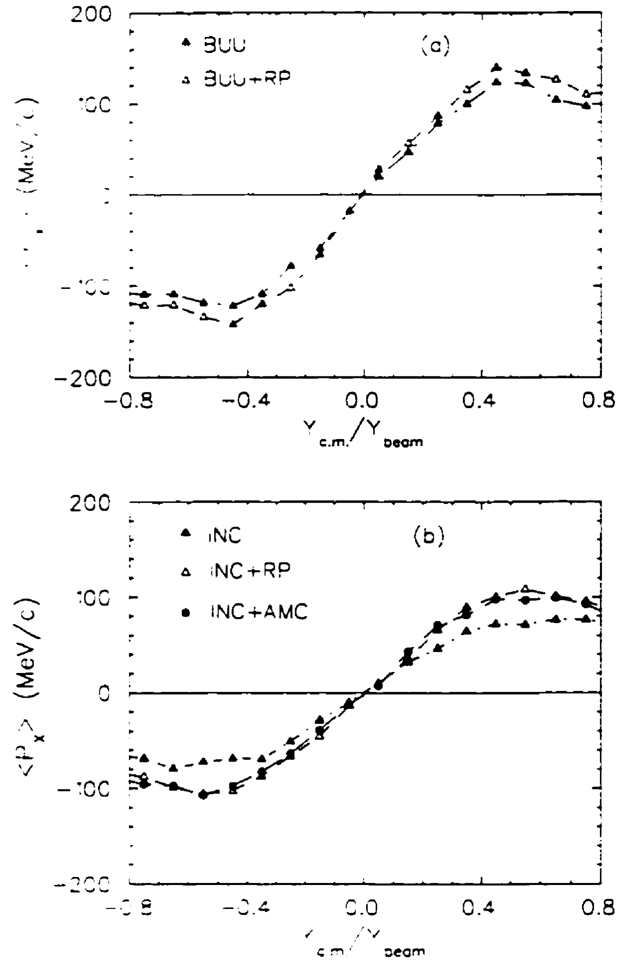

Figure 2.13: We plot the transverse momentum generated in Au + Au collisions at 1 GeV/nucleon against rapidity in the centre of mass. We investigate the consequences of (a) imposing a reaction plane (RP) on each two–body collision in the BUU model with the NMDYI momentum dependent potential and (b) reaction plane (RP) and exact angular momentum conservation (AMC) in a cascade approach.

Fig. 2.14 displays the actual collision numbers between nucleons during the dynamical process with each time step $\delta t = 0.3$ fm/c. From this figure, it is also clear that the effective nucleon-nucleon collisions are decreased by the imposition of the angular momentum conservation. This decrease is much more on the cascade simulations than in the BUU approaches with the NMDYI momentum dependent potential.

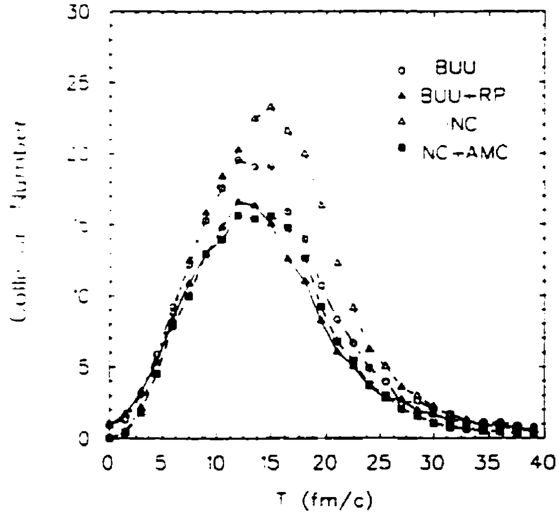

Figure 2.14: The effective number of nucleon-nucleon collisions within each time step δ = 0.3 fm/c during a Au + Au reaction at 1.0 GeV/nucleon and impact parameter b=4.8 fm. The consequences of the imposition of angular momentum constraints on the cascade simulations and BUU model with the NMDYI momentum dependent potential are shown.

2.6 BUU Model + Coalescence Prescription

More than ten years of calculation with the BUU transport model [58] have left no doubt on the complexity of nucleus-nucleus reactions at intermediate energy and on the need for a complete transport approach. As shown in the previous sections, the model has been quite successful in reproducing single particle flow patterns and transverse momentum distributions. However, the BUU equation is the representation of a one-body theory. It yields the time evolution of the *average* one-body density and consequently it is not well suited to describe aspects of nuclear reactions that deal with significant dynamical branching or fluctuations. Nuclear multifragmentation is a good example of this class of phenomena. A significant amount of theoretical activity has been devoted to incorporate the effects of fluctuations in the transport approaches. An attempt to extend the standard BUU in this direction was made recently [59]. Also, in an approach similar to the theory of hydrodynamic fluctuations, a Boltzmann-Langevin equation for the evolution of the one-body density was used [60]. A formalism for addressing stochastic one-body dynamics within the framework of transport theory was devised [61]. The above three techniques have been critically compared in a recent publication [62]. With the exception of the first approach, these scenarios are still not amenable to calculations that can directly be compared with experimental results. Some recent important developments involve the use of quantum many-body theory to derive transport equations with bound-state production and absorption [63, 64]. The work along these lines seems extremely promising.

Driven by the need to interpret the available experimental data in a plausible fashion, other more phenomenological avenues have been followed in the extraction of composite contributions from transport theory results. One simple and intuitively appealing approach relies on the idea of coalescence. This concept was introduced already long ago [65]. The original formulation for heavy ion collisions was devised around the thermodynamic model. Put simply, the picture stipulates that if two or more nucleons are close enough together in phase space when the momentum space configuration of the reacting system ceases to change, they will emerge as a self-bound cluster.

In performing theoretical analyses of intermediate energy heavy ion data and comparing the results of complete BUU calculations with measurements of single nucleon observables, the need to subtract the "spurious" (in this context) cluster contribution from the full simulation results has also arisen. Some early experimental measurements have concentrated on this independent cluster component. For example, the Plastic Ball group has observed relatively large triton yields in nuclear reactions at intermediate and high energies [66]. A coalescence prescription to study the transverse flow of intermediate mass fragments with a relativistic BUU model has been used previously and has been shown to provide a good description of the data [67]. At energies below and around 100 MeV/nucleon, a six-dimensional coalescence model has also been used to filter the results of VUU simulations and to very successfully compare with experimental results [68]. At such energies, the composite to free nucleon ratio is larger than at the energies we will consider here.

It is important to remember that a cluster is really an entity correlated in six-dimensional phase space. However, in view of the fact that our BUU approach contains a binding mean field interaction, we shall adopt a somewhat simpler viewpoint. It is well know from transport theory calculations that the transverse momentum generation in heavy ion reactions begins quite early in the history of the reaction and then stops. The amount of transverse momentum generated has then saturated and the momentum space distributions are approximately stable. Our idea is to apply a coalescence criterion in coordinate space only, at this point. Typical BUU calculations consist of several nucleus-nucleus collision events performed in parallel to enhance statistics and to provide a smooth initial state density profile in coordinate and momentum space [8][2]. The approach is then the following: within a given BUU event, a nucleon will be considered "free" only if no other nucleons are found within a certain critical three-dimensional distance, d_c. Otherwise, it will be considered a component of a bound cluster. We justify restricting our analysis to coordinate space by the fact that, owing to the dynamical nature of the problem and to single particle propagation in the self-consistent mean field, particles nearby in coordinate space but far apart in momentum space will separate after a certain time. There are two parameters to our scenario: the time at which the coalescence model is applied, t_c, and the critical distance parameter, d_c. We choose t_c as the time when the transverse momentum generation just starts to saturate. The value of the critical distance d_c is left as a free parameter and adjusted to experimental data (see next section). This coalescence picture is verified quantitatively in a more sophisticate approach, by spanning the momenta of the nucleons temporarily assigned to a cluster and by rejecting those for which it was kinematically impossible to belong to a common Fermi sphere. This last criterion brings modifications of the straight coordinate space picture at the level of less than 1%. We do recognize that the above simple criterion for clustering is approximate, nevertheless, it is verified to be quantitatively sound and it does provide a basis for adequate phenomenology.

---

[2] An alternate viewpoint is that each "physical" nucleon is represented by a number of "test nucleons" equal to the number of BUU events.

2.7 Comparisons With E848H Free-neutron Data

2.7.1 Double-differential Cross sections

Since the full one-body BUU theory considers all the nucleons whether free or bound in the clusters, to simulate the E848H free neutron data, the coalescence picture described in the above section has been applied to differentiate the free nucleons and the composite fragments. The value of the critical coalescence parameter d_c is determined such that the BUU simulation results with the NMDYI momentum dependent potential would reproduce the double-differential cross section data for emitted neutrons. As before, the impact parameter range is determined by a geometric model. This critical distance was found to be 3.3, 3.0, 3.2 and 2.7 fm for the kinetic energies of 150, 250, 400 and 650 MeV/nucleon, respectively for Au + Au systems. And for La + La and Nb + Nb systems at 400 MeV/nucleon, d_c was chosen to be 2.8 fm, and for La + La at 250 MeV/nucleon, $d_c = 3.0$ fm. The double differential cross sections in the rapidity bin $0.7 \leq \alpha = (Y/Y_{beam})_{cm} \leq 1.2$ for Au + Au collisions at beam energies of 150, 250, 400 and 650 MeV/nucleon are shown in Fig. 2.15, whereas Fig. 2.16 are for La + La and Nb + Nb collisions at beam energy 400 MeV/nucleon and La + La collisions at 250 MeV/nucleon. As displayed in both Fig. 2.15 and Fig. 2.16, this single coalescence fitting parameter reproduced well the double-differential cross section data of free neutrons for different systems and energies in both magnitude and polar angle dependence. At smaller angles the agreement worsens because of evaporation neutrons.

2.7.2 Triple-differential Cross sections

By restricting the BUU calculations to *free* neutrons with the specified NMDYI momentum dependent soft potential, the triple differential cross sections are compared with the experimental data. There are no additional free parameters in this calculations. Fig. 2.17 shows the triple-differential cross sections for Au + Au systems in the rapidity bin $0.7 \leq \alpha \leq 1.2$ region at polar angles $\theta = 15^o$ and $\theta = 21^o$, with kinetic energies

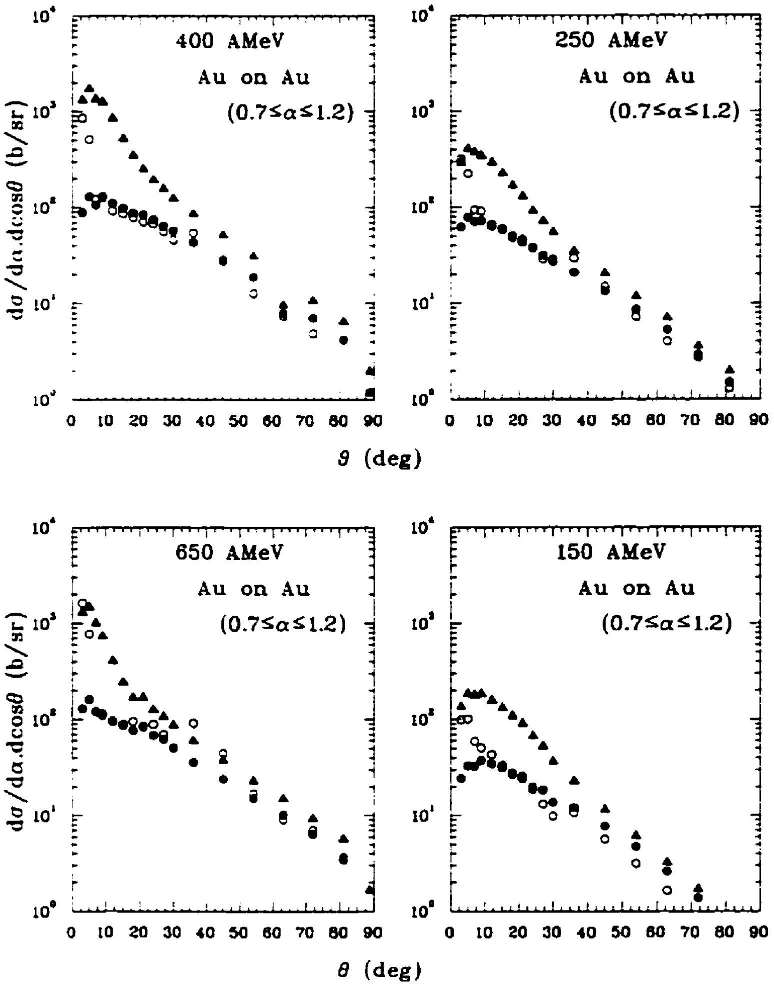

Figure 2.15: The polar angle dependence of the double-differential cross sections for *free* neutrons emitted with rapidities $0.7 \leq \alpha = (Y/Y_{beam})_{cm} \leq 1.2$ in Au-Au collisions at 150, 250, 400, and 650 MeV/nucleon. The open circles represent the experimental data, the filled symbols represent the results from the BUU theory: filled triangles represent all the nucleons whether free or bound in the clusters and filled circles represent free neutrons.

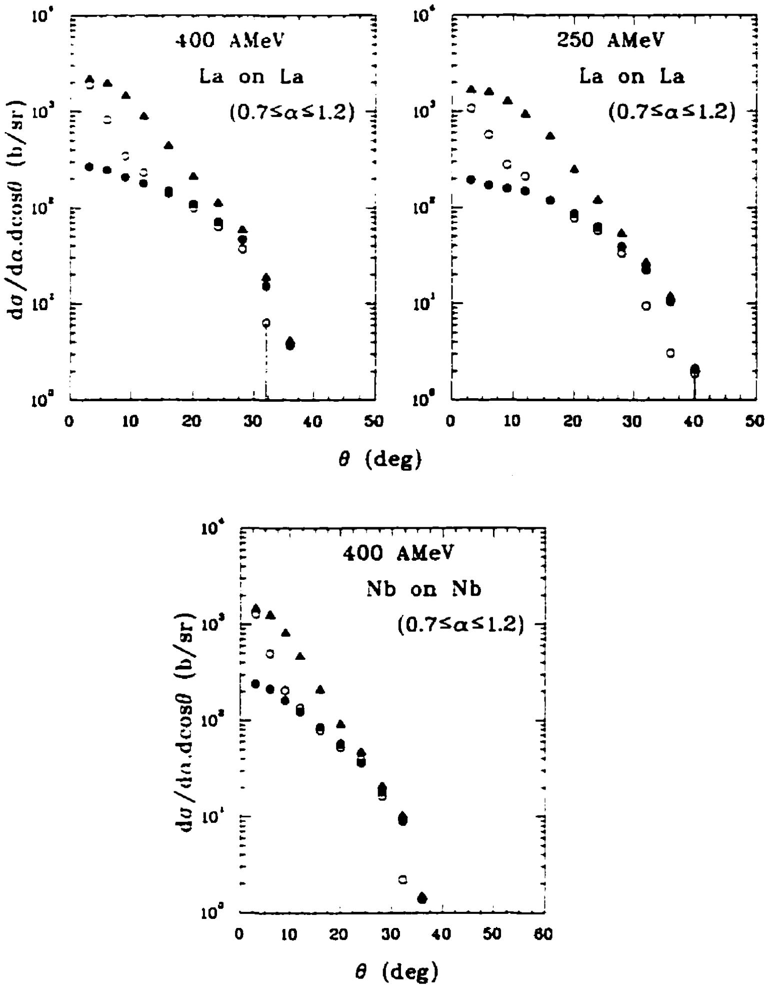

Figure 2.16: Double-differential cross sections for *free* neutrons emitted with rapidities $0.7 \leq \alpha = (Y/Y_{beam})_{cm} \leq 1.2$ in La-La collisions at 400 and 250 MeV/nucleon, and Nb-Nb collisions at 400 MeV/nucleon. The open circles represents the experimental data, the filled symbols represent the simulation results from the BUU theory: filled triangles represent all the nucleons whether free or bound in the clusters and filled circles represent free neutrons.

250, 400 and 650 MeV/nucleon, respectively. Fig. 2.18 displays the triple-differential cross sections for Au + Au at 400 MeV/nucleon, in three different rapidity bin regions: $0.7 \leq \alpha \leq 1.2, 0.2 \leq \alpha \leq 0.7$, and $-1.0 \leq \alpha \leq -0.2$. The polar angles are $\theta = 18^o$ and $\theta = 24^o$, respectively. In both figures, the open symbols represent the BUU simulation results, the filled circles represent the measured data with correction to the true reaction plane (zero dispersion $\Delta\phi_R = 0$) . Since the BUU calculation results are always extracted in the real reaction plane, it is important that the measured data should be corrected to zero dispersions in order to make meaningful comparison between the theory and the data. In fact, Fig. 2.17 displays the energy dependence of the triple-differential cross sections, as all the graphs shown in Fig. 2.17 are in the same rapidity region and also for the same symmetric Au + Au system. We can see the values of the triple-differential cross sections increase with the kinetic energy. Fig. 2.18 displays the different rapidity regions. In the forward rapidity regions, both the simulation results and the data tend to peak at $\phi = 0^o$ and fall off at $\phi = 180^o$. Whereas in the backward regions, the triple-differential cross section distributions peak at 180^o. These features agree with our understanding of the nuclear flow properties. In general, the simulation results reproduce the measured data well, including both the shapes and values. For Au + Au at 150 MeV/nucleon and other polar angles at 250, 400 and 650 MeV/nucleon, one can refer to Ref. [42] to see how well the complete data are reproduced by the theory.

The calculated triple-differential cross sections for free neutrons are shown in Fig. 2.19 for La + La and Nb + Nb systems in the most forward rapidity region $0.7 \leq \alpha \leq 1.2$ and backward rapidity region $-1.0 \leq \alpha \leq -0.2$ at 400 MeV/nucleon. In the rapidity region $0.2 \leq \alpha \leq 0.7$, the triple-differential cross sections from the three different systems Au-Au, La-La and Nb-Nb are shown in Fig. 2.20 at 400 MeV/nucleon, and also 250 MeV/nucleon for La-La system. The polar angle θ is around 20^o for all the systems in this figure. From these two figures, we again see that the BUU calculations agree remarkably well with the measured data.

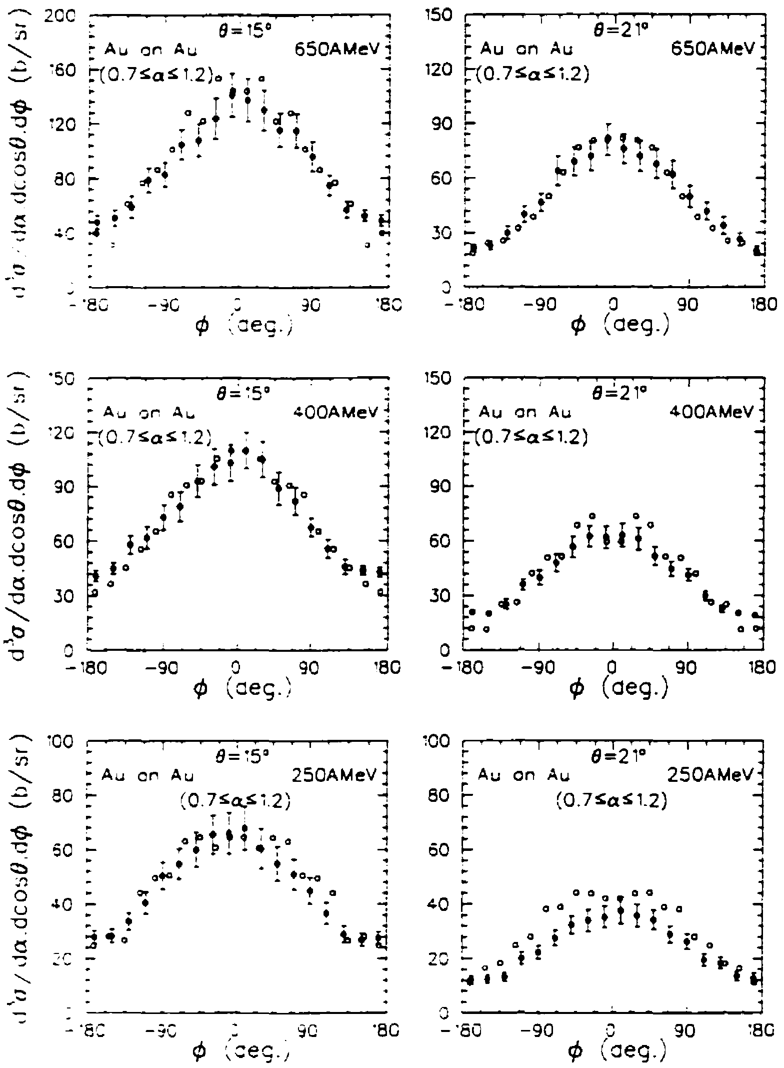

Figure 2.17: Triple-differential cross sections for the emission of *free* neutrons in the projectile-like rapidities ($0.7 \leq \alpha = (Y/Y_{beam})_{cm} \leq 1.2$) at polar angles $\theta = 15^o$, and 21^o, from Au-Au collisions at 250, 400, and 650 MeV/nucleon. Closed circles represent the measured data and the open circles represent the theoretical results(see the text).

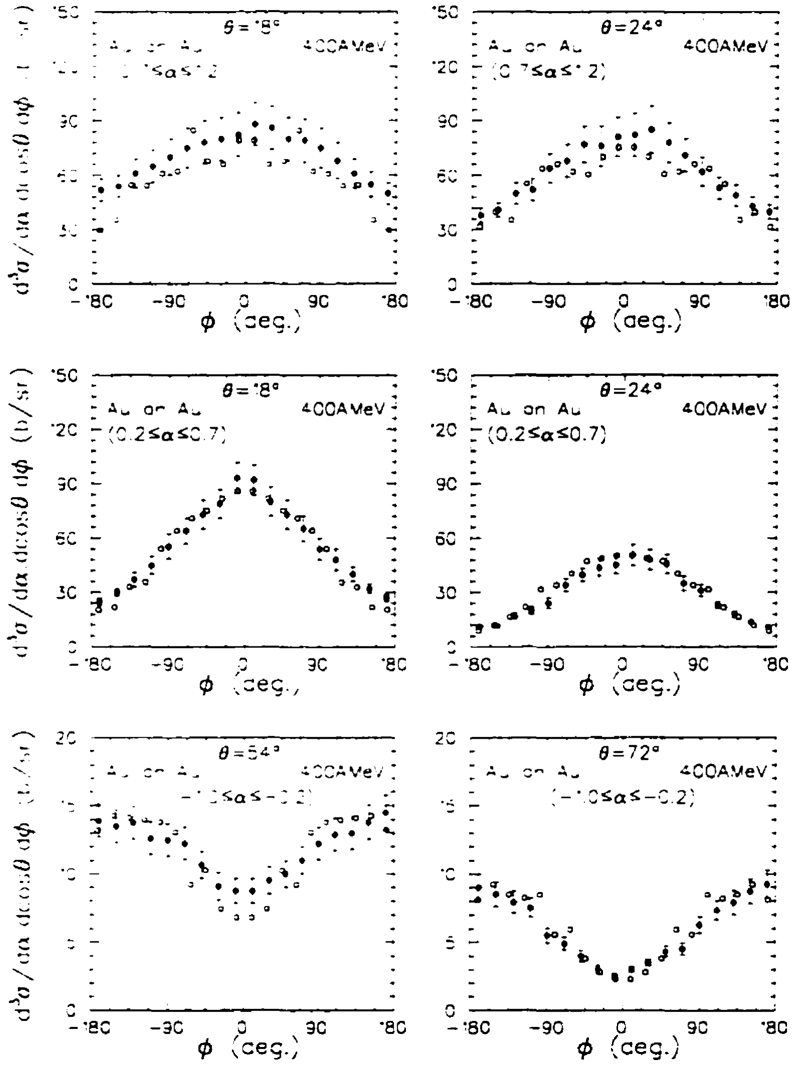

Figure 2.18: Triple-differential cross sections for the emission of *free* neutrons in three different rapidity regions ($0.7 \leq \alpha = (Y/Y_{beam})_{cm} \leq 1.2$, $0.2 \leq \alpha \leq 0.7$, and $-1.0 \leq \alpha \leq -0.2$) at polar angles $\theta = 18^o$, and 24^o, from Au-Au collisions at 400 MeV/nucleon. Closed circles represent the measured data and the open circles represent the theoretical results.

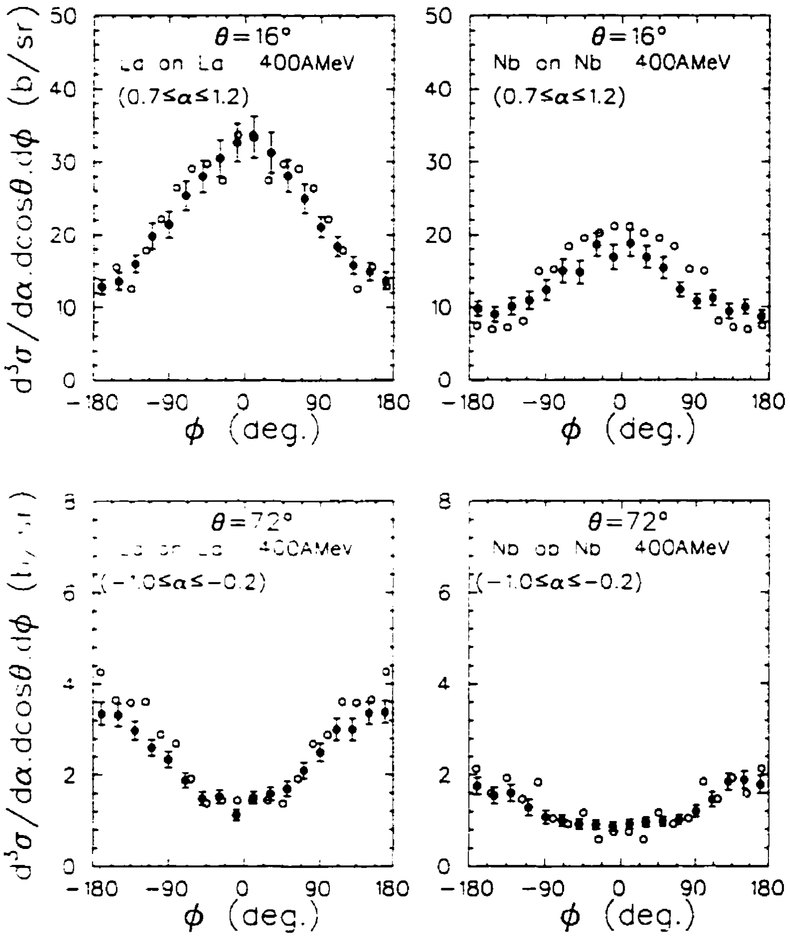

Figure 2.19: Triple-differential cross sections for the emission of *free* neutrons in the projectile-like rapidities ($0.7 \leq \alpha = (Y/Y_{beam})_{cm} \leq 1.2$) and backward rapidities ($-1.0 \leq \alpha \leq -0.2$) at polar angles $\theta = 16^o$, and 72^o, respectively, from La-La and Nb-Nb collisions at 400 MeV/nucleon. Closed circles represent the measured data and the open circles represent the theoretical results.

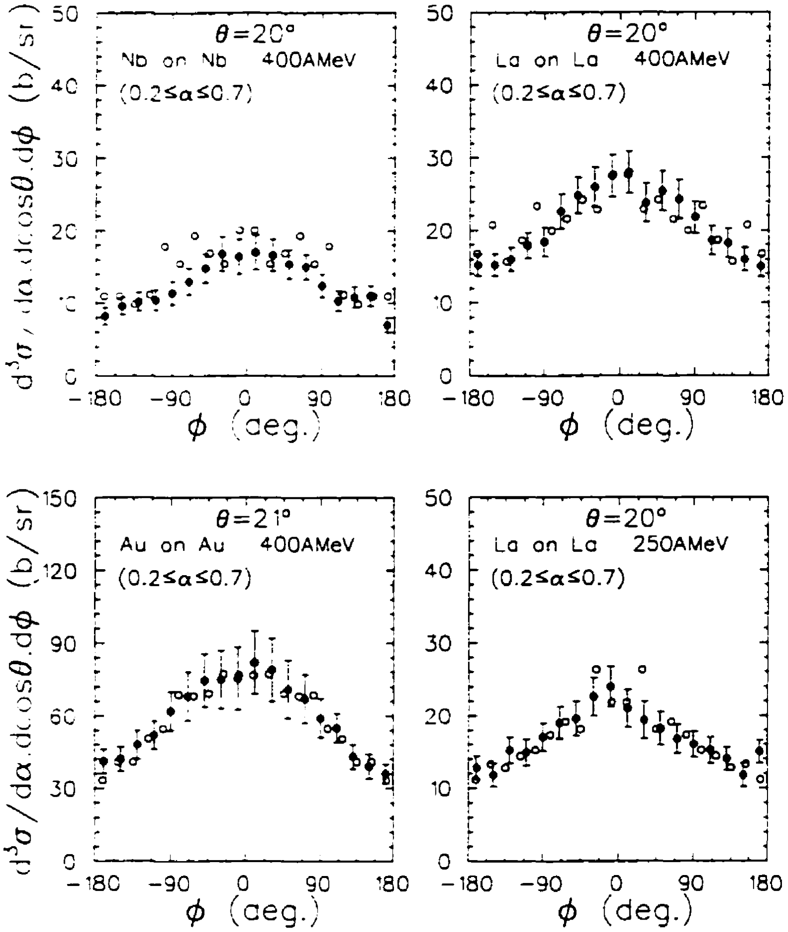

Figure 2.20: Triple-differential cross sections for the emission of *free* neutrons in the rapidities ($0.2 \leq \alpha = (Y/Y_{beam})_{cm} \leq 0.7$) at polar angles around $\theta = 20^o$, from Au-Au, La-La and Nb-Nb collisions at 400 MeV/nucleon, and La-La collisions at 250 MeV/nucleon. Closed circles represent the measured data and the open circles represent the theoretical results.

2.7.3 Maximum Azimuthal Anisotropy Ratio

If we integrate over the polar angle θ of the triple-differential cross sections, we will get another observable. the so-called azimuthal distributions $\frac{d\sigma}{d\phi}$. Those azimuthal distributions are measured event-by-event with respect to the reaction plane which can be estimated experimentally. There is always some error associated with the reaction plane determination [69]. As emphasized previously, the dispersion effect has to be corrected for in order to be able to compare with the simulation results. The sensitivity of such azimuthal distributions to the nuclear equation of state was examined by Welke et al. [37]. The maximum global azimuthal anisotropy ratio can be defined as

$$\mathcal{R} = \frac{\frac{d\sigma}{d\phi}|_{\phi=0^\circ}}{\frac{d\sigma}{d\phi}|_{\phi=180^\circ}} . \tag{2.17}$$

Welke et al. have shown that the maximum azimuthal anisotropy ratio for all test nucleons in a chosen rapidity range, $\mathcal{R}$, was sensitive to the value of the compressibility coefficient for equilibrium nuclear matter used in the theory [37]. Here we concentrate on free neutrons. The character of the composite fragments will be addressed in the following section. A maximum azimuthal anisotropy ratio can also be defined at each polar angle, in a given rapidity range:

$$r(\theta) = \frac{\sigma_3(\theta,\phi)|_{\phi=0^o}}{\sigma_3(\theta,\phi)|_{\phi=180^o}} , \tag{2.18}$$

where

$$\sigma_3(\theta,\phi) \equiv d^3\sigma/d(\cos\theta)d(\phi-\phi_R)dy . \tag{2.19}$$

The variables defined above can be determined in the experiments in the following way. For each polar angle, the cross section measured in the experiment are fitted with the function $\sigma_3(\theta,\phi-\phi_R) = a(\theta)+b'(\theta)\cos(\phi-\phi_R)$, where ϕ_R is the determined azimuthal angle of the reaction plane, and $b'(\theta) = b(\theta)e^{-(\Delta\phi_R)^2/2}$ is the correction for the finite rms dispersion $\Delta\phi_R$, which was obtained for each event. For positive rapidity particles, the triple-differential cross sections peak at $(\phi-\phi_R) = 0^o$ and deplete at $(\phi-\phi_R) = \pm180^o$, as seen in figures 2.17, 2.18, 2.19 and 2.20. The maximum azimuthal anisotropy for positive rapidity neutrons becomes $r(\theta) = [a(\theta)+b(\theta)]/[a(\theta)-b(\theta)]$.

The BUU calculations of the polar-angle dependence of the maximum azimuthal anisotropy ratio $r(\theta)$ for *free* neutrons emitted from Nb-Nb, La-La and Au-Au collisions at 400 MeV/nucleon are shown in Fig. 2.21 for $(b_{max}/2R) = 0.5$. In this figure, the BUU calculations with K=380, 210 and 150 MeV are done for free neutrons. Fig. 2.22 shows the BUU calculations of the polar-angle dependence of the maximum azimuthal anisotropy ratio $r(\theta)$ from La-La collisions at 400 and 250 MeV/nucleon for three different values of the nuclear compressibility coefficient K=380, 210 and 150 MeV. Consistent with the experimental data (see Ref. [44]), the BUU results in these two figures (Fig. 2.21 and 2.22) show very little sensitivity to the system mass and also the beam energy. The BUU calculations of the polar-angle dependence of the maximum azimuthal anisotropy ratio $r(\theta)$ for free neutrons emitted in La-La and Nb-Nb collisions at 400 MeV/nucleon and La-La collisions at 250 MeV/nucleon are compared with the data in Fig. 2.23. As we can see from this figure, the polar-angle dependence of the maximum azimuthal anisotropy ratio $r(\theta)$ is unfortunately insensitive to the nuclear compressibility coefficient K of the nuclear equation of state.

2.7.4 Average In-plane Transverse-Momentum

The calculated average in-plane transverse momentum $< P_x >$ of the free neutrons can be obtained by following the method of section **2.4** . Fig. 2.24 shows the average in-plane transverse momentum of free neutrons from Au-Au collisions versus the normalized neutron rapidity $\alpha = (Y/Y_{beam})_{cm}$ for the beam energies of 150, 250 and 400 MeV, respectively. The curves show the BUU calculation results with the momentum dependent NMDYI potential K=210 MeV and the symbols represent the measured data. From this figure, we can see that the BUU results agree well with the measured data. If we fit the data of this figure in the middle rapidity region (up to $\alpha = 0.5$), the flow parameter F' [3] are plotted in Fig. 2.25. The open squares are the flow F' of neutrons for the three bombarding energies; the circles are the results for the same three energies for protons plus

---

[3] Note F' can be connected with the flow F defined in Eq.(2.13) by $F' = F \times Y_{beam}^{cm}$

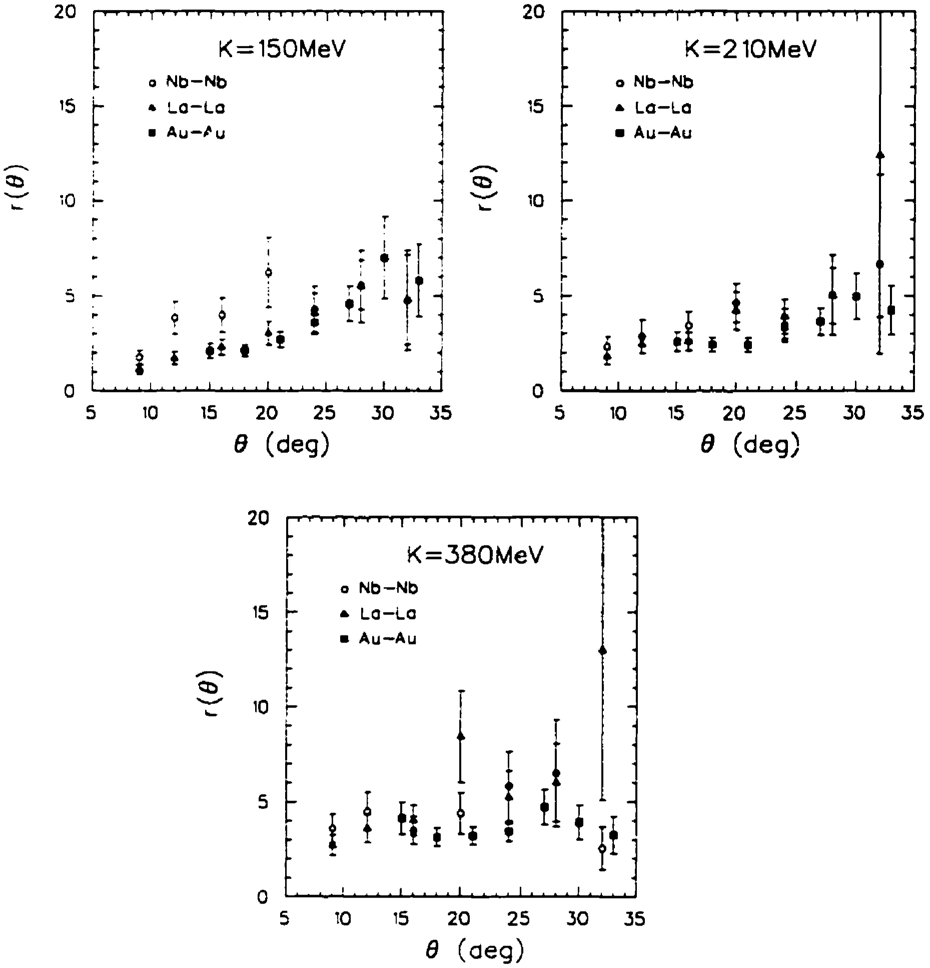

Figure 2.21: The polar-angle-dependent maximum azimuthal anisotropy ratio $r(\theta)$ of *free* neutrons as a function of the polar angle θ for Nb-Nb, La-La and Au-Au collisions at 400 MeV/nucleon from BUU calculations with MDYI type potential: K=150, 210, and 380 MeV, respectively.

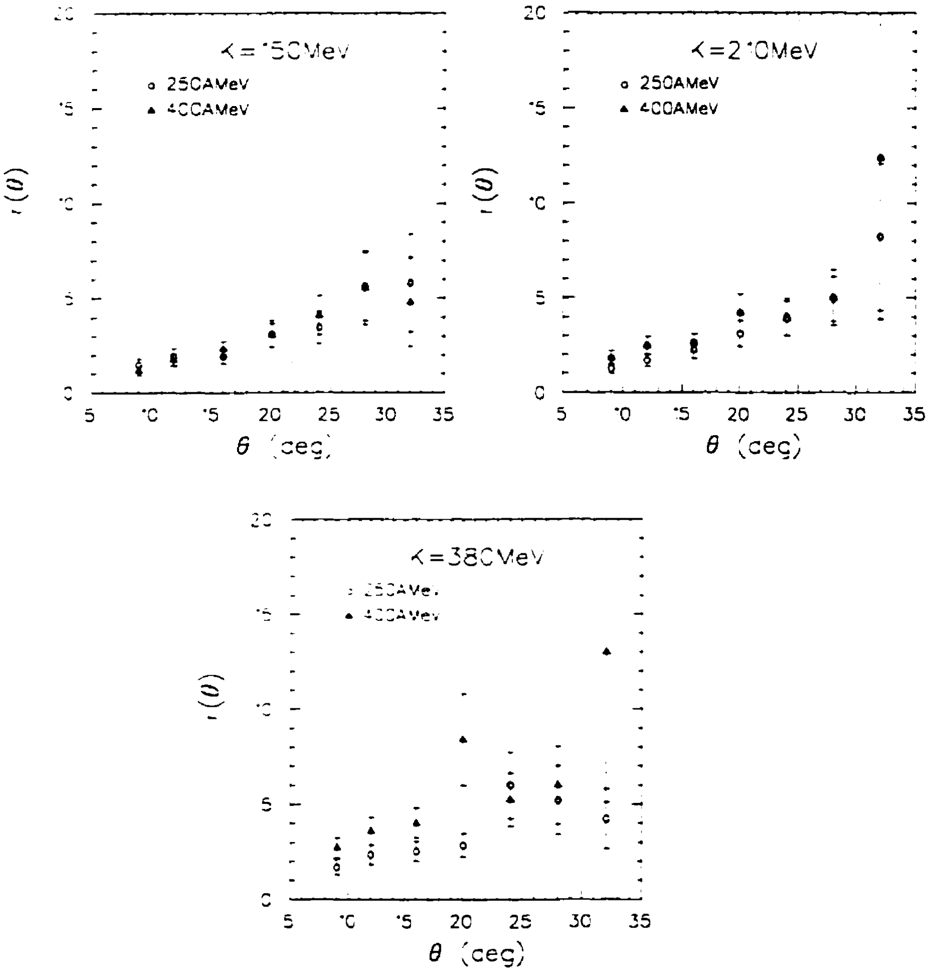

Figure 2.22: The polar-angle-dependent maximum azimuthal anisotropy ratio $r(\theta)$ of *free* neutrons as a function of the polar angle θ for La-La at 400 MeV/nucleon and 250 MeV/nucleon from BUU calculations with MDYI type potential: K=150, 210, and 380 MeV, respectively.

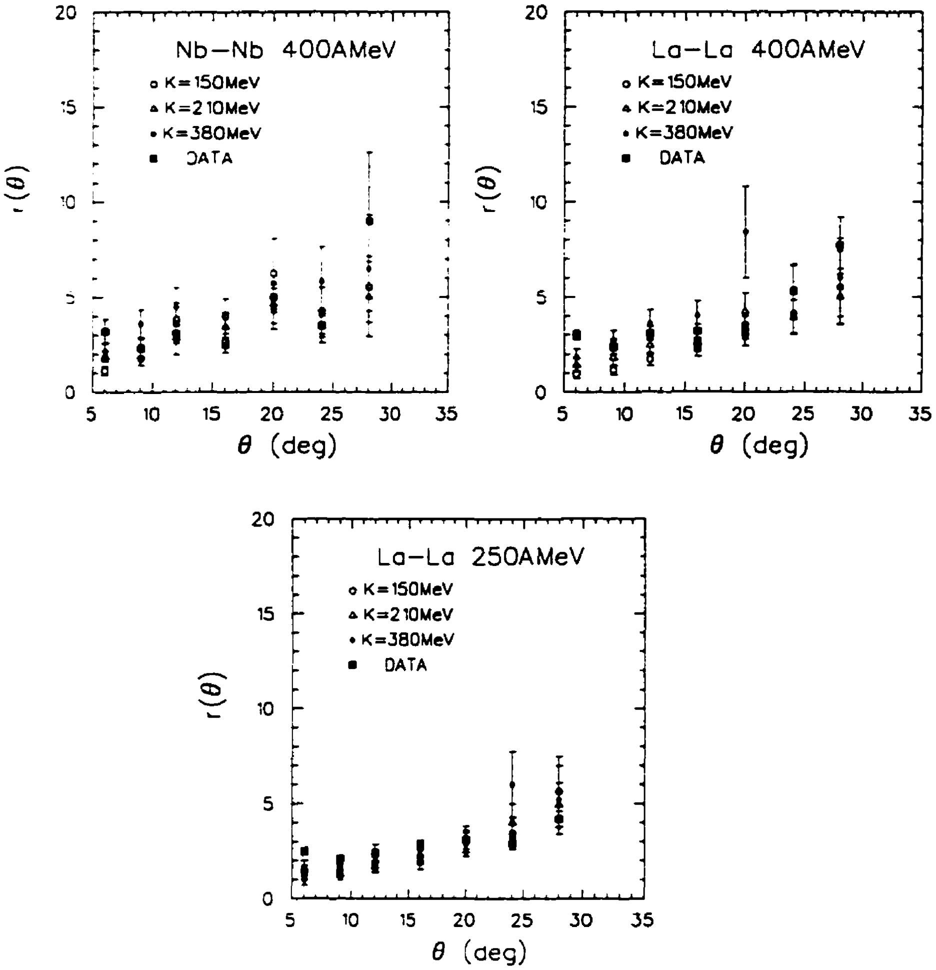

Figure 2.23: The polar-angle-dependent maximum azimuthal anisotropy ratio $r(\theta)$ of *free* neutrons as a function of the polar angle θ for La-La at 400 MeV/nucleon and 250 MeV/nucleon, and Nb-Nb collisions at 400 MeV/nucleon. The filled squares represent the measured data and the open symbols represent BUU calculations with MDYI type potential: K=150, 210, and 380 MeV, respectively.

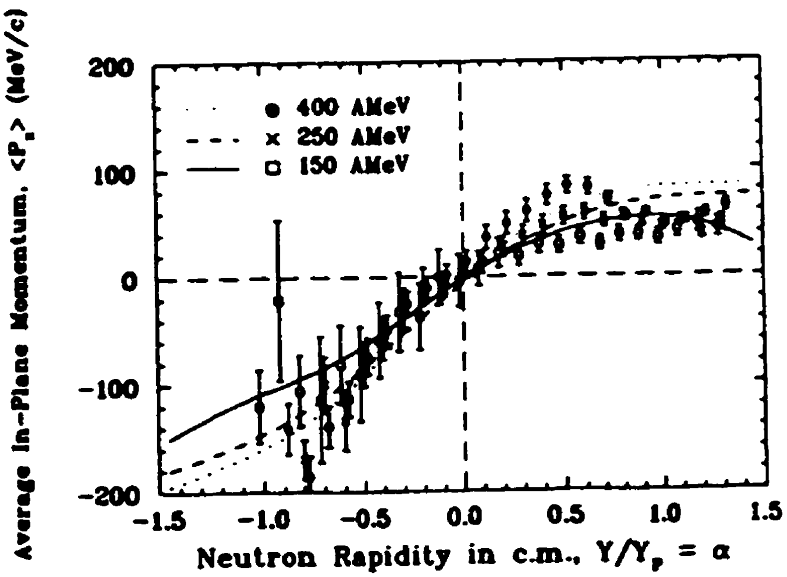

Figure 2.24: Average in-plane transverse momentum of *free* neutrons as a function of the rapidity ($\alpha = (Y/Y_{beam})_{cm}$) for 150, 250 and 400 MeV/nucleon Au-Au collisions. Symbols represent the measured data and lines represent the BUU calculations with NMDYI potential: K=210 MeV.

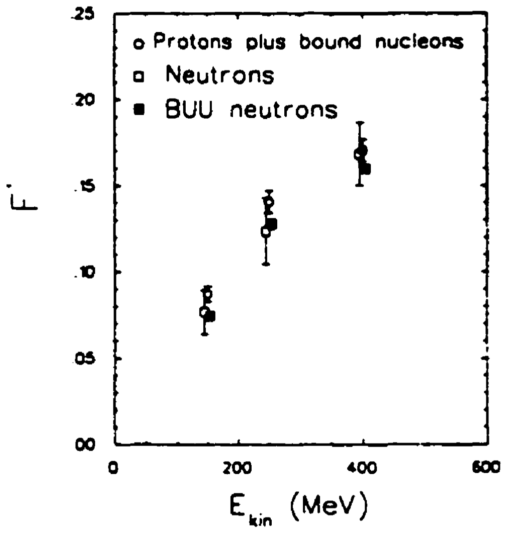

Figure 2.25: Flow of *free* neutrons (open squares) and protons plus bound nucleons(open circles) from Au-Au collisions against the beam energy. The filled squares represent the BUU calculations with NMDYI potential: K=210 MeV.

bound nucleons from the Plastic Ball Group [29]. The BUU calculations (solid squares) agree within uncertainties with the experimental data. We also calculated the average of $< P_x/P_\perp >$, where $P_\perp$ is the transverse momentum of neutrons. The average $< P_x/P_\perp >$ is plotted as a function of the neutron rapidity in Fig. 2.26 for Au-Au system. One can see again that the BUU calculations agree with the experimental data for the average $< P_x/P_\perp >$.

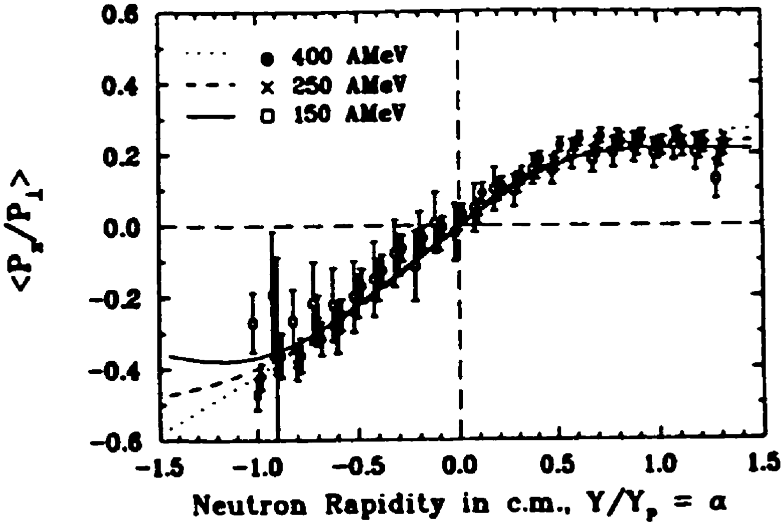

Figure 2.26: Normalized average $< P_X/P_\perp >$ of *free* neutrons as a function of the rapidity ($\alpha = (Y/Y_{beam})_{cM}$) for 150, 250 and 400 MeV/nucleon Au-Au collisions. Symbols represent the measured data and lines represent the BUU calculations with NMDYI potential: K=210 MeV.

For the two smaller systems La-La and Nb-Nb, the average in-plane transverse momentum distributions versus the normalized rapidity α for free neutrons are presented in Fig. 2.27 at 400 MeV/nucleon and also for La-La collisions at 250 MeV/nucleon. The filled symbols represent the experimental data, the open symbols represent the BUU calculations with the NMDYI potential (K=210 MeV). The experimental cuts are cautiously applied in the BUU simulations. Again, the BUU calculations generally agree with the experimental data within their uncertainties, especially in the mid-rapidity regions which gives the information about the flow parameter F'.

Let us summarize this section. By restricting the analysis to free neutrons, our BUU

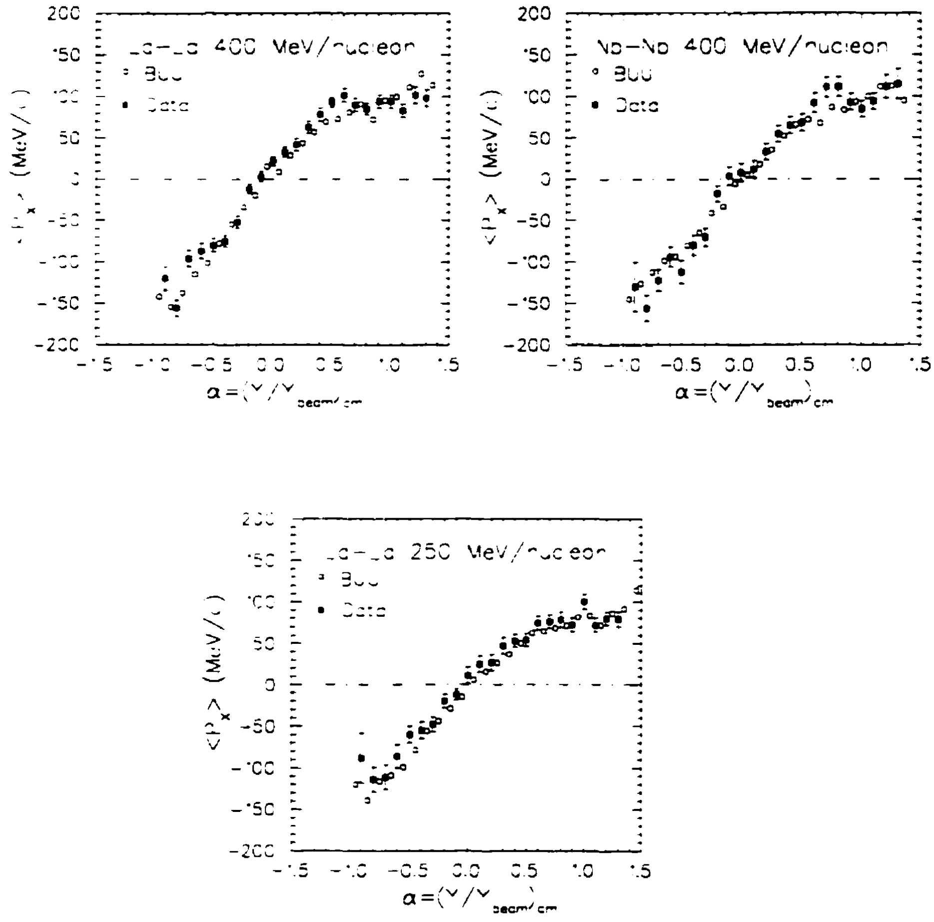

Figure 2.27: Average in-plane transverse momentum for *free* neutrons from La-La collisions at 400 and 250 MeV/nucleon, and Nb-Nb collisions at 400 MeV/nucleon as a function of the normalized rapidity of the neutrons in the centre-of -mass system. The filled symbols represent the measured data and open symbols represent the BUU calculations with NMDYI potential: K=210 MeV.

calculations with the NMDYI potential (K=210 MeV) plus the simple coalescence prescription generally agree very well with the E848H measured double- and triple-differential cross sections, except for smallest polar angles where the BUU cannot treat the neutron evaporation. Note that the prescription for calculating free neutrons is in fact approximate and may need improvement for low beam energies. It is in fact well known that the composite "contamination" in the BUU grows as the bombarding energy is lowered. Our BUU calculations can reproduce the experimental results of the in-plane transverse momentum $< P_x >$ for free neutrons. Both the experimental data and the BUU calculation results show that the polar-angle-dependent maximum azimuthal anisotropy $r(\theta)$ is insensitive to the system mass and the bombarding energy. The BUU calculations reveal that the $r(\theta)$ data for free neutrons are insensitive also to the nuclear compressibility coefficient K of the nuclear equation of state.

2.8 Fragment Azimuthal Distributions

As the sophistication in detection techniques increased, the separate measurement of the flow of nuclear clusters has revealed that "clusters go with the flow" [70] *i.e.* the amount of directed flow. as characterized by the in-plane transverse momentum per nucleon, was found to *increase* with fragment mass. This feature had in fact been predicted rather early [71]. Other calculations capable of producing nuclear fragments also contained the feature that flow effects should be stronger, the heavier the fragment [72, 73, 74, 75]. Here we will focus on the azimuthal distributions of the fragments.

As we have shown in the above section the azimuthal anisotropy ratio $r(\theta)$ of the *free* neutrons is insensitive to the compressibility K of the nuclear equation of state. However, calculations by Welke *et al.* [37] have reported that this azimuthal anisotropy ratio was an observable sensitive to the value of K used in the theory. The insensitivity was confirmed by a recent analysis of neutron azimuthal anisotropy [76]. To reconcile these two apparently contradictory analyses, we concentrate here on the case of semicentral collisions of Au-Au at 400 MeV/nucleon. The impact parameter range we shall integrate over is $0 \leq b \leq 6.2$ fm, and the critical distance in the coalescence approach was set at $d_c = 3.2$ fm. These conditions were determined in the investigation of E848H free neutron data in the above section.

The calculations were done with our momentum dependent MDYI type potential. The five parameters A,B,C, Λ and σ used here will correspond to the nuclear compressibility coefficient K=100, 150, 210 and 380 MeV (see table 2.1). Fig. 2.28(a) shows the maximum azimuthal anisotropy ratio $r(\theta)$ of free nucleons plotted against laboratory polar angle θ for near-central Au + Au collisions at 400 A MeV. For now, we restrict our analysis to the rapidity region $0.7 \leq (Y/Y_{\mathrm{beam}})_{\mathrm{c.m.}} \leq 1.2$ [40, 42, 43]. The statistical uncertainties in the calculation will be slightly larger near the edges of the populated region. As clearly shown in a previous section, these results further confirm that the free nucleon azimuthal data are essentially insensitive to variations in the nuclear EOS. In Fig. 2.28(b), we show $r(\theta)$ *vs.* θ for all BUU nucleon test particles. A much clearer sensitivity to the nuclear compressibility K can now be seen over most of the covered polar angle range. We may now subtract the free nucleons identified with our coalescence prescription to obtain a signal due to all the clusters averaged-over in the one-body BUU. This is show in Fig. 2.28(c). Clearly, the highest values of the azimuthal anisotropy ratio are reached with the clusters only. A strong variation with K is also observed. This is a quite important piece of information, as it verifies that the maximum azimuthal anisotropy of composite fragments as a technique to probe the nuclear EOS is really effective. As a further quantitative scrutiny, in Fig. 2.29 we plot the polar angle integrated azimuthal distributions for free nucleons and clusters, using the procedure described above. Both distributions peak at $\phi = 0°$. The azimuthal differential cross sections for composites are considerable larger than those for free nucleons for small azimuthal angles ϕ and become comparable at large ϕ, which shows that much higher partition of the clusters are emitted to small ϕ region compared to the *free* nucleons. The width of the composite distribution is also significantly smaller. Thus, our calculations are entirely consistent with the experimental observation that fragment

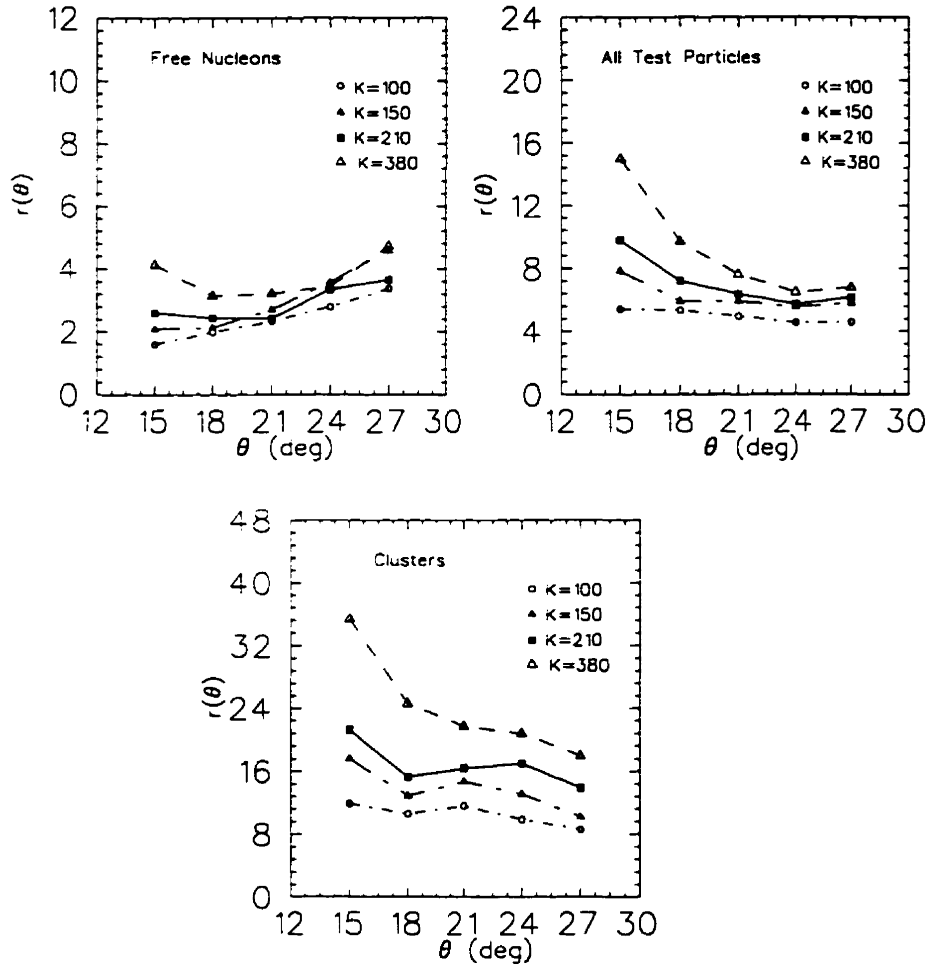

Figure 2.28: (a) We plot the azimuthal anisotropy ratio for free nucleons at a given polar angle, as a function of θ_{lab}.. The different symbols correspond to different values of the compressibility coefficient of equilibrium nuclear matter, in units of MeV. The reaction under scrutiny is ^{197}Au + ^{197}Au at 400 MeV/nucleon. The multiplicity cut corresponds to semi-central collisions. The statistical uncertainties are of the order of 10% in the middle of the populated area in polar angle and roughly 20% at the edges. (b) Same caption as (a), except that all BUU test particles are involved. (c) Same caption as (a), except that all free nucleons have been subtracted from the full set of BUU test particles.

flow is more correlated with the reaction plane than that of single particles [77]. These distribution differences between the free nucleons and clusters implicate that clusters may be subjected to less random thermal motion, thus could carry more information about the nuclear compression, which is directly related to the nuclear EOS. We will come back to discuss this point later. The azimuthal distributions for all the test particles can be produced by summing up these two components: the free nucleons and the clusters.

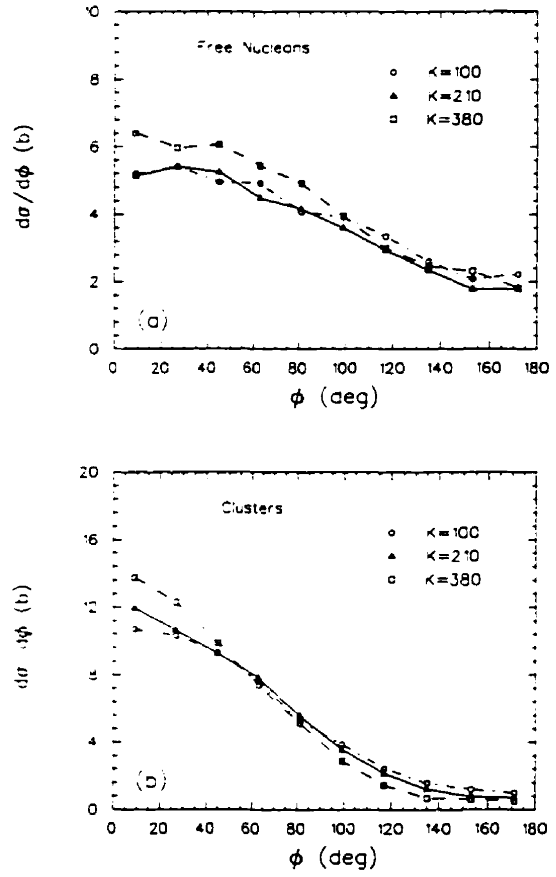

Figure 2.29: **(a)** The azimuthal distributions of free nucleons with respect to the reaction plane are plotted for Au-Au collisions at 400 MeV/nucleon with the BUU theory. The calculations shown correspond to three different values of K. The units of K are MeV. The curves were drawn to guide the eye. **(b)** Same caption as (a) but for clusters.

We now calculate the maximum global anisotropy ratio $\mathcal{R}$, subject to the same kinematical rapidity and spectator cuts as before. We plot $\mathcal{R}$ against the coefficient of compressibility for equilibrium nuclear matter, K, in Fig. 2.30. Each point in this figure represents a set of impact parameter integrated BUU calculations. The power and simplicity of this plot is immediately apparent: an experiment measures one value of $\mathcal{R}$, given a well defined set of kinematical constraints. This would appear on this plot as an horizontal line. The intercept of this line with the appropriate theoretical curve would then directly yield a value of K. The free nucleons do not constitute a very sensitive observable, as we can see: the steeper the curve, the more accurate is the deduced value of K. All the test nucleons analyzed together are somewhat sensitive to the value of K, but the clusters alone are much more sensitive. As in the past one-body theories such as the BUU have compared with "pseudo-nucleons" obtained from folding all the measured particles (free nucleons and composites) together [78, 79], an analogous procedure can be followed to produce a value of $\mathcal{R}$ to be interpreted with the top curve in our Fig. 2.30. The values of $\mathcal{R}$ obtained here with the full BUU test particle ensemble are comparable in magnitude with those of the original study of Welke *et al.*[37], done with a different system at a slightly different bombarding energy.

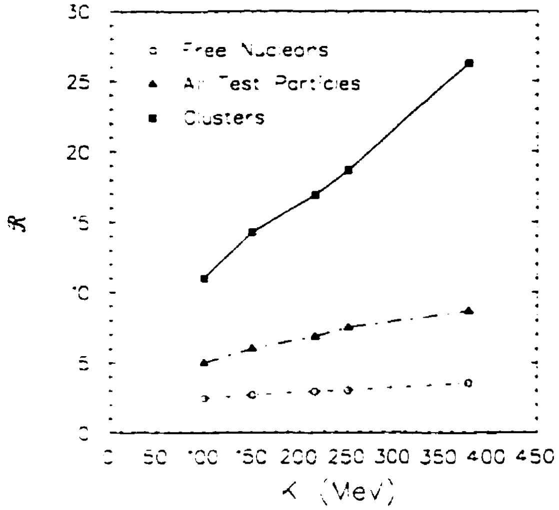

Figure 2.30: We plot the maximum global azimuthal anisotropy ratio $\mathcal{R}$ as defined in the main text, as a function of the compressibility coefficient for equilibrium nuclear matter for Au-Au collisions at 400 MeV/nucleon with the BUU theory. The kinematical cuts are such that particles with rapidity Y such that $0.7 \leq (Y/Y_{\text{beam}})_{\text{c.m.}} \leq 1.2$ were accepted. The curves were drawn to guide the eye.

As mentioned above, the usefulness of the azimuthal anisotropy ratio depends largely on an accurate determination of the event reaction plane. A method which circumvents this difficulty is based on the azimuthal pair correlation function [41]:

$$C(\psi) = \frac{P_{cor}(\psi)}{P_{uncor}(\psi)} , \tag{2.20}$$

where ψ is the smaller azimuthal angle between the transverse momenta of two particles. $P_{cor}(\psi)$ is the ψ distribution for observed pairs from the same event, and $P_{uncor}(\psi)$ is the ψ distribution for pairs from mixed events. Following Ref. [37], let us assume that the azimuthal cross section has the form

$$\frac{d\sigma}{d(\phi - \phi_R)dY} = a[1 + \lambda \cos(\phi - \phi_R)] \tag{2.21}$$

where ϕ_R is the azimuthal angle of the reaction plane. If this parametrization is exact, $C(\psi)$ can be written as

$$C(\psi) = 1 + \frac{1}{2}\lambda^2 \cos(\psi) . \tag{2.22}$$

The maximum global azimuthal anisotropy ratio defined earlier can be expressed as

$$\mathcal{R} = \frac{\frac{d\sigma}{d\phi}|_{\phi=0^\circ}}{\frac{d\sigma}{d\phi}|_{\phi=180^\circ}} = \frac{1+\lambda}{1-\lambda} . \tag{2.23}$$

Thus, measuring the azimuthal pair correlation function can immediately provide us with the anisotropy ratio, $\mathcal{R}$, without the ambiguities associated with event-by-event reaction plane determination. We can easily verify the validity of Eq. 2.21 as an accurate parametrization in the case at hand. Since the issue of statistics is quite important here, we shall slightly shift our rapidity window. We shall choose $0.4 \leq (Y/Y_{\mathrm{beam}})_{\mathrm{cm}} \leq 0.8$ as a sufficiently populated region with a reasonable sensitivity to the nuclear EOS, other kinematical constraints being the same. We study the same reaction as before, with the same reaction parameters. Fig. 2.31(a) is a plot of the azimuthal cross section for all test particles, calculated with three different equations of state: K = 100, 210, and 380 MeV. The curves represent a fit with the parametrization of Eq.(2.21). Fig. 2.31(b) represents the same exercise repeated for clusters as defined through our coalescence prescription. In both cases the accuracy of the cosine assumption is remarkable. We plot on Figs. 2.32(a) and 2.32(b) the azimuthal pair correlation function as calculated numerically, together with the parametrization, Eq.(2.22). The value of λ used are the same ones obtained by

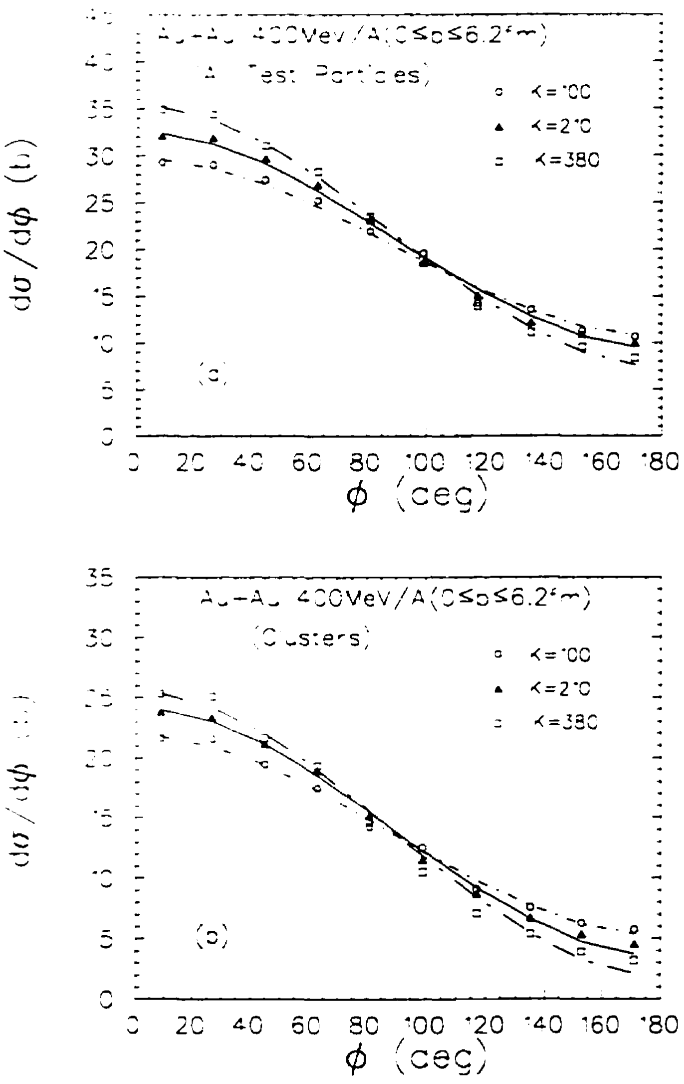

Figure 2.31: (a) The azimuthal distributions of free nucleons with respect to the reaction plane are plotted. The calculations were repeated from three different values of K. The units of K are MeV. The rapidity window has been shifted to $0.4 \leq (Y/Y_{\mathrm{beam}})_{\mathrm{c.m.}} \leq 0.8$. The curves are not drawn through the data as a guide but represent a fit with Eq.(2.21). (b) Same caption as (a) but for clusters.

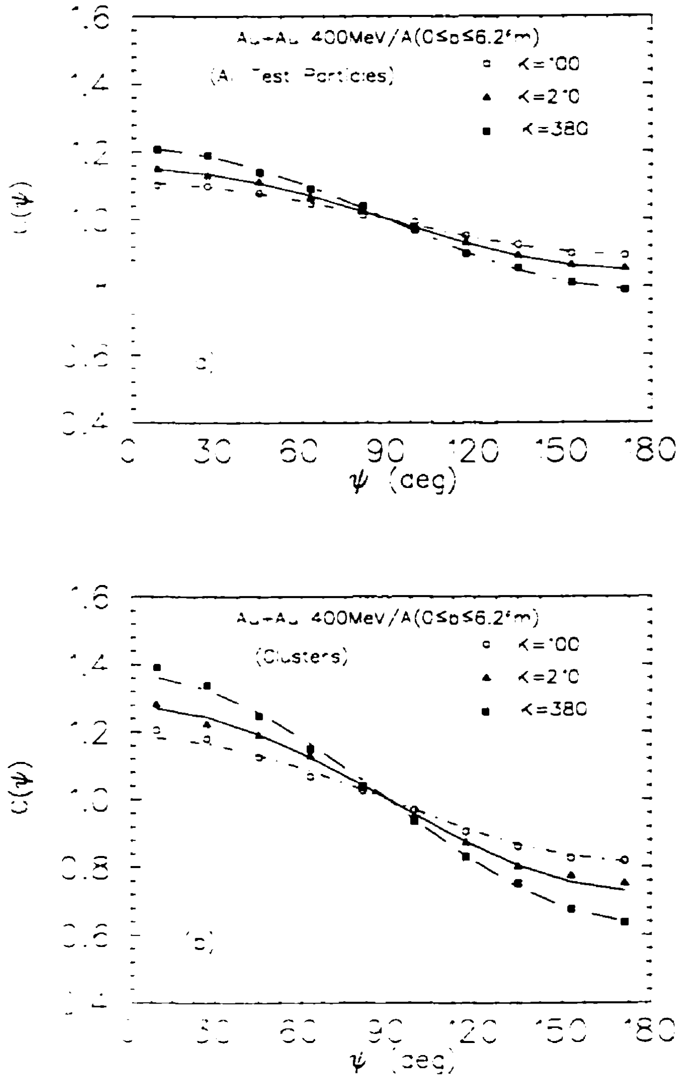

Figure 2.32: (a) The azimuthal correlation function, calculated with all the BUU test nucleons is plotted. The curves represent Eq.(2.22) with values of λ obtained from Fig. 2.31. (b) Same caption as (a) but for clusters.

fitting the results in Fig. 2.31. Again, the agreement between the analytic formulae and the numerical results is excellent. We can now easily plot the azimuthal anisotropy ratio as a function of compressibility as before. See Fig. 2.33. The results are very similar to those obtained with the rapidity window $0.7 \leq (Y/Y_{\text{beam}})_{\text{c.m.}} \leq 1.2$, but with somewhat smaller numerical values. In cases where the cosine form is not appropriate or when the reaction plane is simply not measured, one can define a slightly modified definition of a global azimuthal anisotropy ratio:

$$\mathcal{R}' = \frac{C(\psi = 0^\circ)}{C(\psi = 180^\circ)} . \tag{2.24}$$

In the theory, this quantity has the same desirable behavior with respect to variations of the nuclear matter compressibility coefficient as $\mathcal{R}$ as seen in Fig. 2.34. It can then also be useful in comparisons of experimental results with theoretical calculations.

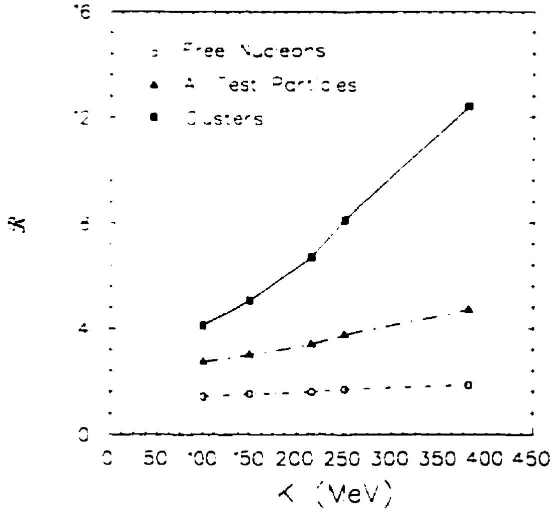

Figure 2.33: We plot the maximum global azimuthal anisotropy ratio as defined in the main text, as a function of the compressibility coefficient for equilibrium nuclear matter for Au-Au collisions at 400 MeV/nucleon with the BUU theory. The kinematical cuts are such that particles with rapidity Y such that $0.4 \leq (Y/Y_{\text{beam}})_{\text{c.m.}} \leq 0.8$ were accepted. The curves were drawn to guide the eye.

Since the maximum azimuthal anisotropy ratio $\mathcal{R}$ in Eq.(2.23) depends only on the constant λ, to see the feature of fragment mass dependence in the BUU theory, in Fig. 2.35(a), we have plotted λ as a function of the normalized centre of mass rapidity

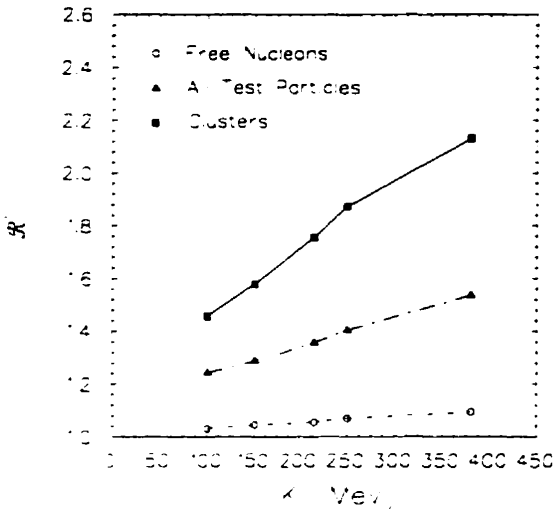

Figure 2.34: We plot the modified global azimuthal anisotropy ratio as defined in the main text, as a function of the compressibility coefficient for equilibrium nuclear matter for Au-Au collisions at 400 MeV/nucleon with the BUU theory. The kinematical cuts are such that particles with rapidity Y such that $0.4 \leq (Y/Y_{\mathrm{beam}})_{\mathrm{c.m.}} \leq 0.8$ were accepted. The spectator cut as defined in the main text was also implemented. The curves were drawn to guide the eye.

$Y_{cm} = (Y/Y_{beam})_{cm}$ for the fragment mass $A \leq 2, A \leq 4$ and all possible sizes, respectively. Bear in mind, the BUU is one-body theory. Fig. 2.35(a) shows that the value of λ is slightly fragment mass dependent. The displayed features are in fact consistent with the measured data [80]. For the light fragments, the BUU simulation results can really match the data as shown in Fig. 2.35(b).

The reasons for the maximum anisotropy ratio of clusters being more sensitive to the nuclear EOS may be complicated. But, a simple interpretation might assume that clusters suffer less thermal motion, thus being more affected by the compression energy. To probe the thermal aspect of the dynamical evolution, we make use of the quadrupole tensor in momentum space. The diagonal component of this quadrupole moment at the freeze-out time t is

$$Q_{zz} = \int \frac{d\vec{r}d\vec{p}}{(2\pi)^3}(2p_z^2 - p_x^2 - p_y^2)f(\vec{r},\vec{p},t) \qquad (2.25)$$

For a completely thermalized system, Q_{zz}=0. For two noninteracting Fermi sphere , which approximately form the initial state of two colliding nucleus, Q_{zz} can be calculated [81]: $Q_{zz} = 4AP_b^2$, where P_b is the projectile momentum in the c.m. frame, A is the nuclear

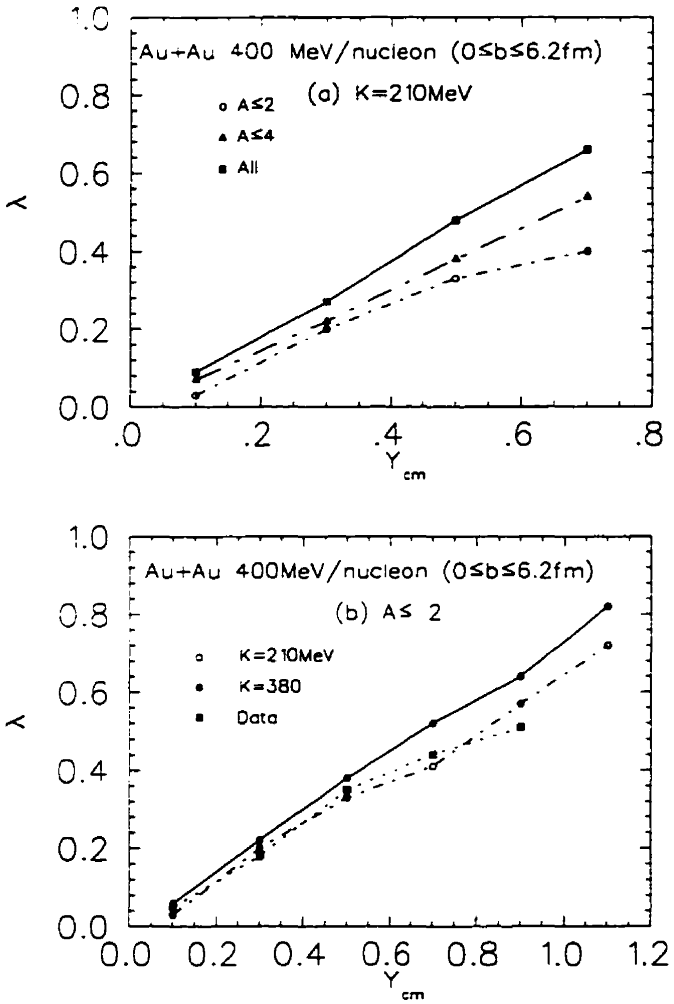

Figure 2.35: We have plotted λ (see text) as a function of the normalized centre of mass rapidity, (a) for the fragment mass $A \leq 2, A \leq 4$ and all possible sizes, respectively, with the NMDYI potential: K=210 MeV; (b) the fragment mass $A \leq 2$, the filled squares represent the data, the filled circles represent the calculations with the hard MDYI type potential: K=380 MeV, and the open circles represent the calculations with the NMDYI potential: K=210 MeV; for Au-Au collisions at 400 MeV/nucleon with the BUU theory.

mass number. The smaller the moment, the closer the system is to a thermal one. During the nucleus-nucleus collision processes, this quadrupole moment will have its largest value at the beginning, then decrease and to a smaller value at the so-called freeze-out time. We have calculated the average quadrupole moment per particle at freeze-out time. The values are 0.035 $(GeV/c)^2$ for free nucleons, 0.109 $(GeV/c)^2$ for test nucleons, and 0.135 $(GeV/c)^2$ for the clusters. It clearly shows that clusters suffer much less thermal random motion.

2.9 Summary

We have used the Boltzmann-Uehling-Uhlenbeck equation to describe the dynamics of nucleus-nucleus collisions. Concentrating on the momentum dependent features of the one–body self–consistent nuclear mean field, we have seen that the precise functional dependence on momentum of the interaction was important. Taking two phenomenological potentials with the exact same characteristics at saturation density and zero temperature (NGBD and NMDYI), we have shown that their behavior in situations removed from equilibrium could be quite different. From a purely theoretical point of view we believe that approaches based on MDYI type interactions are on a firmer basis. In GBD like approaches, the quantity $< \vec{p} >$ was put in by hand to enforce the Galilean invariance of the potential. MDYI has Galilean invariance from the start and furthermore, the fact that it can be identified with the Fourier transform of a Yukawa potential is pleasing. Both interactions have the virtue of being relatively simple to handle (MDYI is however trickier to implement numerically). Again, in equilibrium or close to equilibrium situations it should make little difference which is used.

By performing calculations to address data on symmetric and asymmetric systems at high energies, one can indeed assess the importance of the density–dependent and momentum dependent terms in the nuclear equation of state, separately. In pursuing this point, we have for the first time compared DIOGENE and EOS TPC data with BUU results. We find that all the data we have considered in this work can be reproduced with a momentum dependent interaction with a nuclear compressibility coefficient of K = 210 MeV. Also, we have verified again the importance of angular momentum conservation on the generation of transverse momentum in high energy heavy ion collisions. Relaxing the conservation law leads to a slight variation in the flow parameter in BUU collisions. This change should be considered in high precision fits of the experimental data as it should undoubtedly lead to lower values of χ^2 [82]. This does not however alter the general conclusions reached in this work.

Furthermore, by using a simple coalescence prescription to restrict the analysis to *free* neutrons, we have simulated the E848H collaboration measurements. The BUU calculations of the triple-differential cross sections and in-plane transverse momenta for *free* neutrons agree generally with the data. Comparisons with the data reveals that the maximum azimuthal anisotropy ratio $r(\theta)$ of *free* neutrons is insensitive to the nuclear compressibility K of EOS. This is a quite important piece of information, as a previously full one-body calculation of $r(\theta)$ exhibited considerable structure and sensitivity to K [76]. We have provided an explanation for such an apparent discrepancy. This involved emphasizing the role played by the nuclear composite fragments and their participation in the collective nuclear flow. We have found behaviors in qualitative agreement with earlier calculations with different models [75] and with existing experimental data [83]. Because of the large sensitivity of the composite flow to the nuclear EOS, we further established a quantitative connection between the composite flow and K. It is clear that our approach to clustering in heavy ion reactions is simple but we believe that more sophisticated scenarios should reach similar physical conclusions. Our aim is to extract some physics content in an admittedly phenomenological fashion, not to provide a rigorous and complete theory of cluster production. However, the theoretical problems associated with a complete time-dependent theory of composite formation are being addressed. We believe that therein lies the key to a more complete understanding of the nuclear dynamics involved in heavy ion collisions. In this respect, it is quite stimulating that very high quality data is becoming available.

Finally, it is worth pointing out that after more than a decade of careful experimental investigations and theoretical progress, a consistent picture of the behavior of nuclear matter at high temperatures and densities is emerging. Perhaps the crudest way of characterizing the nuclear equation of state is by its compressibility coefficient and this value is now stabilizing to some number around 210 MeV. The fact that low and high energy heavy ion experiments seem to require compatible values of K is satisfying. The fact that high quality, bias-free, exclusive experimental data is now available and will continue to be generated in the immediate future will set even more stringent tests for the models.

Chapter 3

Dilepton Production in Nucleus-nucleus Collisions

3.1 Introduction

Dileptons and photons are possibly the best carriers of information from the hot and compressed nuclear matter produced in the early stages of heavy ion collisions [84]. As introduced in chapter 1, in principle, those electromagnetically interacting particles can leave the hadronic environment from which they are created without significant disturbances, offering thus a relatively clean probe of the nuclear collision dynamics. In heavy ion collisions at incident energies of 1-5 GeV/nucleon, where the Lawrence Berkeley Laboratory Dilepton Spectrometer(DLS) has already taken dielectron measurements [85], the most important sources of e^+e^- pairs seem to be the Dalitz and radiative decays: mainly from η mesons and $\Delta's$, pion-pion annihilations, and nucleon-nucleon bremsstrahlung [13, 14, 15, 86]. Measurements of lepton pair production in single nucleon-nucleon reactions have also been performed in the GeV energy regime. In those, the measured pd/pp dielectron yield ratios display a clear beam energy as well as a clear invariant mass dependence [87]. This suggests that the dominant mechanism for dilepton production may be changing as the beam energy per nucleon increases from 1 to 5 GeV. In particular, one should pay attention to the opening of inelastic channels. The latter have been shown to play an important role for dielectron production in nucleon-nucleon collisions at 4.9 GeV [86]. To eventually understand quantitatively and completely the relative role of all these contributions and their excitation function in the complex environment of nucleus-nucleus collisions, it is vital to calculate the lepton pair production cross section for individual processes as accurately as possible and to simulate the nucleus-nucleus collision dynamics with a successful model. The aim of this work is thus to re-analyze the main dielectron sources and compare the BUU simulation results to measurement made at 1 GeV/nucleon kinetic energy.

The previous BUU calculations [13, 14, 15] for dielectron yields in nucleus-nucleus collisions used a simple Skyrme momentum-independent potential. As displayed in Chapter **2**, the momentum-dependence of the nuclear potential is essential to interpret the collective side-flow phenomenology. Stimulated by the re-analyzed DLS Ca + Ca dielectron spectrum data at 1.05 GeV/nucleon [12], we will also analyze, for the first time, the effect of nuclear EOS on the dielectron pair production.

We extend our approach to explicitly include pion degrees of freedom and also to consider the $\Delta \rightarrow \pi N, \pi N \rightarrow \Delta$ processes in conjunction with processes already described previously. This method then reproduces the measured pion yields with high accuracy [88]. Instead of conventional detailed balance, the $\sigma_{n\Delta\rightarrow nn}$ is related to $\sigma_{nn\rightarrow n\Delta}$ by [63]

$$\sigma_{n\Delta\rightarrow nn}(\sqrt{s}) = \frac{\frac{1}{8}\frac{mp_f^2}{p_i}\sigma_{nn\rightarrow n\Delta}}{\int_{m_N+m_\pi}^{\sqrt{s}-m_N}\frac{dm'}{2\pi}m'F_\Delta(m')p'} \tag{3.1}$$

with the actual mass of the Δ, $m^2 = E^2 - p^2$, E and p are the c.m. energy and momentum of delta in the initial or final state channel. p_f and p_i are the c.m. momenta in the NN channel and $N\Delta$ channel, respectively. And the delta mass distribution is

$$F_\Delta(m) = \frac{4m_\Delta^2\Gamma_\Delta}{(m^2 - m_\Delta^2)^2 + m_\Delta^2\Gamma_\Delta^2}. \tag{3.2}$$

For the Δ width, Γ_Δ, we take [63]

$$\Gamma_\Delta = \frac{2}{3}\frac{f_\Delta^2}{4\pi}\frac{m_N}{m_\pi^2}\frac{p^3}{m}\left[\frac{\beta^2 + p_\Delta^2}{\beta^2 + p^2}\right]^2 \tag{3.3}$$

with $f_\Delta^2/4\pi = 0.37, \beta = 300$ MeV/c, and p, p_Δ are the pion three-momenta in the rest frame of the Δ with mass m and m_Δ, respectively. The cross section for Δ formation in

πN interaction is determined such that

$$\sigma_{N\pi\to\Delta} = \frac{\pi}{p^2}\frac{g_\Delta}{2}\Gamma_{\Delta\to N\pi}F_\Delta(m), \tag{3.4}$$

where g_Δ is the spin degeneracy of the Δ resonance, and p is the c.m. momentum in πN channel. The isospin components of the Δ are followed explicitly in the numerical calculation. In addition to the nucleons and delta resonances, the propagated particles include free pions, which follow the classical Hamilton equations.

We have checked the effect of explicitly including free pions on the collective baryon flow. Calculations were done with two different algorithms: including free pions or not. The NMDYI momentum dependent potential with nuclear compressibility K=210 MeV was used. The results show that the differences between results with the two algorithms are within the numerical fluctuations.

This chapter is organized as follows. In the following section, we will discuss the microscopic calculation method for the nucleon-nucleon bremsstrahlung. Comparisons with previous approaches will also be made. Then in section **3**, the treatment of Dalitz Δ decay and η decay will be presented in detail. The η meson production in heavy ion collisions will also be studied. Following the presentation of pion-pion annihilation and bremsstrahlung (section **4**), in section **5** we discuss the nuclear EOS effects on the dileptons and compare the calculated dilepton production results with the experimental data. Finally, we give some concluding remarks.

3.2 Nucleon-nucleon Bremsstrahlung

Several different calculations for electron-positron pair emission through nucleon-nucleon bremsstrahlung have been performed for reactions at, and slightly above, 1 GeV. Some of the more sophisticated approaches used relativistic one-boson exchange (OBE) Lagrangians, with the coupling to the electromagnetic field done by minimal substitution [24, 25, 26]. These approaches are thus entirely Lorentz-covariant and are also gauge-invariant in the electromagnetic sector. Note that the OBE dilepton calculations can be made gauge-invariant even when form factors at the strong interactions vertices are used [24]. Such approaches have all the transformation properties that are required of a complete theory but they are not completely satisfactory in two respects. First, they are very cumbersome. If several meson fields are involved, the number of Feynman graphs to be evaluated proliferates rapidly and the difficulty of the calculations increases accordingly. The coupling constants in the OBE model are fitted such that the total nucleon-nucleon cross sections are reproduced as closely as possible. This exercise thus has to be repeated for each colliding system. Second, even if two different OBE calculations with two slightly different set of ingredients (meson fields, form factors and coupling constants) can do a good job of generating total nucleon-nucleon cross sections that are in agreement with experimental measurements, generally they will then have different predictions for the differential cross sections. As we shall see below, there is a way of writing the very low invariant mass dilepton production cross section in nucleon-nucleon collisions such that it clearly depends on the differential elastic cross section of the colliding partners. This fact thus imposes very stringent requirements on the OBE models as far as their ability to predict lepton pair production yields is concerned. Because of the above considerations, several calculations pertaining to the bremsstrahlung generation of low invariant mass lepton pairs in nucleon-nucleon collisions have used a soft photon approximation [90]. A lot of the recent calculations of dielectron production in nucleon-nucleon collisions that have used the soft photon approximation as their starting point a formula suggested by Rückl [22]:

$$E_+E_-\frac{d^6\sigma^{e^+e^-}}{d^3p_+d^3p_-} = \frac{\alpha}{2\pi^2}\frac{1}{M^2}\left(\omega\frac{d^3\sigma^\gamma}{d^3q}\right)_{\mathbf{q}=\mathbf{p}_++\mathbf{p}_-} . \tag{3.5}$$

This equation links the cross section for production of dileptons via virtual photon bremsstrahlung to the bremsstrahlung cross section for real photons. In the above, $\mathbf{p}_\pm$ is the three-momentum of the electron or positron, $E_\pm$ is the energy, $M^2 = (p_+ + p_-)^2$ is the dilepton invariant mass squared, $\mathbf{q}$ is the photon momentum and ω is its energy. The fine structure constant appears as α.

The derivation of soft photon formulae in the context of bremsstrahlung emission of lepton pairs has recently been re-analyzed [21]. It was shown that Rückl's formula was not properly Lorentz-covariant and did not contain the relationship between dilepton cross section and virtual photon cross section that is required by gauge invariance [92]. We will derive some leading-order and next-to-leading order formulæ for dilepton emission from nucleon-nucleon bremsstrahlung in this work.

Consider the reaction

$$p_1 + p_2 \rightarrow p_1^{'} + p_2^{'} + e^+e^- \tag{3.6}$$

where $p_1, p_2, p_1^{'}$ and $p_2^{'}$ represent the four-momenta of the initial and final state nucleons, respectively. The schematic Feynman diagrams for the contributions to the emission of a virtual photon are shown in Fig.3.0. The circle represents the strong interaction.

In the limit of soft photons, real or virtual, the radiation from the strong interaction blob (Fig.3.0(d)) and seagull graphs (Fig.3.0(c)) is a sub-leading contribution [91]. The leading-order contributions of lepton pair emission, which are represented by Fig.3.0(a) and (b), should be added coherently. Note in passing that there have been arguments that bremsstrahlung from *np* reactions should be significantly more important than that from *pp*. These were based on the fact that, nonrelativistically, the first non-vanishing multipole contribution for *pp* appears at the quadrupole level, whereas for *np* it is at the dipole stage. It has however been recently shown that such arguments do not hold for relativistic collisions [86]. In fact, the dilepton yields from these two processes are comparable at 4.9 GeV [86]. We also will discuss *pp* contributions in this work.

Using the Feynman rules of spinor electrodynamics [90], we can immediately write down the contribution to the matrix element $\mathcal{M}_1$ from Fig.3.0(a),

$$\begin{aligned} \mathcal{M}_1 \;=\; & u(p_2, s_2)\Gamma_{22'}\overline{u}(p_2^{'}, s_2^{'})S_F(p_1 - p_1^{'} - q)\overline{u}(p_1^{'}, s_1^{'}) \\ & \Gamma_{11'}\frac{\gamma\cdot(p_1 - q) + m}{(p_1 - q)^2 - m^2}\gamma^{\mu}u(p_1, s_1)(eQ_1L_{\mu}) \end{aligned} \tag{3.7}$$

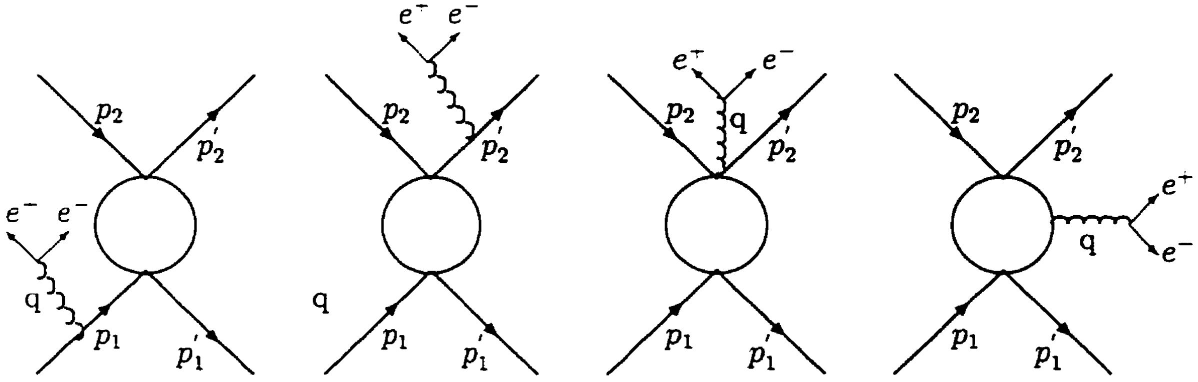

(a) (b) (c) (d)

Fig.3.0: The lepton pairs emission from the nucleon-nucleon collisions.
(a) From the incoming nucleons; (b) From the outgoing nucleons;
(c) From the contact terms; (d) From the internal strong interaction blob.

where q represents the four momentum of the dilepton, and $S_F(p_1 - p_1' - q)$ represents the strong interaction appearing as a circle in Fig.3.0(a). Γ represents a hadronic vertex, L_μ represents the lepton part. Note that $\{\gamma^\mu, \gamma^\nu\} = 2g^{\mu\nu}$ and $(\gamma \cdot p_1 - m)u(p_1, s_1) = 0$, we then obtain

$$\frac{[\gamma \cdot (p_1 - q) + m]}{2p_1 \cdot q - q^2}\gamma^\mu u(p_1, s_1) = u(p_1, s_1)\frac{[2p_1^\mu - (\gamma \cdot q)\gamma^\mu]}{2p_1 \cdot q - q^2} \tag{3.8}$$

Anticipating the soft photon limit, we assume that the hadronic part of the total matrix element is unaffected by the fact that one of its legs is slightly off-shell. And we further just keep the leading-order of four-momentum q in the current part. Then, Eq. (3.7) can be re-written as

$$\mathcal{M}_1 = \mathcal{M}_0(p_1, p_2, p_1', p_2')\frac{p_1}{p_1 \cdot q}(-eQ_1)L_\mu . \tag{3.9}$$

We have written the on-shell matrix element for elastic nucleon-nucleon scattering as $\mathcal{M}_0$,

$$\mathcal{M}_0(p_1, p_2, p_1', p_2') = u(p_2, s_2)\Gamma_{22'}\overline{u}(p_2', s_2')S_F(p_1 - p_1')\overline{u}(p_1', s_1')\Gamma_{11'}u(p_1, s_1) \tag{3.10}$$

Summing the amplitudes of all the relevant Feynman diagrams represented by Fig.3.0 (a) and (b), we label it as $\mathcal{M}$, and further squaring it and also summing over the spins of the final-state leptons, we obtain

$$\sum_{s_+ s_-} |\mathcal{M}|^2 = 4\pi\alpha \, |\mathcal{M}_0|^2 \, J^\mu J^\nu L_{\mu\nu} \, . \tag{3.11}$$

In the above,

$$J^\mu = -Q_1 \frac{p_1^\mu}{p_1 \cdot q} - Q_2 \frac{p_2^\mu}{p_2 \cdot q} + Q_1' \frac{p_1'^\mu}{p_1' \cdot q} + Q_2' \frac{p_2'^\mu}{p_2' \cdot q} \tag{3.12}$$

is the hadron electromagnetic current, and the lepton tensor is

$$L^{\mu\nu} = \frac{8\pi\alpha}{M^4} \left(2\left(p_+{}^\mu p_-{}^\nu + p_-{}^\mu p_+{}^\nu\right) - M^2 g^{\mu\nu} \right) \, . \tag{3.13}$$

The Q's and p's represent charges and four-momenta for the particles, and $q^\mu = (p_+ + p_-)^\mu$. Note that $J^\mu q_\mu = 0$, as a consequence of electromagnetic gauge invariance.

After performing the appropriate contractions and relativistic kinematic calculations, we may write the differential cross section for e^+e^- pair production with invariant mass M and energy q_0 as (please refer to the next chapter for the detailed derivation):

$$\frac{d\sigma^{e^+e^-}}{dM^2} = \frac{\alpha^2}{3\pi^2} \frac{\hat{\sigma}(s)}{M^2} \int_M^{\frac{(s+M^2-4m^2)}{2\sqrt{s}}} \frac{(q_0^2 - M^2)^{\frac{1}{2}}}{q_0^2} \frac{R_2(s_2)}{R_2(s)} dq_0 \tag{3.14}$$

where $R_2(s)$ is the two particle phase space integral [93] and

$$\frac{R_2(s_2)}{R_2(s)} = \frac{\lambda^{\frac{1}{2}}(s_2)}{\lambda^{\frac{1}{2}}(s)} \frac{s}{s_2} \tag{3.15}$$

with $s_2 = s + M^2 - 2\sqrt{s} q_0$ in the *c.m.* $p_1 + p_2$ frame, the kinematic function

$$\lambda(x, y, z) = x^2 + y^2 + z^2 - 2(xy + xz + yz) \tag{3.16}$$

and the weighted cross section

$$\hat{\sigma}(s) \equiv \int_{-(s-4m^2)}^{0} dt \frac{d\sigma_{ab\to cd}}{dt} \left(q_0^2 |\epsilon \cdot J|^2 \right) . \tag{3.17}$$

here ϵ is the polarization of the emitted real or virtual photon.

In the evaluation of the original Feynman diagrams, we have neglected the four-momentum q of the virtual photon in the phase-space δ function in order to obtain the *on-shell* elastic nucleon-nucleon cross section. Because of this approximation, we include

[94] the ratio of two-body phase space [93] $R_2(s_2, m^2, m^2)/R_2(s, m^2, m^2)$ to restore energy conservation. This correction restores energy-momentum conservation and thus has a significant effect on dilepton distributions. The ratio constructed from Eq. (3.14) with and without the phase space correction factor drops monotonically to zero in the limit of maximum invariant mass. Handling the phase-space properly is quite important.

By summing up the coherent superposition, the squared modulus of the polarization dotted into the current, Eq. (3.12), for equal-mass two-body scattering ($m_1 = m_2 = m$) reads [91]

$$\begin{aligned} q_0^2|\epsilon \cdot J|^2 \;=\; & -(Q_1^2 + Q_2^2 + Q_1'^2 + Q_2'^2) \\ & - 2(Q_1 Q_2 + Q_1' Q_2')\frac{s - 2m^2}{\sqrt{s(s - 4m^2)}} ln\left(\frac{\sqrt{s} + \sqrt{s - 4m^2}}{\sqrt{s} - \sqrt{s - 4m^2}}\right) \\ & - 2(Q_1 Q_2' + Q_2 Q_1')\frac{s - 2m^2 + t}{\sqrt{(s + t - 4m^2)(s + t)}} ln\left(\frac{\sqrt{s + t} + \sqrt{s + t - 4m^2}}{\sqrt{s + t} - \sqrt{s + t - 4m^2}}\right) \\ & + 2(Q_1 Q_1' + Q_2 Q_2')\frac{2m^2 - t}{\sqrt{t(t - 4m^2)}} ln\left(\frac{\sqrt{4m^2 - t} + \sqrt{-t}}{\sqrt{4m^2 - t} - \sqrt{-t}}\right) \end{aligned} \tag{3.18}$$

where t is the four-momentum transfer and $s \geq 4m^2$, $-(s - 4m^2) \leq t \leq 0$. Suppose the momentum transfer is small relative to the mass in the problem (specifically,$|t| \leq 4m^2$) , a good approximation to the electromagnetic factor for p-n scattering is:

$$q_0^2\, |\epsilon \cdot J|^2_{ab \to cd} \simeq \frac{2}{3}\left(\frac{-t}{m_N^2}\right) \tag{3.19}$$

then the weighted cross section reduces to

$$\hat{\sigma}_a(s) = \frac{2}{3}\int_{-(s-4m_N^2)}^{0} \left(\frac{-t}{m_N^2}\right) \frac{d\sigma_{nn}^{el}}{dt} dt \tag{3.20}$$

Furthermore, if the differential cross section is symmetric about $\theta_{cm} = 90^0$,or equivalently $d\sigma_{nn}/dt$ is a symmetric function of u and t, then we get:

$$\hat{\sigma}_s(s) = \frac{4}{3}\sigma_{nn}^{el}(\frac{s}{4m_N^2} - 1) \tag{3.21}$$

where σ_{nn}^{el} is the total elastic nucleon-nucleon collision cross section. We comment immediately on the reality of this approximation.

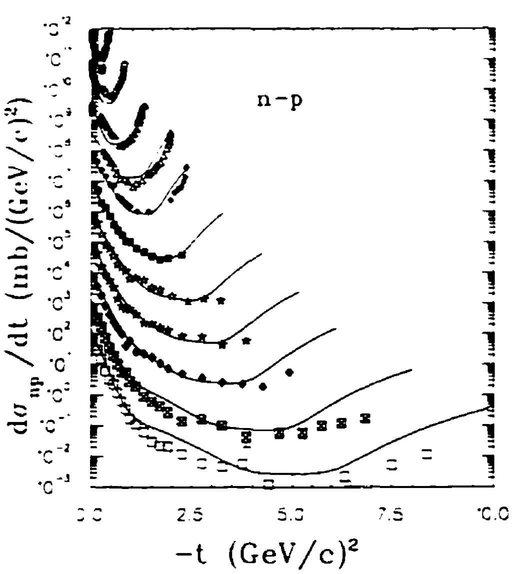

Figure 3.1: The comparisons between the parametrization for the n-p differential elastic cross section and the experimental data at kinetic energy E_{kin} (from top to bottom): 0.21, 0.414, 0.65, 1.028, 1.25, 1.741, 2.252, 2.752, 3.25, 4.25, 5.252 GeV. The Scaling factor for E_{kin}=0.21 GeV is 2×10^9, for E_{kin}=0.414 is 4×10^8 and 0.65 GeV is 4×10^7, else is from 1 to 10^7 starting from the bottom in steps of 10.

Several previous n-p bremsstrahlung calculations use the symmetric weighted cross-section $\bar{\sigma}_s(s)$ [13, 14]. At kinetic energy less than 1 GeV, this should be a good approximation, as for np elastic collisions, $d\sigma/dt$ is nearly symmetric for such low energy. But at higher energies, the observed distributions are not symmetric about $\theta_{c.m.} = 90°$ but rather develop a stronger forward peak. This asymmetry increases with the scattering energy and can suppress the np bremsstrahlung contribution to dilepton production by a factor of 4 at 4.9 GeV [86, 89]. We choose to parametrize the n-p and p-p elastic differential cross sections with functional forms that can fit the experimental data up to energies of 6 GeV with the necessary accuracy. Please refer to Fig. 3.1 and Fig. 3.2 to see how good the fit is. The experimental data are taken from Ref. [95] and Ref. [96].

In Fig. 3.3, the comparison between the momentum transfer weighted cross sections $\sigma_a(s)$ and $\sigma_s(s)$ for n-p scattering, and Eq. (3.17) with Eq. (3.18) leading to $\bar{\sigma}(s)$ for both n-p and p-p collisions against the invariant energy of the system is plotted. We view this comparison as a test for the effects of small t approximation and the symmetric approximation for n-p differential elastic cross section $\frac{d\sigma_{np}^{el}}{dt}$. The forward peak in the $\frac{d\sigma_{np}^{el}}{dt}$ distribution

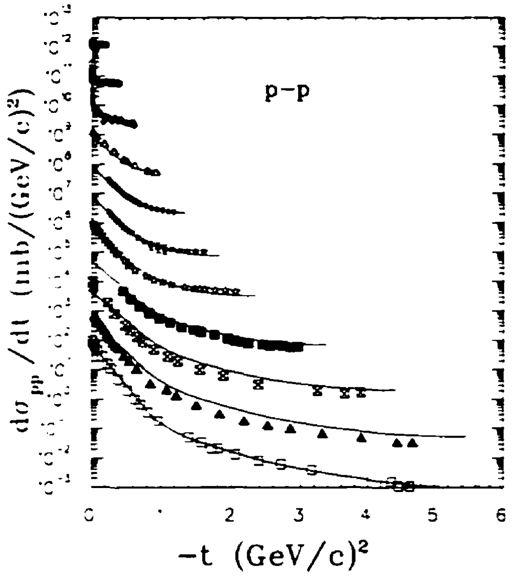

Figure 3.2: The comparisons between the parametrization for the p-p differential elastic cross section and the experimental data at kinetic energy E_{kin} (from the top to the bottom): 0.21, 0.414, 0.65, 1.0, 1.27, 1.73, 2.21, 3.17, 4.149, 5.135, 6.124 GeV. The scaling factor if from 1 to 10^{10} from bottom to top in steps of 10.

leads to a smaller weighted cross-section than that from the symmetric parametrization, for kinetic energies larger than 1 GeV, where the asymmetric parametrization is effective. In the low energy region up to 1.2 GeV , the weighted cross section for p-p is negligibly small compared with that for n-p. But it becomes comparable in high energies. At kinetic energy more than 1 GeV. it is thus imperative to have an accurate parametrization for the elastic nucleon-nucleon differential cross section $d\sigma/dt$ over a relevant range in t.

In all of the above comparisons, we have consistently set $q = 0$ in the 4-dimensional phase space delta function. We now avoid making this approximation and investigate the consequences (full phase space approach). The many-body Lorentz-invariant phase space can be expressed in terms of Mandelstam-type invariants [93], or in this case one can perform the integrals directly. We leave the detailed derivation of the procedure for the next chapter and we simply write down the result

$$\frac{d\sigma^{e^+e^-}}{dM^2} = \frac{\alpha^2}{24\pi^3}\sqrt{s(s-4m^2)}\frac{1}{M^2}\int \frac{(-J^2)}{|\vec{q}|}\frac{d\sigma_{nn}}{dt}\,dy\,dq_\perp^2\,d\phi\,dE_2', \qquad (3.22)$$

where y is the dilepton rapidity, E_2' is one of the nucleon energy in the final state, $q_\perp$ and ϕ are the dilepton transverse momentum and azimuthal angle, respectively. The electron

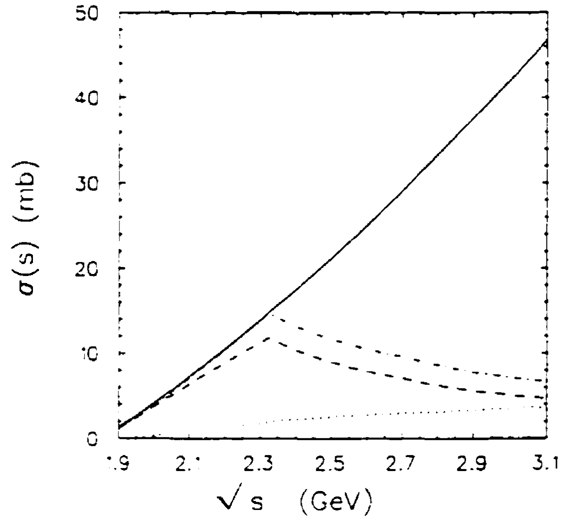

Figure 3.3: Comparisons of the momentum transfer weighted cross sections (see the text) for n-p and p-p , respectively, as a function of invariant energy. The solid line refers to the n-p symmetric parametrization $\hat{\sigma}_s$, the dot-dashed line is for n-p unsymmetric parametrization $\hat{\sigma}_a$ (small t approximation), and the dashed line and the dotted line give the exact results for $\hat{\sigma}$ with Eq.(3.17) and Eq.(3.18) for n-p and p-p scattering.

mass μ has been set to $\mu = 0$.

Note that $\mathcal{M}_0(p_1, p_2, p_1', p_2')$ depends on the virtual photon four-momentum q at the zeroth order, and J^μ at the order -1. Now we evaluate the next-to-leading order. Suppose $\mathcal{M}_0$ in Eq. (3.10) is slightly off-shell, then the first-order derivative $\Delta\mathcal{M}$ of $\mathcal{M}_0$ should be a function of q at the order 1. Let ΔJ represent the correction of the current J^μ to order 0. Rewrite the matrix $\mathcal{M}$ in the following form,

$$\begin{aligned}\mathcal{M} &= (\mathcal{M}_0 + \Delta\mathcal{M})(J + \Delta J)^\mu \\ &\approx \mathcal{M}_0 J^\mu + \mathcal{M}_0 \Delta J^\mu + \Delta\mathcal{M} J^\mu \end{aligned} \tag{3.23}$$

where

$$\Delta J^\mu = Q_1 \frac{(\gamma \cdot q)\gamma^\mu}{2p_1 \cdot q} + Q_2 \frac{(\gamma \cdot q)\gamma^\mu}{2p_2 \cdot q} + Q_1' \frac{(\gamma \cdot q)\gamma^\mu}{2p_1' \cdot q} + q_2' \frac{(\gamma \cdot q)\gamma^\mu}{2p_2' \cdot q} \tag{3.24}$$

and $\Delta\mathcal{M}$ can be obtained by writing

$$\mathcal{M}_0(p_i \pm q) = \mathcal{M}_0 \pm q^\alpha \frac{\partial \mathcal{M}_0}{\partial p_i^\alpha} \tag{3.25}$$

However, the amplitude expressed in Eq. (3.23) is not gauge-invariant. Gauge-invariance is restored by the contribution from the contact term (seagull graphs represented by

Fig.3.0(c)), which can be obtained by the minimal electromagnetic substitution $p^{\alpha} \rightarrow p^{\alpha} - eQg^{\alpha\mu}$ then take the first derivative of the expansion for $\mathcal{M}_0(p_i^{\alpha} - eQ_i g^{\mu\nu})$,

$$C_0^{\mu} = \sum_i -eQ_i \frac{\partial \mathcal{M}_0}{\partial p_{i\mu}} \tag{3.26}$$

Putting all the contributions together. Eq. (3.11) can be rewritten up to next-to-leading order in q as follows

$$\sum_{s_+ s_-} |\mathcal{M}|^2 = 4\pi\alpha H^{\mu\nu} L_{\mu\nu} \tag{3.27}$$

where

$$\begin{aligned} H^{\mu\nu} &= [(\mathcal{M}_0 + \Delta\mathcal{M})(J + \Delta J)^{\mu} + C_0^{\mu}]\,[(\mathcal{M}_0 + \Delta\mathcal{M})(J + \Delta J)^{\nu} + C_0^{\nu}] \\ &\approx \mathcal{M}_0^2 J^{\mu} J^{\nu} + \mathcal{M}_0\,[J^{\mu}(\mathcal{M}_0 \Delta J^{\nu} + \Delta\mathcal{M} J^{\nu} + C_0^{\nu}) + (\mathcal{M}_0 \Delta J^{\mu} + \Delta\mathcal{M} J^{\mu} + C_0^{\mu}) J^{\nu}] \\ &\approx |\mathcal{M}_0|^2 J^{\mu} J^{\nu} + \frac{1}{2} \sum_{i,j} \frac{Q_i Q_j'}{(p_i \cdot q)(p_j \cdot q)} \frac{\partial |\mathcal{M}_0|^2}{\partial p_i^{\beta}} p_{i\alpha} \\ &\times \left[p_j^{\mu}(g^{\nu\alpha} q^{\beta} - g^{\nu\beta} q^{\alpha}) + p_j^{\nu}(g^{\mu\alpha} q^{\beta} - g^{\mu\beta} q^{\alpha})\right] \end{aligned} \tag{3.28}$$

To simplify the formula. we have used the convention $Q_j' = -Q_j$ for the incoming nucleons and $Q_j' = Q_j$ for the outgoing nucleons.

The differential cross section for dielectron emission up to next-to-leading order now reads

$$\begin{aligned} \frac{d\sigma^{e^- e^-}}{dM^2} &= \frac{\alpha^2}{24\pi^3} \sqrt{s(s - 4m^2)} \frac{1}{M^2} \int \frac{1}{|\vec{q}|} [(-J^2) \frac{d\sigma_{nn}}{dt} + \sum_{i,j} \frac{Q_i Q_j'}{(p_i \cdot q)(p_j \cdot q)} \\ &\times \left((p_i \cdot q) p_j^{\beta} - (p_i \cdot p_j) q^{\beta}\right) \frac{\partial(\frac{d\sigma_{nn}}{dt})}{\partial p_i^{\beta}}] dy dq_{\perp}^2 d\phi dE_2' \end{aligned} \tag{3.29}$$

On Fig. 3.4 we display three different curves for the case of p-n scattering, at energies of 0.5, 1.0 and 2.0 GeV. We compare calculations done with Eq. (3.14), calculations done with Eq. (3.22) and Eq. (3.29). The three approaches display general behaviors that are similar. But there are some effects that can be seen from this figure. At each energy, the difference between the solid line and the dotted line is the subleading-order contribution. At low energy and low invariant dilepton mass M, this effect is really small. The largest contribution occurs at high invariant mass M and high energies. Since the subleading formula is not appropriately defined there, we should not take the large subleading effect at high M too quantitatively. This only serves as an indication. Comparisons between the solid line and the dot-dashed line at each energy display the effect of approximating the phase space. The largest deviations are at low kinetic energies and low M. Recall that the "soft photon limit" is not really properly defined by $M \to 0$.

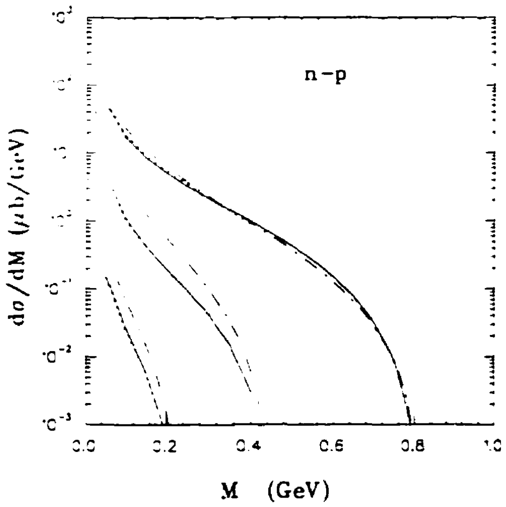

Figure 3.4: We plot the differential cross section for production of lepton pairs of invariant M in the case of p-n collisions at kinetic energies of 0.5, 1.0 and 2.0 GeV (bottom to top curves, respectively). The solid lines represent calculations done with Eq. (3.22), full phase space; the dotted lines represent the calculation results with Eq. (3.29), next to leading order; and the dot-dashed lines are done using Eq. (3.14), soft approximation. The scaling factor is 1 at 0.5 GeV, 10 at 1.0 GeV and 100 at 2 GeV.

Another useful comparison is the relative radiative intensities from pp and np scattering. As mentioned above, pp bremsstrahlung has often been neglected because of a classical multipole argument. We examine the relative importance of proton-proton and neutron-proton bremsstrahlung here, with the full phase space approach (Eq. (3.22)). The relative intensities depend on kinetic energy as shown in Fig. 3.5 which presents the ratio $R=(\frac{d\sigma}{dM})_{pp}/(\frac{d\sigma}{dM})_{np}$ as a function of invariant mass at different kinetic energies. Proton-proton bremsstrahlung becomes more and more important as the kinetic energy increases.

We also calculated the angular distribution of the bremsstrahlung dileptons. Angular

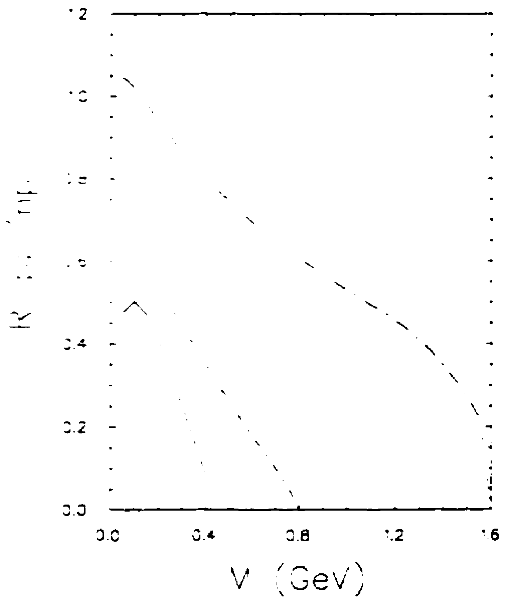

Figure 3.5: The ratio of dilepton production cross section in pp and np reactions, R=$(\frac{d\sigma}{dM})_{pp}/(\frac{d\sigma}{dM})_{np}$, as a function of invariant mass M at kinetic energies 1.0, 2.0, 3.0 and 4.9 GeV, from bottom to top.

anisotropies have recently been put forward as a means of distinguishing between competing lepton pairs production sources [97, 98]. This argument has power only if the angular distributions of those sources can reliably be calculated.

Owing to collision dynamics, the polarization of the virtual photon eventually converting into a lepton pair may be such that, in the rest frame of the dilepton, the single lepton distribution may not be isotropic [23]. This is the essence of the idea. Following Ref. [97], we write the differential cross section for emission of a lepton pair of invariant mass M, with a lepton coming out at a polar angle θ in the rest frame of the lepton pair as

$$S(M,\theta) = \frac{d\sigma}{dM^2 d\cos\theta} = A(1 + B\cos^2\theta) \tag{3.30}$$

This enables us to write the polar anisotropy coefficient, B, as

$$B = \frac{S(M,\theta = 0^o)}{S(M,\theta = 90^o)} - 1 \tag{3.31}$$

Since the full phase space is obviously crucial to the proper kinematics, we use methods which will be discussed in detail in the next chapter. Here, we simply give the results.

In Fig. 3.6. we plot the coefficient B as a function of invariant mass M, with the leading- and next-to-leading-order formalism, for the kinetic energies 0.5 and 1 GeV. The next-to-leading contribution has shifted the curves upwards a little bit. For further results at higher energies, please refer to Ref. [23]. There, we have shown that the angular anisotropy of the lepton spectrum depends on the details of the calculations. We thus do not include such calculations in the BUU simulations for nucleus-nucleus collisions, for the moment. There are presently no data for this quantity.

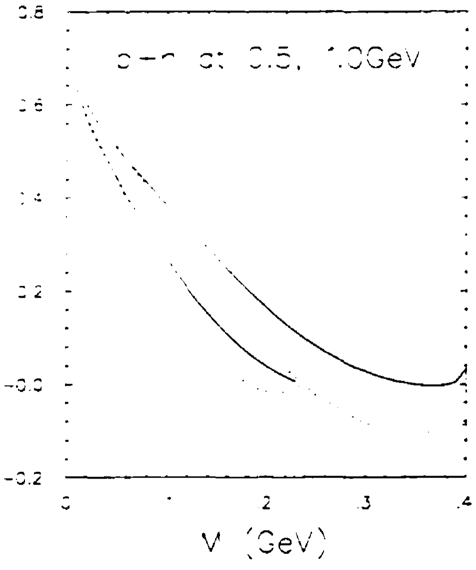

Figure 3.6: We plot the polar anisotropy coefficient, as defined in the text, against lepton pair invariant mass M in the case of p-n collisions at kinetic energies of 0.5, 1.0 GeV/nucleon. The dotted curves represent calculations done with leading order, the solid curves represent the calculation results to subleading order.

Finally, we get the differential lepton pair yields in nucleus-nucleus collisions at a given impact parameter, b :

$$\frac{dN^{e^-e^-}(b)}{dM^2} = \sum_{p-p,n-p} \frac{d\sigma^{e^+e^-}}{dM^2} \frac{1}{\sigma_{NN}} W_p \tag{3.32}$$

where σ_{NN} is the total nucleon-nucleon cross section and

$$W_p = \frac{1}{4\pi} \int d\Omega [1 - f(\vec{r}, \vec{p}_1', t)][1 - f(\vec{r}, \vec{p}_2', t)] \tag{3.33}$$

is the effect of Pauli Blocking of the final state phase space, $\vec{r}$ and t give the space time coordinates of each collision, $\vec{p}_1'$ and $\vec{p}_2'$ are the final momenta of the collided nucleons, and f is the phase space occupation density as in chapter 2.

The dilepton differential cross sections from the nucleus-nucleus collisions thus can be obtained by integrating over the impact parameter

$$\frac{d^2\sigma^{e^+e^-}}{dM^2} = \int d^2b \frac{dN^{e^+e^-}(b)}{dM^2}. \tag{3.34}$$

3.3 Dalitz-Decay

The main processes of Dalitz decay of hadrons which contribute to the dielectron production considered here are Δ and η-meson decays. The Dalitz decay of π^0 is neglected due to the low invariant mass of the produced dileptons.

The contributions of the Δ and η-meson decay to the dielectron yields in heavy ion collisions can be considered as a two-step process in which at first the Δ or η-meson is formed in the inelastic N-N reactions and then decays into a dielectron pair.

3.3.1 Δ Dalitz Decay

For the derivation of the $\Delta \rightarrow N\gamma$ amplitude, we start from the interaction Lagrangian [102]

$$\mathcal{L} = eA^\mu \overline{\Psi}^\beta_\Delta \Gamma_{\beta\mu} \Psi_N \tag{3.35}$$

where $\Gamma_{\beta\mu}$ is

$$\begin{aligned} \Gamma_{\beta\mu} &= G_1(q^2)\Gamma^1_{\beta\mu} + G_2(q^2)\Gamma^2_{\beta\mu} + G_3(q^2)\Gamma^3_{\beta\mu} \\ &= G_M(q^2)\Gamma^M_{\beta\mu} + G_E(q^2)\Gamma^E_{\beta\mu} + G_C(q^2)\Gamma^C_{\beta\mu} \end{aligned} \tag{3.36}$$

which includes the contributions from magnetic dipole $G_M(q^2)\Gamma^M_{\beta\mu}$, electric quadrupole $G_E(q^2)\Gamma^E_{\beta\mu}$, and Coulomb quadrupole interactions $G_C(q^2)\Gamma^C_{\beta\mu}$. $G_i(q^2)$ is a corresponding formfactor. The $\Gamma^1_{\beta\mu}, \Gamma^2_{\beta\mu}$, and $\Gamma^3_{\beta\mu}$ have the form

$$\begin{aligned} \Gamma^1_{\beta\mu} &= (q_\beta\gamma_\mu - q\cdot\gamma g_{\beta\mu})\gamma_5 \\ \Gamma^2_{\beta\mu} &= (q_\beta p_\mu - q\cdot p g_{\beta\mu})\gamma_5 \\ \Gamma^3_{\beta\mu} &= (q_\beta q_\mu - q^2 g_{\beta\mu})\gamma_5 \end{aligned} \tag{3.37}$$

where $p = \frac{1}{2}(p_\Delta + p_N)$, $q = p_\Delta - p_N$. The p_Δ, p_N and q represent the four momenta of delta, nucleon and virtual photon, respectively. Thus, $q^2 = M^2$, $p_\Delta^2 = m_\Delta^2$, $p_N^2 = m_N^2$. We further just keep the dominant magnetic dipole term and use

$$\Gamma^M_{\beta\mu} = f \cdot E_{\beta\mu}, \tag{3.38}$$

with

$$\begin{aligned} E_{\beta\mu} &= -m_\Delta \Gamma^1_{\beta\mu} + \Gamma^2_{\beta\mu} + \frac{1}{2}\Gamma^3_{\beta\mu}; \\ f &= G_M(q^2)[-\frac{3}{2}\frac{1}{m_N}\frac{m_N + m_\Delta}{(m_\Delta + m_N)^2 - M^2}] \end{aligned} \tag{3.39}$$

The differential probability of the Δ decay into dileptons with invariant mass M reads

$$\frac{d\Sigma_\Delta}{dM^2} = \frac{\alpha}{3\pi M^2} B_\gamma(m_\Delta) R(m_\Delta, M^2) \tag{3.40}$$

where

$$B_\gamma(m_\Delta) = \frac{\Gamma_0(m_\Delta, 0)}{\Gamma_\pi(m_\Delta)}, \qquad R(m_\Delta, M^2) = \frac{\Gamma_0(m_\Delta, M^2)}{\Gamma_0(m_\Delta, 0)}, \tag{3.41}$$

$\Gamma_0(m_\Delta, M^2)$ is the total decay width of Δ into a virtual photon (please refer to Appendix B for the derivation), and the total width of Δ to a pion-nucleon pair is $\Gamma_\pi(m_\Delta)$.

The function $R(m_\Delta, M^2)$ can be written as

$$\begin{aligned} R(m_\Delta, M^2) &= \frac{m_\Delta M^2 + 5m_\Delta q_0^2 - 3m_N M^2 - 3q_0 M^2 - 3m_N q_0^2 - 3q_0^3}{q_0'^2(5m_\Delta - 3m_N - 3q_0')} \\ &\times \left[\frac{(m_\Delta + m_N)^2}{(m_\Delta + m_N)^2 - M^2}\right]^2 \left(\frac{\lambda(m_\Delta^2, m_N^2, M^2)}{\lambda(m_\Delta^2, m_N^2, 0)}\right)^{\frac{1}{2}} \frac{G_M(M^2)}{G_M(0)} \end{aligned} \tag{3.42}$$

with

$$q_0 = \frac{m_\Delta^2 + M^2 - m_N^2}{2m_\Delta}, \qquad q_0' = \frac{m_\Delta^2 - m_N^2}{2m_\Delta} \tag{3.43}$$

In the vector dominance model (VMD) [99], the delta decay would proceed through $\Delta \to N\rho^0 \to N\gamma$. The formulas obtained in Eq.(B.9) and Eq.(3.42) thus need to be multiplied by a VMD form factor $|F_\pi(M)|^2$, which is defined as [100]

$$|F_\pi(M)|^2 = \frac{m_\rho^4}{(M^2 - m_\rho'^2)^2 + m_\rho^2\Gamma_\rho^2} \tag{3.44}$$

with $m_\rho = 0.775$GeV, $m_\rho' = 0.761$GeV and $\Gamma_\rho = 0.118$ GeV.

As an alternate procedure, we directly use the interaction Lagrangian [101]

$$\mathcal{L}_{\rho N\Delta} = i\frac{g_{\rho N\Delta}}{m_N + m_\Delta}\overline{\Psi}^{\mu}_{\Delta}\mathcal{T}(\partial_\nu \rho_\mu - \partial_\mu \rho_\nu)\gamma^\nu \gamma_5 \Psi_N + h.c. \tag{3.45}$$

where $\mathcal{T}$ is the isospin transition matrix, m_N is the nucleon mass, and the coupling constant $g_{\rho N\Delta}$ is from Ref. [101]. And we further apply vector dominance to calculate the width of delta photonic decay in the same fashion as developed above. The obtained differential probability of delta decay into a dilepton pair with invariant mass M for delta mass of 1.13, 1.23, 1.33, 1.43, 1.53 GeV (dotted line) are compared to the results with Eq.(3.40) (solid line) after having added the VMD form factor, in Fig. 3.7. While this figure shows that the difference between the two approaches is small, it in fact illustrates a very important point: the magnetic dipole term in Lagrangian Eq.(3.35) is the dominant contribution to the delta photonic decay. The neglected contributions from the quadrupole interactions $G_E(q^2)\Gamma^E_{\beta\mu}$ and $G_E(q^2)\Gamma^C_{\beta\mu}$ are in fact of higher order [102]. Note that only Δ^- and Δ^0 can decay into dilepton pair due to charge conservation.

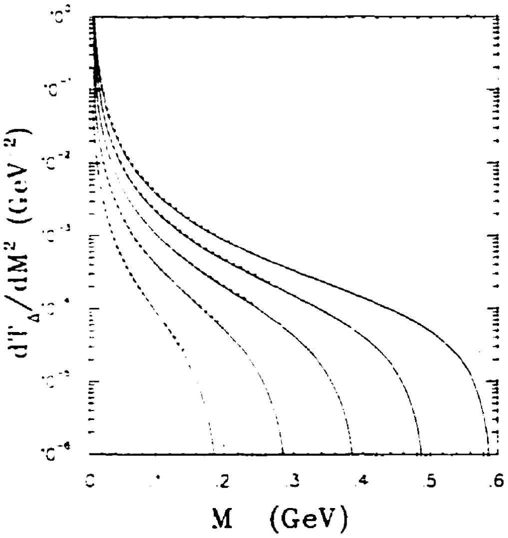

Figure 3.7: The differential probability (Eq.(3.40)) of delta-decay into a lepton pair with invariant mass M for the different delta masses. From the left to right, the curves are for m_Δ=1.13, 1.23, 1.33, 1.43, 1.53 GeV, respectively. Please refer to the text for more details.

In principle, the delta decay contribution to the dilepton pair production should be summed up coherently with the nucleon-nucleon bremsstrahlung amplitudes, as the delta is produced from nucleon-nucleon inelastic scattering. Its decay into virtual photon is indistinguishable from the bremsstrahlung contributions. A recent one-meson-exchange model calculation considered such interference [104]. Their results show that the interference is insignificant at kinetic energy $E_{kin} = 1$ GeV/nucleon, which is the energy we are interested in[1]. Therefore, we believe that the coherent effects from the delta Dalitz decay and bremsstrahlung is negligible at 1 GeV/nucleon, even though a complete study to clear up such an issue is necessary and goes beyond the scope of this work.

3.3.2 η Production and Dalitz Decay

In our BUU approach, the η-mesons mainly come from two classes of elementary processes. The first is

$$NN \to NN\eta, \qquad N\Delta \to NN\eta, \tag{3.46}$$

where N is a nucleon.

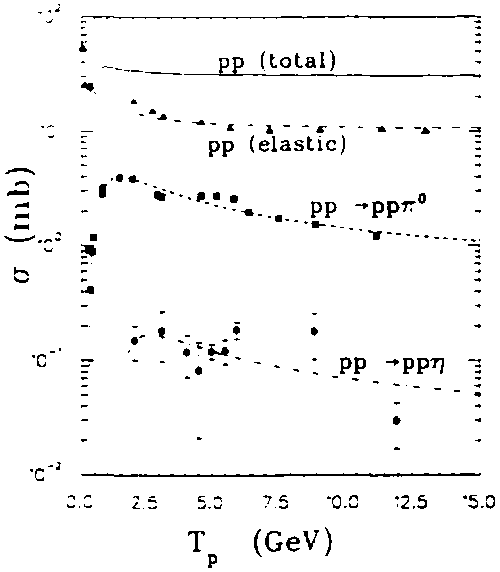

Figure 3.8: Comparisons of the elementary cross sections for η and π^0 production and the experimental data from proton-proton reactions. The elastic and the total p-p cross sections against the projectile proton energy are also shown. The data are from Ref. [106] for $pp \to pp\eta$ and $pp \to pp\pi^0$, and Ref. [108] for elastic p-p cross sections.

---

[1] The delta radiative decay will dominate the virtual bremsstrahlung at this energy.

In Fig. 3.8 . we show the measured cross section for the process $pp \rightarrow pp\eta$ [106] and the total cross section of nucleon-nucleon collisions as a function of the projectile nucleon kinetic energy. It's very easy to see that the cross section of this process is very small compared with the total nucleon- nucleon cross section. The other class of processes involves pions,

$$\pi N \rightarrow N\eta \tag{3.47}$$

where the free pions are produced by the delta decay during the dynamical evolution of the nucleus-nucleus collision. Fig. 3.9 shows that the cross section for this process is also much smaller than the total cross section of πN scattering. Thus, we treat η-meson production in nucleus-nucleus collisions perturbatively. In this method, the probability of producing η-mesons is calculated without taking their energy out of the nucleus-nucleus simulation. This is different from the treatment of pion production, where the processes of Δ decaying into pion and nucleon, and pion fusion with a nucleon into a Δ are treated explicitly with energy and momentum conservation in the simulation, since pions are produced at a much larger rate (see also Fig. 3.8).

For baryon-baryon collisions, we treat the process NN$\rightarrow$NNη as a reaction of two particles into three particles. There are four variables to describe the phase space. The momentum value of η-meson can be set by Monte-Carlo method after the maximum possible value of η-meson momentum is determined with exact kinematics. We parametrize the total cross section for η-meson production process as [107]

$$\sigma_{pp\rightarrow pp\eta}(\sqrt{s}) = \frac{A(\sqrt{s}-\sqrt{s_0})}{B+(\sqrt{s}-\sqrt{s_0})^2} \qquad (mb), \tag{3.48}$$

where A=0.17 mb GeV, B=0.253 GeV^2, $\sqrt{s}$ is the total available energy and the threshold energy $\sqrt{s_0} = 2m_p + m_\eta = 2.424$ GeV. The comparisons of this with the experimental data is made in Fig. 3.8, where the fit to the experimental data is quite reasonable. According to OBE calculations, the cross section for $pn \rightarrow pn\eta$ is considerably larger than that for $pp \rightarrow pp\eta$. The calculated value of the ratio between the cross section of $pn \rightarrow pn\eta$ and $pp \rightarrow pp\eta$ is approximately 3.5 near the threshold and this ratio will decreases to around

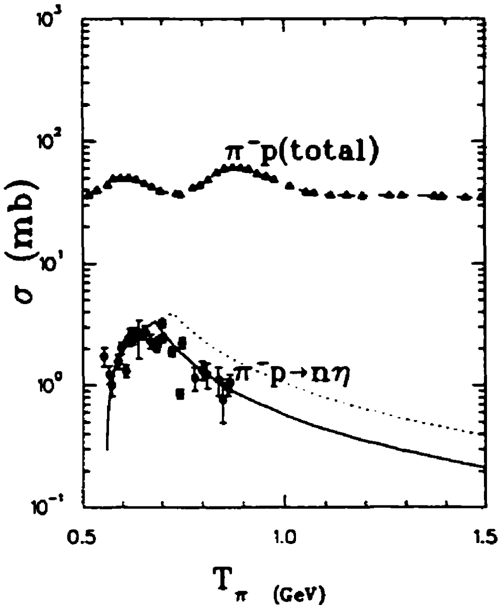

Figure 3.9: Comparisons of the parametrizations of $\pi^- p \to n\eta$ cross sections and the experimental data taken from Ref. [113]. The dotted curve is the parametrization used in Ref. [112]. The solid curve is what we used. The total $\pi^- p$ experimental cross sections against the pion kinetic energy are also shown, which are from Ref. [115].

2.0 with increasing energy $\sqrt{s}$. The first measured results also support this [110]. We use a cross section for $np \to np\eta$ that is three times larger than for pp, and $\sigma_{nn\to nn\eta} = \sigma_{pp\to pp\eta}$. All the other cross sections are given by the corresponding nucleon-nucleon cross sections at the same invariant energy with the appropriate spin average. For pion-nucleon reaction, the η-meson production cross section can be parametrized like

$$
\begin{aligned}
\sigma_{\pi^- p\to\eta n}(\sqrt{s}) &= 13.07(\sqrt{s}-\sqrt{s_0})^{0.5288} \quad (mb) \quad for \quad \sqrt{s_0} < \sqrt{s} < 1.562GeV \\
&\quad 0.8(\frac{1}{\sqrt{s}-\sqrt{s_0}})^{1.452} \quad (mb) \quad for \quad 1.562GeV < \sqrt{s}. \qquad (3.49)
\end{aligned}
$$

where $\sqrt{s_0} = m_n + m_\eta = 1.486$ GeV is the threshold energy. The energy dependence of the cross section of the process $\pi^- p \to n\eta$ with the function of Eq. (3.49) is compared with the experimental data [113] in Fig. 3.9. We calculate the η-meson production directly with this process.

The differential probability of η-meson Dalitz decay into dielectron with invariant mass M is given by [116]

$$
\frac{dw}{dM} = \frac{4\alpha}{3\pi} B_r \frac{1}{M}(1-\frac{M^2}{m_\eta^2})^3 |F_\eta(M)|^2 \qquad (3.50)
$$

where the form factor

$$F_\eta(M) = \frac{1}{1 - \frac{M^2}{\Lambda_\eta^2}}; \tag{3.51}$$

with Λ_η=0.77 GeV, and B_r=0.39 is an experimental branching ratio.

3.4 Pion-Pion Annihilation and Bremsstrahlung

3.4.1 Pion-Pion Annihilation

The $\pi^+\pi^-$ annihilation proceeds through the ρ meson which decays into a virtual massive photon by vector dominance. A standard expression for this annihilation cross section is:

$$\sigma_{\pi^+\pi^-}^{e^+e^-}(M) = \frac{4\pi}{3}\frac{\alpha^2}{M^2}(1 - \frac{4m_\pi^2}{M^2})^{\frac{1}{2}}|F_\pi(M)|^2 \tag{3.52}$$

where $|F_\pi(M)|^2$ is the form factor as defined in Eq.(3.44).

The probability of dilepton production from this process is calculated with the ratio between the pion annihilation cross section given by Eq.(3.52) and the total pion-pion cross section for which we approximately use the pion-pion elastic cross section which is parametrized in the following way [118]:

(a) For $\sqrt{s} \leq$ 0.6GeV the chiral model expression is used:

$$\sigma_{el}(s) = \frac{2}{3}\frac{1}{F_\pi^4}\frac{1}{16\pi}s\left[1 - \frac{5m_\pi^2}{s} + \frac{7m_\pi^4}{s^2}\right] \tag{3.53}$$

with the pion decay constant F_π=0.098 GeV.

(b) At a collision energy near the ρ mass, 0.6$\leq \sqrt{s} \leq$ 1.5 GeV, the largest contribution to $\pi\pi$ scattering amplitude is due to resonance formation. Therefore

$$\sigma_{el}(s) = \frac{g_{\rho\pi\pi}^4}{48\pi s}\frac{(s - 4m_\pi^2)^2}{(s - m_\rho^2)^2 + m_\rho^2\Gamma_\rho^2} \tag{3.54}$$

where the coupling constant $g_{\rho\pi\pi} \cong 6, m_\rho = 0.775$ GeV, and $\Gamma_\rho = 0.155$ GeV.

(c) For large collision energy $\sqrt{s} \geq$ 1.5 GeV, σ_{el} becomes energy independent $\sigma_{el} \cong 5$ mb.

3.4.2 Pion-Pion Bremsstrahlung

As another possible source for the dilepton production, pion-pion radiation can be handled in the same way as nucleon-nucleon bremsstrahlung in the section **3.2**. The momentum transfer weighted cross section for $\pi^+\pi^0$, $\pi^-\pi^0$ and $\pi^+\pi^-$ processes (the cross section of the other isospin channels are relatively small) then are

$$\dot{\sigma}(s) = \frac{4}{3}\sigma^{el}_{\pi\pi}(s)(\frac{s}{4m_\pi^2} - 1)[\frac{4}{3} + \frac{1}{2}f(s)] \tag{3.55}$$

with

$$\begin{aligned} f(s) \quad = \quad & \frac{s}{2(s-4m_\pi^2)} - \frac{s-4m_\pi^2}{2s} - \frac{m_\pi^2}{s}\left\{\frac{2\sqrt{s}}{\sqrt{s-4m_\pi^2}} + \left(\frac{\sqrt{s}}{\sqrt{s-4m_\pi^2}}\right)^3\right. \\ & \left. + \frac{\sqrt{s-4m_\pi^2}}{\sqrt{s}}\right\} \ln\left(\frac{\sqrt{s}+\sqrt{s-4m_\pi^2}}{\sqrt{s}-\sqrt{s-4m_\pi^2}}\right). \end{aligned} \tag{3.56}$$

Calculations for such $\pi\pi$ bremsstrahlung processes will be discussed in detail in the next chapter. There, we perform a calculation using σ and ρ meson exchange to model the strong interaction.

The comparisons of the differential dilepton cross sections at invariant mass M from pion-pion bremsstrahlung at different pion kinetic energies are made in Fig. 3.10. In the region of low invariant mass M of dileptons, this differential cross section is large compared to n-p bremsstrahlung in Fig. 3.4 for a single collision event. But the number of N-N collisions is much larger than that of pion-pion collisions in the heavy ion reaction. These two effects will go against each other, it's still possible that the contribution of the pion-pion bremsstrahlung is important relative to n-p radiation. The dynamical results will be discussed in the next section. The pion-nucleon bremsstrahlung is neglected as its contribution has been shown negligible in comparison with the n-p source [13, 14]. The cross section for $\pi^+\pi^-$ annihilation is also plotted in Fig. 3.10, which will mainly contribute to large invariant mass dilepton yields.

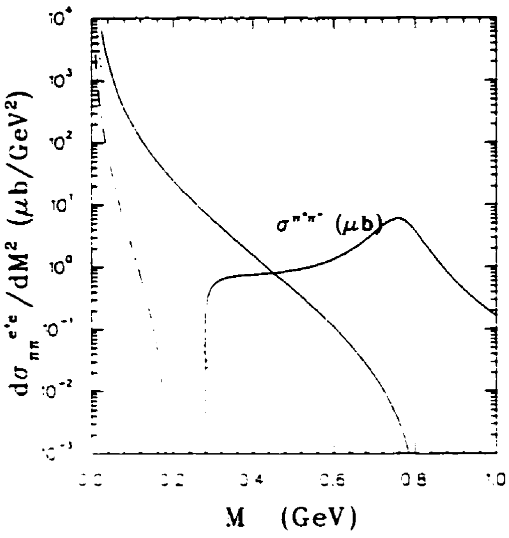

Figure 3.10: The differential cross sections of pion-pion bremsstrahlung at the pion kinetic energies: 0.5 GeV (dashed-dotted line), 1.0 GeV (dotted line), 4 GeV (solid line), against the lepton pair invariant mass M. The solid curve marked $\sigma^{\pi^+\pi^-}$ is for the pion-pion annihilation cross section.

3.5 Dynamical Results

The BUU equation is solved with the test particle method, and the dynamical evolution is divided into time steps as described in chapter **2**. The number of the parallel events used was 200 and the time step 0.3 fm/c. Since both the neutron-proton and proton-proton bremsstrahlung will not affect the final state of two collided particles much due to the small probability, we treat the dielectron production from the nucleon-nucleon radiation perturbatively like the $\eta - meson$ production described in section **3.3.2**. The Dalitz decay of delta is also calculated perturbatively, because the duration of the dynamical evolution of nucleus-nucleus collision is less than 30 fm/c in the energy range of our interest, which is small compared with the half-life of delta decay into a virtual photon. Furthermore, the delta can decay into pion and nucleon, the half-life of this process is much shorter than its photonic decay. In our treatment, the deltas are produced not only from the nucleon-nucleon collisions but also from the pion-nucleon fusions. The total probability of dielectron production is calculated by adding the contributions from neutron-proton, proton-proton, pion-pion bremsstrahlung, the Dalitz decay of delta and η-meson, and finally the $\pi^-\pi^-$ annihilation. The real dilepton production cross section is then obtained by dividing by the number of simulations and integrating over the impact parameter.

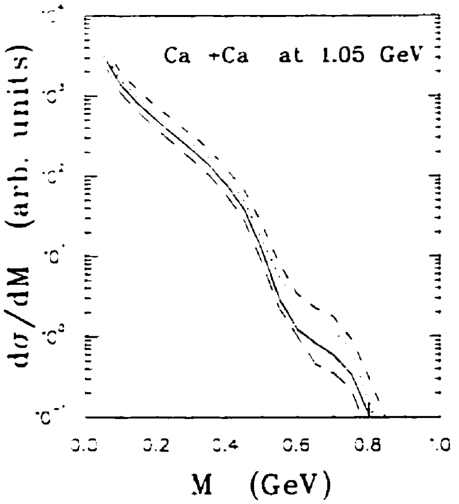

Figure 3.11: The dielectron invariant mass spectra for reactions Ca + Ca, impact parameter b=1.2 fm at kinetic energy 1.05 GeV/nucleon with solid lines: NMDYI (K=210 MeV), long-dashed lines: hard MDYI (K=380 MeV), dotted lines: Hard (K=380 MeV, momentum independent), dashed lines: Soft (K=210 MeV, momentum independent) potentials.

As a first calculation, we test the nuclear EOS effects on the dielectron spectra for the reactions Ca + Ca at an impact parameter b=1.2 fm at kinetic energy 1.05 GeV/nucleon. The results are shown in Fig. 3.11. The calculations were done with the soft (K=210 MeV), hard (K=380 MeV) momentum independent potentials, and NMDYI (K=210 MeV), hard MDYI (K=380 MeV) momentum dependent potentials (see chapter **2** for the details of these interactions). To clearly display the nuclear EOS effects, the relative ratio of the dielectron spectra are also plotted (see Fig. 3.12). One can see that the dielectron spectrum is sensitive to the momentum dependent features and to the variation in the nuclear compressibility K. The momentum dependent mechanism decreases the dielectron spectrum nearly by a factor of 2, while the variation of K from 210 to 380 MeV generates differences exceeding 30%, owing to the complex collision dynamics. As we will see later, the dielectron spectrum reveals that the η-meson Dalitz decay is the dominant source at low invariant masses and pion-pion annihilation is a very important one for the high invariant mass range. The EOS effects on the η-meson and pion total cross sections for Ca

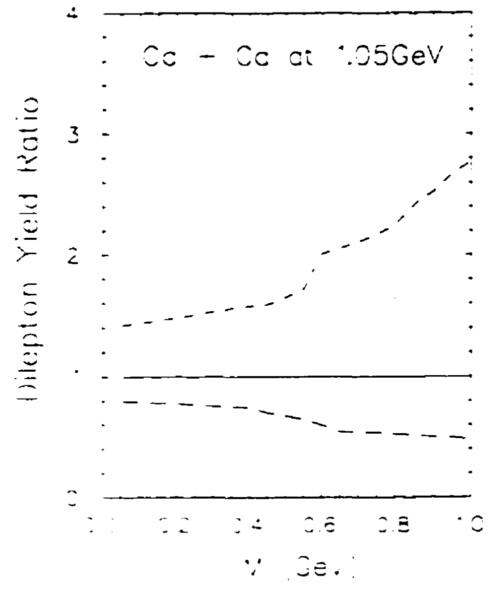

Figure 3.12: The ratio of the dielectron invariant mass spectra for the reaction Ca + Ca. at impact parameter b=1.2 fm and for kinetic energy 1.05 GeV/nucleon. Long-dashed line: HM (hard MDYI, K=380 MeV), dotted line: Hard (K=380 MeV, momentum independent), dashed line: Soft (K=210 MeV, momentum independent). The common denominator in these ratios is the result with the NMDYI potential (K=210 MeV), (solid line).

+ Ca system at 1.05 GeV/nucleon, b=1.2 fm are recorded in table 3.1, which shows that the η yields are somewhat sensitive to the EOS, while the pions are less sensitive [117]. Our calculation shows that the contribution to the η yield from π-nucleon sources dominates over the nucleon-nucleon channels, the sensitivity of the η-meson to the nuclear EOS may be understood from the feature of π-nucleon cross sections: a little energy change could lead to large cross section variations. The η-meson decay contribution to the dielectron spectra depends on the η total numbers. Thus it is very important to reproduce the experimental measurement of this quantity. We have calculated the impact parameter dependence of the η yield for Ca + Ca at 1.05 GeV/nucleon with the NMDYI potential and this is displayed in Fig. 3.13. Note a scaling factor of 300 is applied in order to directly compare with the experimental data. The recent measurement of η*300 yields 23.5±9.5 for central collisions [114]. Fig. 3.13 shows that our results with NMDYI potential are within the error bar of the measurement, especially after considering the necessary integration over the central region in order to directly compare with the data.

Table 3.1: The η and π total yields from Ca + Ca collisions at impact parameter b=1.2 fm. E_{kin} = 1.05GeV/nucleon, with four different potentials: Hard, Soft, NMDYI and HM. The η yields are multiplied by 300.

Potential	η	π	π^-	π^0	π^-
Soft	53.28	11.18	3.76	3.68	3.74
Hard	38.08	10.42	3.47	3.49	3.46
NMDYI	31.31	9.98	3.36	3.34	3.28
HM	24.85	8.85	2.97	2.92	2.95

The momentum independent potentials produce larger η cross section than the NMDYI potential which has been shown to be able to reproduce the η-meson cross section data well. Recall that NMDYI also gives much better baryon flow results.

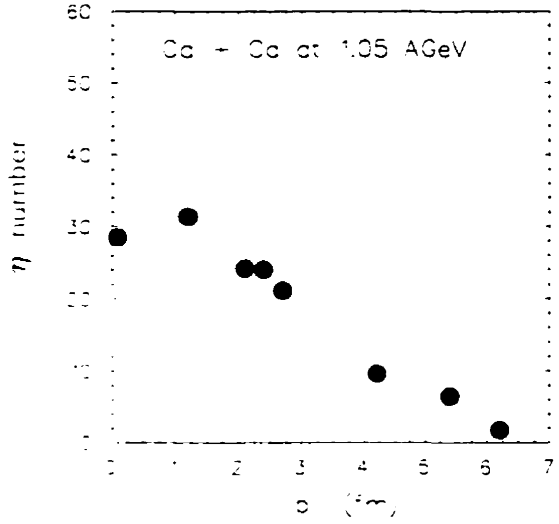

Figure 3.13: The impact parameter dependence of the η-meson yields for Ca + Ca collisions at 1.05 GeV/nucleon.

To get a better understanding of the collision dynamics, the dynamical evolution of the η, π and Δ from NMDYI potential are plotted in Fig. 3.14 for Ca + Ca at 1.05 GeV/nucleon, b=1.2 fm, together with the central density of the system. Note that the η-meson yields are completely generated in the compression stage. As both the η-meson and π are stabilized at freeze-out time, another useful comparison is the η/π^0 ratio. For Ar + Ca reaction at 1.0 GeV/nucleon, the TAPS measurement of $100^*\eta/\pi^0$ combined with a thermal model [109] gives the result 1.9 ± 1.2 with the full phase space. The BUU calculations for this ratio is 3.2 with NMDYI potential, which is slightly higher than the measurement [109]. Our calculations also display that this ratio is not very much sensitive to the impact parameter, which is a desired feature that the absolute η yields fail to have.

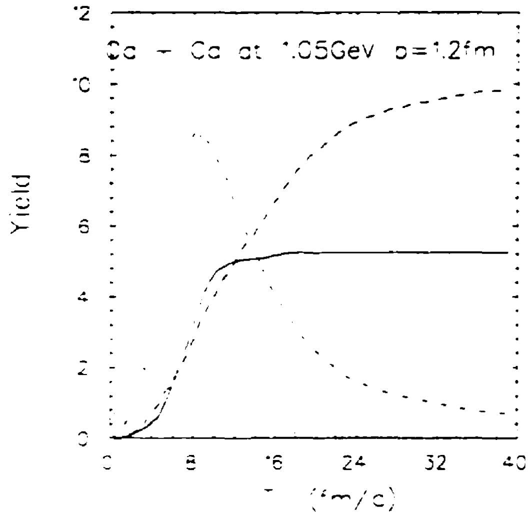

Figure 3.14: The dynamical evolution of various quantities in Ca + Ca collisions at 1.05 GeV/nucleon. b=1.2 fm. Dotted line: central density in units of ρ_0, dashed line: pions, solid line: η-mesons(50*η), dash-dotted line: Δ.

Now we are at the stage of comparing our calculation results with the DLS experimental data. The simulation results must be filtered by the DLS acceptance in order to directly compare to the measurements.

In Fig. 3.15, we compare the BUU calculation results to the new re-analyzed preliminary DLS data for Ca + Ca collision at 1.05 GeV/nucleon. The contributions from different sources are also displayed. The acceptance filter version we used is version 2.0 [2]. One can see that the BUU reproduces the spectrum in the mass region $0.2 \leq M \leq 0.5$ GeV reasonably well, and the dominant source for this region is the η Dalitz decay. As emphasized above, the contribution of the η-meson decay to the dielectron spectra only depends on the η-meson number and on the experimental acceptance, thus a measured η-meson number could be used to normalize the absolute dielectron cross section in this region. In the high mass region where the pion-pion annihilation is very important, the

---

[2] The experimental filter relevant to this experiment has not yet been released. However, it should be similar to the version 2.0, except at very low invariant masses [12].

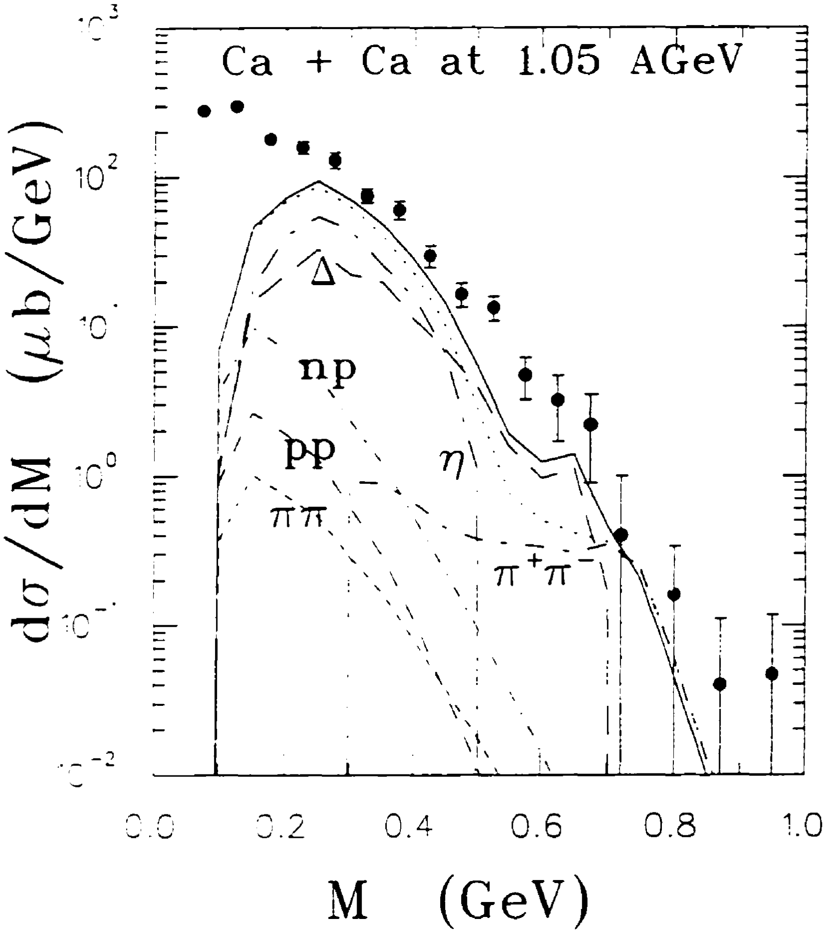

Figure 3.15: Dielectron invariant mass spectra for Ca + Ca collisions at 1.05 GeV/nucleon. The contributions from different sources are given by short-dashed-line: $\pi\pi$ bremsstrahlung; dashed-line: p-p bremsstrahlung; short-dashed-dotted-line: n-p bremsstrahlung; long-dashed-line: Δ decay; dashed-dotted-line: $\pi^+\pi^-$ annihilation; long-dashed-dotted-line: η decay; and the solid-line: sum of all the sources. The symbols are the preliminary experimental data from DLS [12]. The dotted-line is the sum of all the sources, where the VDM form factor is not included for delta Dalitz decay.

simulation results are within the experimental error bar. Note in this region, the statistics are quite low. The large difference in the very low mass region $M \approx 0.2$ GeV can be attributed to the fact that we neglected the very rich π^0 Dalitz decay and very importantly, the experimental filter in that region is different from the version 2.0 [12]. In the intermediate mass region, vector dominance improves the fit, but the calculation is still slightly under the data. A next generation calculation should explicitly include the π-N channel and also consider coherent effects with the delta Dalitz decay. From this figure, one can see that the bremsstrahlung contributions play a minor role. The $\pi\pi$ and proton-proton bremsstrahlung channels have much smaller contributions than the neutron-proton channel.

With respect to our results, there are still important issues. The intermediate dielectron invariant mass region reflects the in-medium Dalitz decay of the Δ and $\pi\pi$ annihilation. There are genuine in-medium processes. While the difference between the data and the calculation in this region may be an indicator of in-medium effects, such a conclusion can only be drawn after we have understood the dielectron sources in this region completely. An improved precision measurement of the η production total cross section or the η/π^0 ratio will be very useful. The simulations about particle multiplicity distributions and kinematics to determine the impact parameter range of the measured data from the DLS is also important, as our calculations display that the dielectron spectrum is somewhat dependent on the impact parameters. The next generation of calculation should also include the η absorption mechanism. In OBE model, this could proceed via N(1535) dynamics. This effect has to be explored cautiously. Its importance is presently somewhat of an open question [15, 111].

3.6 Summary

We have used the Boltzmann-Uehling-Uhlenbeck model to describe the dynamics of nucleus-nucleus collisions. Our BUU can reproduce the pion yields and the numerical calculation of dilepton production is carried out in a two-step process for all the sources. For nucleon-nucleon bremsstrahlung, we include the exact real photon electromagnetic current and the asymmetric parametrization for the n-p elastic differential cross section. Using these, we find smaller results than when using the small t approximation (Eq.(3.20)) and using the symmetric parametrization for the n-p differential cross section. The proton-proton and pion-pion bremsstrahlungs are unimportant at the energy of our calculations, but they are expected to play a more important role at higher energies. As the η cross section is small, we treat the η production perturbatively. Our results show that the η-meson decay dominates the dilepton spectra with the invariant mass from 0.2 to 0.5 GeV. A next generation calculation will use non-perturbative methods. In the mid-invariant mass region $0.5 < M < 0.7$ GeV, the delta Dalitz decay is the dominant source. The $\pi\pi$ annihilation determines the dielectron spectra shape at the high invariant mass. Further measurements of η production, and the determination of the impact parameter range for the Ca + Ca dielectron data at 1.05 GeV/nucleon will be very helpful. The facts that the HADES experiment is under the way at GSI and that the DLS is still improving their data analysis make this field promising.

Chapter 4

The Formalism For Bremsstrahlung: A Simple Test Case

4.1 Introduction

Testing theoretical models [26, 104, 105, 99, 119, 120, 123, 121] and approximations [21, 22, 23, 91, 122, 100, 124] has been a very important aspect of studying hadron-hadron bremsstrahlung processes, especially those processes containing significant resonance or exchange effects. In this chapter, with $\pi^+\pi^-$ bremsstrahlung as a case study, we consider the ρ, σ meson exchange interactions to evaluate the effects of various approximate formulae for bremsstrahlung.

The plan of this chapter is as follows. In the following two sections, we present the $\pi^-\pi^- \to \pi^-\pi^-$ elastic scattering amplitude and $\pi^+\pi^-$ bremsstrahlung amplitude using σ and ρ interactions. Then we will derive the general virtual-photon bremsstrahlung cross section in two-body scattering. In section **5** and **6**, we will discuss explicitly different soft-photon approximations. The formalism for exact virtual-photon amplitude calculations and the numerical results for different approximations are presented in section **7**. In section **8**, we discuss the anisotropy of virtual-photon emission. Then, we calculate the dilepton rates and yields. The dilepton yields are obtained by integrating the rates over the time or temperature evolution of the colliding nuclei within a Bjorken picture [126]. The results are presented in section **9**. The final section is a simple summary.

4.2 $\pi^+\pi^- \to \pi^+\pi^-$ Matrix Element

For charged pions interacting with a neutral ρ-meson, the Lagrangian is [123]

$$\mathcal{L} = \frac{1}{2}|D_\mu\Phi|^2 - \frac{1}{2}m_\pi^2|\Phi|^2 - \frac{1}{4}\rho_{\mu\nu}\rho^{\mu\nu} + \frac{1}{2}m_\rho^2\rho_\mu\rho^\mu \tag{4.1}$$

where Φ is the complex charged pion field, $\rho_{\mu\nu} = \partial_\mu\rho_\nu - \partial_\nu\rho_\mu$ is the ρ field strength and $D_\mu = \partial_\mu - ig_\rho\rho_\mu$ is the covariant derivative. Note that this Lagrangian is just like scalar electromagnetism but with a massive photon m_ρ. Then, the $\pi - \rho$ interaction will be

$$\mathcal{L}_{\pi\rho}^{int} = g_\rho(\Phi\rho^\mu\partial_\mu\Phi^* - \partial_\mu\Phi\rho^\mu\Phi^*) \tag{4.2}$$

For $\pi\sigma$ dynamics, we use [125]

$$\mathcal{L}_{\pi\sigma}^{int} = g_\sigma\sigma\partial_\mu\Phi \cdot \partial^\mu\Phi \tag{4.3}$$

Putting these two components together, we obtain the effective interaction Lagrangian

$$\mathcal{L}^{int} = g_\rho(\Phi\rho_\mu\partial_\mu\Phi^* - \partial_\mu\Phi\rho_\mu\Phi^*) + g_\sigma\sigma\partial_\mu\Phi \cdot \partial^\mu\Phi \tag{4.4}$$

With the Lagrangian Eq. (4.4) . we can get the amplitude $\mathcal{M}_0$ for the $\pi^+\pi^- \to \pi^+\pi^-$ $(p_1 + p_2 \to p_1' + p_2')$ elastic scattering. There are two terms $\mathcal{M}_1$ and $\mathcal{M}_2$ in the matrix element $\mathcal{M}_0$

$$\mathcal{M}_0 = \mathcal{M}_1 + \mathcal{M}_2. \tag{4.5}$$

For the s-channel, we include the imaginary part explicitly in the propagator,

$$\begin{aligned}\mathcal{M}_1 \quad &= \quad -\frac{g_\rho^2}{s - m_\rho^2 + im_\rho\Gamma_\rho}[(p_1 - p_2)^\mu g_{\mu\nu}(p_1' - p_2')^\nu] \\ &\quad + \frac{g_\sigma^2(p_1 \cdot p_2)(p_1' \cdot p_2')}{s - m_\sigma^2 + im_\sigma\Gamma_\sigma}\end{aligned} \tag{4.6}$$

We can rewrite Eq. (4.6) with Mandelstam variables

$$\mathcal{M}_1 = -\frac{g_\rho^2(u - t)}{s - m_\rho^2 + im_\rho\Gamma_\rho} + \frac{g_\sigma^2(s - 2m_\pi^2)^2}{s - m_\sigma^2 + im_\sigma\Gamma_\sigma} \tag{4.7}$$

For the t-channel. we include a monopole form factor [91]

$$h_\rho(t) = \frac{m_\rho^2 - m_\pi^2}{m_\rho^2 - t}, \qquad h_\sigma(t) = \frac{m_\sigma^2 - m_\pi^2}{m_\sigma^2 - t} \tag{4.8}$$

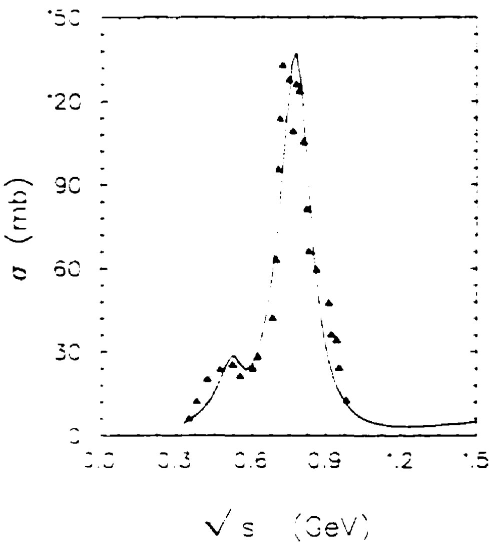

Figure 4.1: Total elastic $\pi^-\pi^-$ cross section as compared with experimental data from Refs. [127] and [128] . The symbols represent the data, whereas the solid line is for the model calculation results.

to suppress high momentum transfers, then

$$\begin{aligned}\mathcal{M}_2 &= -\frac{g_\rho^2 h_\rho^2(t)}{t-m_\rho^2}[-(p_2+p_2')^\mu g_{\mu\nu}(p_1+p_1')^\nu] \\ &\quad + \frac{g_\sigma^2 h_\sigma^2(t)}{t-m_\sigma^2}[(p_1\cdot p_1')(p_2\cdot p_2')]\end{aligned} \tag{4.9}$$

or with Mandelstam variables

$$\mathcal{M}_2 = \frac{g_\rho^2 h_\rho^2(t)(s-u)}{t-m_\rho^2} + \frac{g_\sigma^2 h_\sigma^2(t)(2m_\pi^2-t)^2}{t-m_\sigma^2} \tag{4.10}$$

The invariant energy is $s = (p_1+p_2)^2$, the four momentum transfer is $t = (p_2-p_2')^2$, and $u = 4m_\pi^2 - s - t$. The parameters have been adjusted to roughly fit the total $\pi^+\pi^-$ cross section up to $\sqrt{s} = 1.0$ GeV with $g_\rho = 6.25$, $m_\rho = 0.775$ GeV , Γ_ρ=0.155 GeV, $g_\sigma = 3.55, m_\sigma = 0.525$ GeV and $\Gamma_\sigma = 0.1$ GeV (see Fig. 4.1). The differential cross section distribution with such parameters is also plotted. This is shown in Fig. 4.2.

4.3 $\pi^+\pi^-$ Bremsstrahlung Amplitudes

For the reaction $(p_1 + p_2 \rightarrow p_1' + p_2' + q)$

$$\pi^+ + \pi^- \rightarrow \pi^+ + \pi^- + e^+e^- \tag{4.11}$$

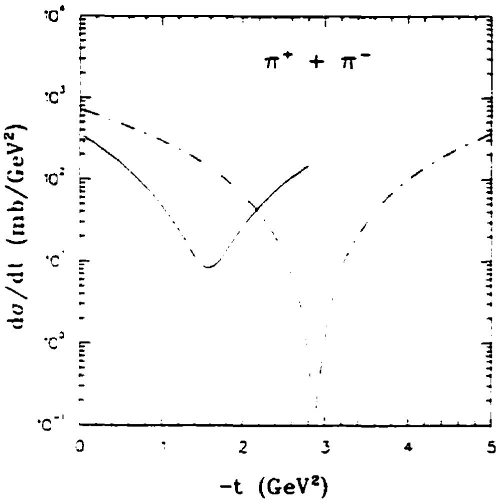

Figure 4.2: The $\pi^+\pi^-$ differential elastic cross section distributions at the system invariant energies 0.4 (dotted line), 0.6 (solid line), and 0.8 (dashed-dotted line) GeV, respectively.

only the Feynman diagrams where the virtual photon is attached to one of the external legs and the "seagull" terms contribute to the invariant matrix element $\mathcal{M}$ as shown in Fig.4.0. There are eight Feynman graphs to be added coherently from the external legs for each t-channel (Fig.4.0(a)) and each s-channel (Fig.4.0(b)). The total number of the "seagull" graphs represented by Fig.4.0(c) are also eight. In our case, we do not consider Feynman diagrams in which a virtual photon is radiated from internal lines as the propagator is neutral.

With the aid of the Feynman rules of pseudoscalar electrodynamics [129], we can write the radiation matrix element

$$\mathcal{M} = eK \cdot L \tag{4.12}$$

after summing up the contributions of all the individual Feynman graphs. There L_μ represents the lepton part

$$L_\mu = \frac{e}{M^2}\bar{u}(p_-, s_-)\gamma_\mu v(p_+, s_+) \tag{4.13}$$

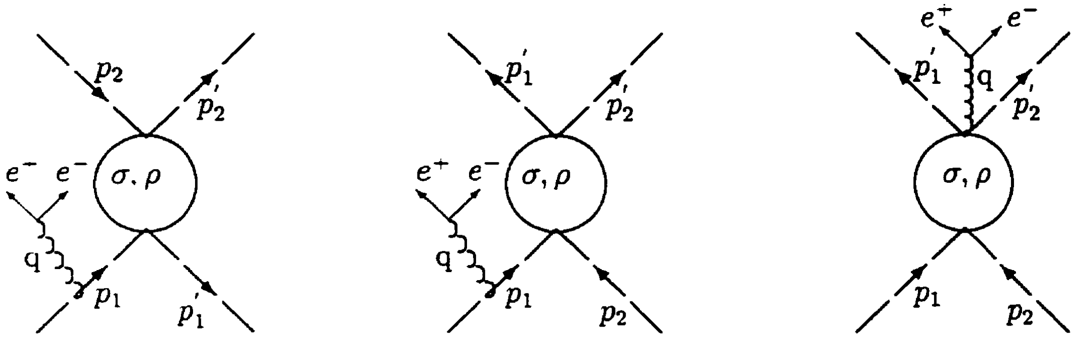

(a): t channel (b): s channel (c): Seagull graph

Fig.4.0: The lepton pairs emission from the $\pi^+\pi^- \to \pi^+\pi^-$ reactions

and the hadron-electric current includes two parts

$$K^\mu = K_1^\mu + K_2^\mu \tag{4.14}$$

where K_1^μ is the contribution from the external legs

$$\begin{aligned} K_1^\mu &= -Q_1 T_1 \frac{(2p_1 - q)^\mu}{2p_1 \cdot q - M^2} - Q_2 T_2 \frac{(2p_2 - q)^\mu}{2p_2 \cdot q - M^2} \\ &\quad + Q_1' T_1' \frac{(2p_1' + q)^\mu}{2p_1' \cdot q + M^2} + Q_2' T_2' \frac{(2p_2' + q)^\mu}{2p_2' \cdot q + M^2} \end{aligned} \tag{4.15}$$

with the definitions

$$\begin{aligned} T_1 &= \frac{g_\rho^2 h_\rho^2(k_2^2)}{k_2^2 - m_\rho^2}(p_1 + p_1' - q)(p_2 + p_2') \\ &\quad - \frac{g_\rho^2}{k_4^2 - m_\rho^2 + i m_\rho \Gamma_\rho}(p_1 - p_2 - q)(p_1' - p_2') \\ &\quad + \frac{g_\sigma^2 h_\sigma^2(k_2^2)}{k_2^2 - m_\sigma^2}(p_1 \cdot p_1' - p_1' \cdot q)(p_2 \cdot p_2') \\ &\quad + \frac{g_\sigma^2}{k_4^2 - m_\sigma^2 + i m_\sigma \Gamma_\sigma}(p_1 \cdot p_2 - p_2 \cdot q)(p_1' \cdot p_2') \\ T_2 &= \frac{g_\rho^2 h_\rho^2(k_1^2)}{k_1^2 - m_\rho^2}(p_1 + p_1')(p_2 + p_2' - q) \\ &\quad - \frac{g_\rho^2}{k_4^2 - m_\rho^2 + i m_\rho \Gamma_\rho}(p_1 - p_2 + q)(p_1' - p_2') \end{aligned}$$

$$
\begin{aligned}
&+\frac{g_\sigma^2 h_\sigma^2(k_1^2)}{k_1^2-m_\sigma^2}(p_1\cdot p_1^{'})(p_2\cdot p_2^{'}-p_2^{'}\cdot q) \\
&+\frac{g_\sigma^2}{k_4^2-m_\sigma^2+im_\sigma\Gamma_\sigma}(p_1\cdot p_2-p_1\cdot q)(p_1^{'}\cdot p_2^{'}) \\
T_1^{'} \quad = \quad &\frac{g_\rho^2 h_\rho^2(k_2^2)}{k_2^2-m_\rho^2}(p_1+p_1^{'}+q)(p_2+p_2^{'}) \\
&-\frac{g_\rho^2}{k_3^2-m_\rho^2+im_\rho\Gamma_\rho}(p_1^{'}-p_2^{'}+q)(p_1-p_2) \\
&+\frac{g_\sigma^2 h_\sigma^2(k_2^2)}{k_2^2-m_\sigma^2}(p_1\cdot p_1^{'}+p_1\cdot q)(p_2\cdot p_2^{'}) \\
&+\frac{g_\sigma^2}{k_3^2-m_\sigma^2+im_\sigma\Gamma_\sigma}(p_1\cdot p_2)(p_1^{'}\cdot p_2^{'}+p_2^{'}\cdot q) \\
T_2^{'} \quad = \quad &\frac{g_\rho^2 h_\rho^2(k_1^2)}{k_1^2-m_\rho^2}(p_1+p_1^{'})(p_2+p_2^{'}+q) \\
&-\frac{g_\rho^2}{k_3^2-m_\rho^2+im_\rho\Gamma_\rho}(p_1-p_2)(p_1^{'}-p_2^{'}-q) \\
&+\frac{g_\sigma^2 h_\sigma^2(k_1^2)}{k_1^2-m_\sigma^2}(p_1\cdot p_1^{'})(p_2\cdot p_2^{'}+p_2\cdot q) \\
&+\frac{g_\sigma^2}{k_3^2-m_\sigma^2+im_\sigma\Gamma_\sigma}(p_1\cdot p_2)(p_1^{'}\cdot p_2^{'}+p_1^{'}\cdot q).
\end{aligned}
\tag{4.16}
$$

The Q's represent the particle charges with $Q_1 = Q_1^{'}, Q_2 = Q_2^{'}$, and $q = p_+ + p_-$. The variables $k_i^{'}s$ are defined as $k_1 = p_1 - p_1^{'}$, $k_2 = p_2 - p_2^{'}$, $k_3 = p_1 + p_2$, $k_4 = p_1^{'} + p_2^{'}$.

The contribution from the seagull diagrams can be written as

$$
\begin{aligned}
K_2^\mu \quad = \quad &-Q_1\frac{2g_\rho^2 h_\rho^2(k_2^2)}{k_2^2-m_\rho^2}(p_2^{'}+p_2)^\mu - Q_2\frac{2g_\rho^2}{k_4^2-m_\rho^2+im_\rho\Gamma_\rho}(p_1^{'}-p_2^{'})^\mu \\
&-Q_1^{'}\frac{2g_\rho^2}{k_3^2-m_\rho^2+im_\rho\Gamma_\rho}(p_2-p_1)^\mu - Q_2^{'}\frac{2g_\rho^2 h_\rho^2(k_1^2)}{k_1^2-m_\rho^2}(p_1+p_1^{'})^\mu \\
&-Q_1\frac{g_\sigma^2 h_\sigma^2(k_2^2)}{k_2^2-m_\sigma^2}[(p_1+p_1^{'})\cdot q](p_2\cdot p_2^{'}) \\
&-Q_2\frac{g_\sigma^2}{k_4^2-m_\sigma^2+im_\sigma\Gamma_\sigma}[(p_1-p_2)\cdot q](p_1^{'}\cdot p_2^{'}) \\
&-Q_1^{'}\frac{g_\sigma^2}{k_3^2-m_\sigma^2+im_\sigma\Gamma_\sigma}[(p_2^{'}-p_1^{'})\cdot q](p_1\cdot p_2) \\
&-Q_2^{'}\frac{g_\sigma^2 h_\sigma^2(k_1^2)}{k_1^2-m_\sigma^2}[(p_2+p_2^{'})\cdot q](p_1\cdot p_1^{'})
\end{aligned}
\tag{4.17}
$$

For now, by squaring the invariant amplitude $\mathcal{M}$, and summing over the spin of the lepton pairs. we obtain

$$\sum_{s_+s_-} |\mathcal{M}|^2 = 4\pi\alpha K^\mu K^\nu L_{\mu\nu} \tag{4.18}$$

After summation over the e^+e^- spins, the lepton tensor is equal to

$$L_{\mu\nu} = \sum_{s_+s_-} L_\mu L_\nu = \frac{8\pi\alpha}{M^4}(q_\mu q_\nu - l_\mu l_\nu - M^2 g_{\mu\nu}) \tag{4.19}$$

where $l_\mu = p_+ - p_-$ is the relative dilepton momentum. Then, the invariant amplitude can be expressed as

$$\sum_{s_+s_-} |\mathcal{M}|^2 = \frac{32\pi^2\alpha^2}{M^4}[(q\cdot K)^2 - (l\cdot K)^2 - M^2K^2] \tag{4.20}$$

4.4 Derivation of the cross section

We can directly write the differential cross section for e^+e^- pair production

$$\begin{aligned} E_+E_-\frac{d^6\sigma^{e^+e^-}}{d^3p_+d^3p_-} &= \frac{1}{16E_1E_2|\mathbf{v}_1 - \mathbf{v}_2|}\frac{1}{(2\pi)^6}\sum_{s_+s_-}|\mathcal{M}|^2 \\ &\times(2\pi)^4\delta^4\left(p_1 + p_2 - p_1' - p_2' - q\right)\frac{d^3p_1'}{(2\pi)^3 2E_1'}\frac{d^3p_2'}{(2\pi)^3 2E_2'} \end{aligned} \tag{4.21}$$

Recall the general formula from relativistic kinematics

$$q_0\frac{d^6\sigma^{e^+e^-}}{dM^2d^3q\,d\Omega_+} = \frac{1}{4}\sqrt{1 - \frac{4\mu^2}{M^2}}E_+E_-\frac{d^6\sigma^{e^+e^-}}{d^3p_+d^3p_-} \tag{4.22}$$

where μ is the electron mass, $q_0 = E_+ + E_-$, and $d\Omega_+$ is the solid angle for positron momentum in the dilepton rest frame. Note in that frame, the integral

$$\int\frac{(l\cdot K)^2}{M^2}d\Omega_+ = \frac{4\pi}{3}(1 - \frac{4\mu^2}{M^2})[\frac{(q\cdot K)^2}{M^2} - K^2] \tag{4.23}$$

We finally obtain the differential cross section for lepton pair radiation with invariant mass M and energy q_0 as

$$\begin{aligned} q_0\frac{d^4\sigma^{e^+e^-}}{dM^2d^3q} &= \frac{1}{4E_1E_2|\mathbf{v}_1 - \mathbf{v}_2|}\frac{\alpha^2}{12\pi^3}\frac{1}{M^2}(1 + \frac{2\mu^2}{M^2})\sqrt{1 - \frac{4\mu^2}{M^2}} \\ &\times\int[\frac{(q\cdot K)^2}{M^2} - K^2](2\pi)^4\delta^4\left(p_1 + p_2 - p_1' - p_2' - q\right) \\ &\times\frac{d^3p_1'}{(2\pi)^3 2E_1'}\frac{d^3p_2'}{(2\pi)^3 2E_2'} \end{aligned} \tag{4.24}$$

4.5 Soft-photon Approximation(SPA)

If we suppose that the non-radiative matrix element will not change when a virtual photon is radiated from the incoming or outgoing charged particles, it means that the dilepton momentum q in Eq. (4.16) can be neglected (approximation I), then we get

$$T_1 = T_2 = T_1' = T_2' = \mathcal{M}_0 \tag{4.25}$$

This approximation, in fact, neglects all the contributions from the Feynman diagrams in which a virtual photon radiates from the internal lines and contact terms, and is the basis of most soft photon approximations. Approximation I is also known as the on-shell approach. The hadron-electric current K_1^μ in this case can be written as

$$K_1^\mu = \mathcal{M}_0 J^\mu \tag{4.26}$$

with the four-vector electric current

$$\begin{aligned} J^\mu &= -Q_1\frac{(2p_1-q)^\mu}{2p_1\cdot q - M^2} - Q_2\frac{(2p_2-q)^\mu}{2p_2\cdot q - M^2} \\ &\quad + Q_1'\frac{(2p_1'+q)^\mu}{2p_1'\cdot q + M^2} + Q_2'\frac{(2p_2'+q)^\mu}{2p_2'\cdot q + M^2} \end{aligned} \tag{4.27}$$

Taking charge conservation ($J\cdot q = 0$) into account, we can immediately rewrite the differential cross section from Eq. (4.24) as

$$\begin{aligned} q_0\frac{d^4\sigma^{e^+e^-}}{dM^2d^3q} &= \frac{1}{4E_1E_2|\mathbf{v}_1-\mathbf{v}_2|}\frac{\alpha^2}{48\pi^5}\frac{1}{M^2}\left(1+\frac{2\mu^2}{M^2}\right)\sqrt{1-\frac{4\mu^2}{M^2}} \\ &\quad \times\int(-J^2)|\mathcal{M}_0|^2\delta^4\left(p_1+p_2-p_1'-p_2'-q\right)\frac{d^3p_1'}{2E_1'}\frac{d^3p_2'}{2E_2'} \end{aligned} \tag{4.28}$$

4.5.1 Rückl Approach

Now we further neglect the lepton pair four-momentum q in the argument of the four-dimensional δ function in Eq. (4.28) (approximation II). Because of this approximation, the energy-momentum conservation will be violated. To restore the energy conservation, we will include a two-body Lorentz invariant phase space ratio factor $\frac{R_2(s_2,m_1^2,m_2^2)}{R_2(s,m_1^2,m_2^2)}$, where s is the invariant energy available for all the final state particles and $s_2 = s + M^2 - 2q_0\sqrt{s}$ in the center of mass of $p_1 + p_2$ frame. This ratio factor originates from

$$\int \delta^4(p_1 + p_2 - p_1^{'} - p_2^{'} - q)\frac{d^3p_1^{'}}{2E_1^{'}}\frac{d^3p_2^{'}}{2E_2^{'}} = \int \frac{R_2(s_2, m_1^2, m_2^2)}{R_2(s, m_1^2, m_2^2)} \times \delta^4(p_1 + p_2 - p_1^{'} - p_2^{'})\frac{d^3p_1^{'}}{2E_1^{'}}\frac{d^3p_2^{'}}{2E_2^{'}}\,, \tag{4.29}$$

and will reduce the dilepton production accordingly with the increase of e^+e^- pair invariant mass M as mentioned in Chapter **3**. Recall that the two-body elastic differential cross section

$$d\sigma^{12\to 1'2'} = \frac{1}{4E_1E_2|\mathbf{v}_1 - \mathbf{v}_2|}|\mathcal{M}_0|^2(2\pi)^4\delta^4(p_1 + p_2 - p_1^{'} - p_2^{'})\frac{d^3p_1^{'}}{2E_1^{'}(2\pi)^3}\frac{d^3p_2^{'}}{2E_2^{'}(2\pi)^3} \tag{4.30}$$

The Lorentz-covariant differential cross section from Eq. (4.28) then reads

$$q_0\frac{d^4\sigma^{e^+e^-}}{dM^2d^3q} = \frac{\alpha^2}{12\pi^3}\frac{1}{M^2}(1 + \frac{2\mu^2}{M^2})\sqrt{1 - \frac{4\mu^2}{M^2}}\int(-J^2)\frac{d\sigma^{12\to 1'2'}}{dt}\frac{R_2(s_2, m_1^2, m_2^2)}{R_2(s, m_1^2, m_2^2)}dt \tag{4.31}$$

We note that if the electron mass is set μ=0, the formula Eq. (4.31) is the same as the expression used by Haglin, Gale, and Emel'yanov [91], except for a numerical factor $\frac{2}{3}$ originally omitted from Rückl's formula [22]. However, the electric current J^μ in this approach is exact for the case of interest, whereas in theirs the current for real photon emission

$$J^\mu = -Q_1\frac{p_1^\mu}{p_1 \cdot q} - Q_2\frac{p_2^\mu}{p_2 \cdot q} + Q_1^{'}\frac{p_1^{'\mu}}{p_1^{'} \cdot q} + Q_2^{'}\frac{p_2^{'\mu}}{p_2^{'} \cdot q} \tag{4.32}$$

was used for soft virtual photons. In general, the current J^μ Eq. (4.27) contains at least the subleading order in q , whereas the current of Eq. (4.32) is in the leading order. A quantitative comparison will pin down the effect of different levels of approximation.

After integrating over the 3-momentum space of the e^+e^- pair from Eq. (4.31), we can finally express the differential cross section as

$$\frac{d\sigma^{e^+e^-}}{dM^2} = \frac{\alpha^2}{3\pi^2}\frac{1}{M^2}(1 + \frac{2\mu^2}{M^2})\sqrt{1 - \frac{4\mu^2}{M^2}} \int\sqrt{q_0^2 - M^2}\sqrt{\frac{s(s_2 - 4m_\pi^2)}{s_2(s - 4m_\pi^2)}}(-J^2)\frac{d\sigma^{12\to 1'2'}}{dt}dtdq_0 \tag{4.33}$$

The two-body phase space ratio factor has been put as

$$\frac{R_2(s_2, m_1^2, m_2^2)}{R_2(s, m_1^2, m_2^2)} = \sqrt{\frac{s(s_2 - 4m_\pi^2)}{s_2(s - 4m_\pi)}}. \tag{4.34}$$

In principle, the elastic differential cross section $d\sigma^{12\to 1'2'}/dt$ can be parametrized from measured experimental data. Here we rely on the model calculation to make use of the on-shell matrix element $\mathcal{M}_0$ in Eq. (4.5) for consistency. The result is

$$\frac{d\sigma^{12\to 1'2'}}{dt} = \frac{|\mathcal{M}_0|^2}{16\pi s(s - 4m_\pi^2)} \tag{4.35}$$

In Fig. 4.3, we plot the dilepton differential cross section $d\sigma^{e^+e^-}/dM$ as a function of e^-e^- pair invariant mass M with the virtual photon current Eq. (4.27) and the exact real photon current Eq. (4.32). Since the solid and dotted curves are obtained under the same approximations, this comparison clearly shows the effect of using virtual photon current and real photon current. Our results do not substantiate a recent general argument [21] that the virtual photon current may make significant differences in dilepton production. From here on, we use the virtual current Eq. (4.27).

Summarizing, we have presented the SPA approach along the lines introduced by Rückl. We shall refer the above approximation as "Rückl's approach".

4.5.2 The Complete Phase-space Approach

Because of approximation II inherent to SPA, one can not calculate the current term $(-J^2)$ precisely. To calculate the kinematics exactly $(p_1 + p_2 = p_1' + p_2' + q)$, we need to keep the argument q in Dirac δ function as in Eq. (4.28). Write one of the final state particle integral $d^3p_1'/2E_1'$ in the explicitly invariant form

$$\frac{d^3p_1'}{2E_1'} = \int d^4p_1' \delta(p_1'^2 - m_\pi^2)\theta(p^0) \tag{4.36}$$

where $\theta(p^0)$ is the step function, and note that in the center of mass 1+2 frame

$$p_1'^2 = m_\pi^2 + s + M^2 + 2E_2' q_0 - 2|\vec{p}_2'||\vec{q}| \cos\theta_{p_2'q} - 2\sqrt{s}(E_2' + q_0), \tag{4.37}$$

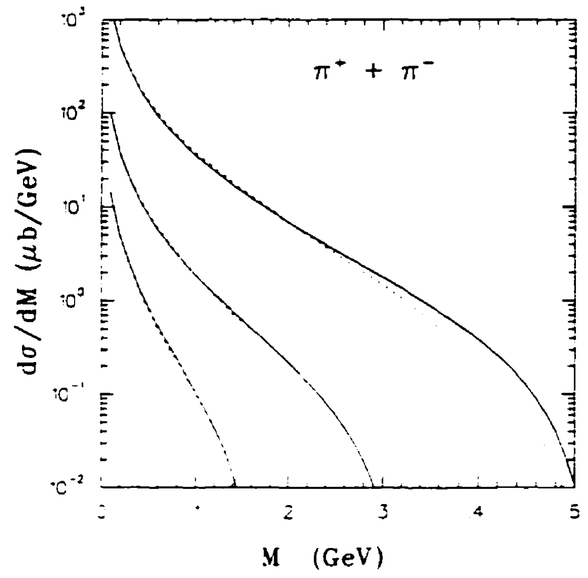

Figure 4.3: The Lorentz covariant global dilepton differential cross section against the lepton pair invariant mass M for $\pi^+\pi^-$ collisions. The solid lines are for real current approximations, the dotted lines are for virtual current approaches at system invariant energies 0.45, 0.6 and 0.8 GeV, respectively.

the final state integrals can be rewritten as

$$\int \delta^4\left(p_1+p_2-p_1'-p_2'-q\right)\frac{d^3p_1'}{2E_1'}\frac{d^3p_2'}{2E_2'} = \frac{1}{4}\int\frac{1}{|\vec{q}|}dE_2'd\cos\theta_{p_2'q}d\phi \times\delta\left(\cos\theta_{p_2'q}-\frac{s+M^2+2E_2'q_0-2\sqrt{s}(E_2'+q_0)}{2|\vec{p_2'}||\vec{q}|}\right) \qquad (4.38)$$

Using the fact that $d^3q/q_0 = |\vec{q}|dq_0 d\cos\theta_{p_1q}d\phi'$, and further integrating over the free variable ϕ', we obtain

$$\frac{d\sigma^{e^+e^-}}{dM^2} = \frac{\alpha^2}{12\pi^3}\frac{1}{M^2}(1+\frac{2\mu^2}{M^2})\sqrt{1-\frac{4\mu^2}{M^2}}\sqrt{s(s-4m_\pi^2)}\int(-J^2)\frac{d\sigma^{12\to1'2'}}{dt} \times\delta\left(\cos\theta_{p_2'q}-\frac{s+M^2+2E_2'q_0-2\sqrt{s}(E_2'+q_0)}{2|\vec{p_2'}||\vec{q}|}\right) \times dq_0dE_2'd\cos\theta_{p_1q}d\cos\theta_{p_2'q}d\phi \qquad (4.39)$$

The integral range of the variables dq_0 and dE_2' can be determined from the δ function condition

$$|\cos\theta_{p_2'q}| = |\frac{s+M^2+2E_2'q_0-2\sqrt{s}(E_2'+q_0)}{2|\vec{p_2'}||\vec{q}|}| \leq 1 \qquad (4.40)$$

Up to this stage, we have used the invariant matrix $\mathcal{M}_0$(Eq. (4.5)) expressed by the invariant variables s and t: $K^\mu(s,t)$ (Eq. (4.7)), or by u and t: $K^\mu(u,t)$ (Eq. (4.10)) [1], to calculate the dilepton production differential cross section as a function of the e^+e^- pair invariant mass M under the complete phase-space approach. In this method, the current term J^μ is evaluated exactly (refer to Appendix C) and the effective four-momentum transfer t is determined strictly by the kinematics $p_1 + p_2 = p_1' + p_2' + q$.

4.6 Sub-leading order approximation

In this section, we will only consider the $K^\mu(s,t)$ scheme for the leading order amplitude. To the subleading order, we can expand

$$\begin{aligned} \mathcal{M}_0(p_i - q) &= \mathcal{M}_0 - q^\alpha \frac{\partial \mathcal{M}_0}{\partial p_i^\alpha} \\ \mathcal{M}_0(p_i' + q) &= \mathcal{M}_0 + q^\alpha \frac{\partial \mathcal{M}_0}{\partial p_i'^\alpha} \end{aligned} \tag{4.41}$$

However, this procedure breaks gauge invariance. To restore gauge invariance, we should include the seagull graphs contribution up to the same order as mentioned previously. The seagull terms to this order can be written as

$$\mathcal{M}_0' = -e \sum_i Q_i \frac{\partial \mathcal{M}_0}{\partial p_{i\mu}} \tag{4.42}$$

Thus, the hadron-electric current reads

$$K^\mu = \mathcal{M}_0 J^\mu + \sum_i Q_i \frac{\partial \mathcal{M}_0}{\partial p_i^\alpha} \left(\frac{p_i^\mu q^\alpha}{p_i \cdot q} - g^{\mu\alpha} \right) \tag{4.43}$$

Now, substituting K^μ into Eq. (4.24) and using the same procedure as in the leading order approximation, we get the differential cross section in dilepton invariant mass M up to the subleading order

$$\frac{d\sigma^{e^-e^-}}{dM^2} = \frac{\alpha^2}{12 \times 16\pi^4} \frac{1}{M^2} \left(1 + \frac{2\mu^2}{M^2}\right) \sqrt{1 - \frac{4\mu^2}{M^2}} \frac{1}{\sqrt{s(s - 4m_\pi^2)}}$$

---

[1] We refer them as $K^\mu(s,t)$ scheme and $K^\mu(u,t)$ scheme. Note that the difference between these schemes is relevant only in the case of approximation I.

$$
\begin{aligned}
&\times \int \left((-J^2)|\mathcal{M}_0|^2 + \sum_{i=1}^{4}\sum_{j=1}^{4} \frac{Q_i Q_j'}{(p_i \cdot q)(p_j \cdot q)} [(p_i \cdot q)p_j^\beta - (p_i \cdot p_j)q^\beta] \frac{\partial |\mathcal{M}_0|^2}{\partial p_i^\beta} \right) \\
&\times \delta \left(\cos\theta_{p_2' q} - \frac{s + M^2 + 2E_2' q_0 - 2\sqrt{s}(E_2' + q_0)}{2|\vec{p_2'}||\vec{q}|} \right) \\
&\times dq_0 dE_2' d\cos\theta_{p_1 q} d\cos\theta_{p_2' q} d\phi
\end{aligned} \tag{4.44}
$$

Note for simplicity, we have used the convention $Q_j' = -Q_j$ for the incoming hadrons, $Q_j' = Q_j$ for the outcoming hadrons, and $p_1' = p_3, p_2' = p_4$ in Eq. (4.44).

To express the subleading term in term of scalar products $p_i \cdot p_j$, we write

$$
\frac{\partial |\mathcal{M}_0|^2}{\partial p_i} = \frac{\partial |\mathcal{M}_0|^2}{\partial s}\frac{\partial s}{\partial p_i} + \frac{\partial |\mathcal{M}_0|^2}{\partial t}\frac{\partial t}{\partial p_i}. \tag{4.45}
$$

Since we expand the $\mathcal{M}_0$ in powers of the dilepton energy q, and only keep the first derivative, the above subleading formula will be effective only for the case that the maximum energy of the dilepton is much less than the energies of the particles in the system.

4.7 Exact Results

For an exact calculation, we make use of the hadron-electric current K^μ in Eq. (4.15). Since gauge invariance is an important issue here, a gauge-invariance check leads to

$$
q_\mu K_1^\mu = -Q_1 T_1 - Q_2 T_2 + Q_1' T_1' + Q_2' T_2' = -q_\mu K_2^\mu \tag{4.46}
$$

It shows that $q_\mu K^\mu = 0$, the sum of the amplitudes K^μ presented in Eq. (4.15) is gauge invariant. Then we have

$$
\begin{aligned}
\frac{d\sigma^{e^- e^-}}{dM^2} &= \frac{\alpha^2}{12 \times 16\pi^4} \frac{1}{M^2}\left(1 + \frac{2\mu^2}{M^2}\right)\sqrt{1 - \frac{4\mu^2}{M^2}} \frac{1}{\sqrt{s(s - 4m_\pi^2)}} \\
&\times \int [-(K_1^2 + 2K_1 \cdot K_2 + K_2^2)] dq_0 dE_2' d\cos\theta_{p_1 q} d\cos\theta_{p_2' q} d\phi \\
&\times \delta \left(\cos\theta_{p_2' q} - \frac{s + M^2 + 2E_2' q_0 - 2\sqrt{s}(E_2' + q_0)}{2|\vec{p_2'}||\vec{q}|} \right)
\end{aligned} \tag{4.47}
$$

The square of the invariant matrix element K^2 just involves the combinations of the ten scalar products and known relative constants (see Appendix C).

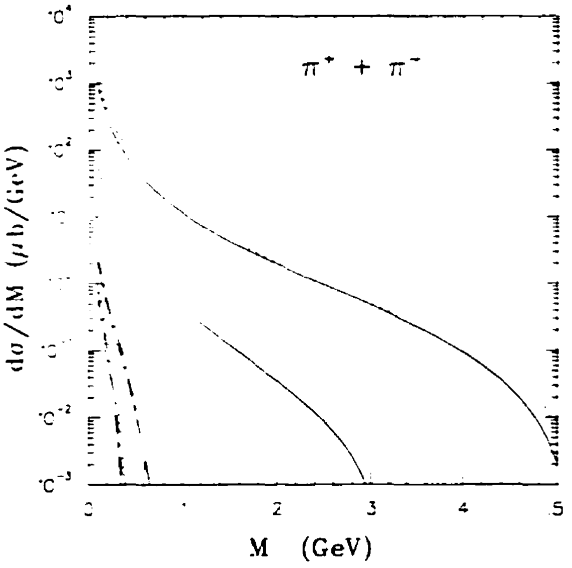

Figure 4.4: The comparison between the exact dilepton differential cross section calculation and the leading-order approximations (often used Low-scheme: $K^\mu(s,t)$) for $\pi^+\pi^-$ collisions at the system invariant energies 0.32, 0.36, 0.6 and 0.8 GeV. At the two smallest energies 0.32 and 0.36 GeV, the subleading-order contributions are also presented. The solid lines are the exact calculations (Eq. (4.47)), the dotted lines are the $K^\mu(s,t)$ scheme leading-order results. While the dashed-dotted lines represent the calculation results up to the subleading-order with the $K^\mu(s,t)$ scheme.

The results for the calculation of the dilepton differential cross section with Eq. (4.15) are presented in Fig. 4.4. and compared with the results of the $K^\mu(s,t)$ scheme for $\sqrt{s}$=0.32. 0.36. 0.60 and 0.80 GeV, respectively. At $\sqrt{s}$=0.32 and 0.36 GeV, we also plot the SPA $K^\mu(s,t)$ results up to the subleading-order. It shows that the traditional SPA $K^\mu(s,t)$ approach overestimates the exact results. This overestimation may suggest the size of off-shell contributions to the dilepton production cross section. At $\sqrt{s}$=0.6 and 0.8 GeV, we do not include the subleading-order contributions, since at large energies our expansion technique will cease to be valid. The results up to the subleading-order match the exact results with a reasonable accuracy in energies where they have been calculated. In the low energy limit, when $\sqrt{s}$ of a system is not too large, our results suggest that the soft-photon approximation formula are appropriate.

In Fig. 4.5. we present the comparison the different soft-photon approaches and the exact calculation for energies $\sqrt{s}$=0.32. 0.4 and 0.6 GeV. From this figure, (i) the effect of

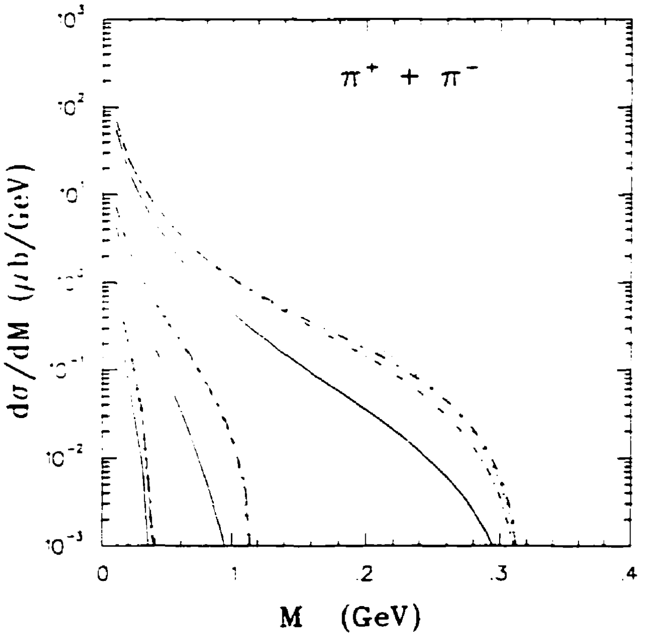

Figure 4.5: The comparison between the exact dilepton differential cross sections in $\pi^+\pi^-$ collisions and the three-different soft-photon approaches (see the text), for invariant energies of 0.32, 0.40 and 0.60 GeV, respectively. The solid lines represent the exact calculation: the dashed-dotted lines and the long-dashed-dotted lines are for $K^\mu(s,t)$ and $K^\mu(u,t)$ schemes, respectively. Finally, the dotted lines represent the Rückl approach (see the text) with virtual current.

the SPA approximation II can be appreciated by comparing the "Rückl approach" results and those with the $K^\mu(s,t)$, as the "Rückl approach" uses both approximation I and II, and the complete phase-space approach only uses approximation I. Although the virtual current is used for both cases, there are differences between the two approaches. (ii) we can see the effects of using $K^\mu(s,t)$ scheme and the corresponding $K^\mu(u,t)$ scheme. There are some differences between these two approaches to the soft-photon approximation. (iii) At low energies, *e.g.* $\sqrt{s} = 0.32$ GeV, all the SPA approaches can give reasonable dilepton cross section, comparing to the exact results.

4.8 Anisotropy of Dilepton Emission

From Eq. (4.20), Eq. (4.21) and Eq. (4.22), we obtain

$$
\begin{aligned}
q_0 \frac{d^6\sigma^{e^+e^-}}{dM^2 d^3q d\Omega_-} &= \frac{1}{4E_1E_2|\mathbf{v}_1 - \mathbf{v}_2|} \frac{\alpha^2}{32\pi^4} \frac{1}{M^2} \sqrt{1 - \frac{4\mu^2}{M^2}} \int [-\frac{(l \cdot K)^2}{M^2} - K^2] \\
&\times (2\pi)^4 \delta^4 \left(p_1 + p_2 - p_1^{'} - p_2^{'} - q\right) \frac{d^3p_1^{'}}{(2\pi)^3 2E_1^{'}} \frac{d^3p_2^{'}}{(2\pi)^3 2E_2^{'}} \qquad (4.48)
\end{aligned}
$$

Write $d\Omega^+ = d\cos\theta d\phi$, and integrating over d^3q and $d\phi$, Eq. (4.48) can be simplified as

$$
\begin{aligned}
\frac{d^2\sigma^{e^+e^-}}{dM^2 d\cos\theta} &= \frac{\alpha^2}{16^2\pi^4} \sqrt{1 - \frac{4\mu^2}{M^2}} \frac{1}{\sqrt{s(s - 4m_\pi^2)}} \frac{1}{M^2} \frac{1}{2\pi} \int [-\frac{(l \cdot K)^2}{M^2} - K^2] \\
&\times \delta \left(\cos\theta_{p_2^{'}q} - \frac{s + M^2 + 2E_2^{'}q_0 - 2\sqrt{s}(E_2^{'} + q_0)}{2|\vec{p_2^{'}}||\vec{q}|} \right) \\
&\times dq_0 dE_2^{'} d\cos\theta_{p_1q} d\cos\theta_{p_2^{'}q} d\phi d\phi_1 \qquad (4.49)
\end{aligned}
$$

In the rest frame of the lepton pair, the gauge invariance condition $q^\mu K_\mu = 0$ leads to

$$(l \cdot K)^2 = 2(p_+ \cdot K)^2 + 2(p_- \cdot K)^2 \qquad (4.50)$$

Define an unit vector $\hat{p}_+$ in the dilepton rest frame("$i^{'}j^{'}k^{'}$" frame, refer to Fig. (4.6))

$$\hat{p}_+ = \cos\theta \hat{k}^{'} + \sin\theta \sin\phi \hat{j}^{'} + \sin\theta\cos\phi \hat{i}^{'} \qquad (4.51)$$

where θ is the angle between the unit vectors $\hat{q}$ and $\hat{p}_+$.

Now in the center of mass $\vec{p_1} + \vec{p_2}$ frame of the two colliding pions, we choose the coordinate system("ijk" frame) such that

$$
\begin{aligned}
&\hat{q} = \hat{k}, \\
&\hat{p}_1 = \cos\theta_{p_1q}\hat{k} + \sin\theta_{p_1q}\hat{j} = -\hat{p}_2, \\
&\hat{p}_2^{'} = \cos\theta_{p_2^{'}q}\hat{k} + \sin\theta_{p_2^{'}q}\sin\phi_1\hat{j} + \sin\theta_{p_2^{'}q}\cos\phi_1\hat{i} \\
&\hat{p}_1^{'} = -(\hat{p}_2^{'} + \hat{q}) \qquad (4.52)
\end{aligned}
$$

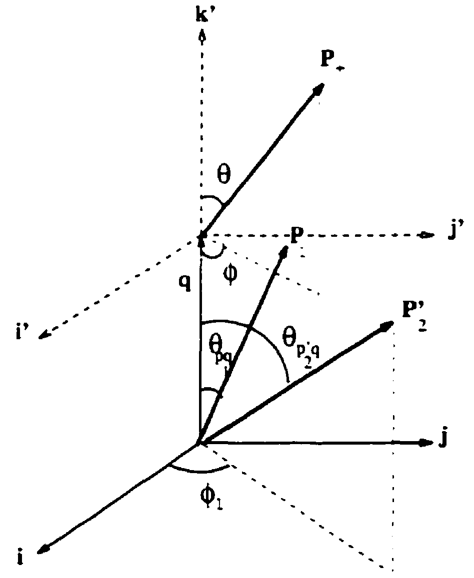

Figure 4.6: The coordinate relation of the dilepton rest frame (i'j'k') and the center of mass two colliding pions frame (ijk). $\vec{p_+}$ is the positron momentum in i'j'k' frame, $\vec{p_1}$ is the initial pion momentum, $\vec{p_2'}$ is one of the final pion momentum in the ijk frame.

Then the "$i'j'k'$" frame is coincident with the "ijk" frame (see Fig. (4.6)).

As all the variables should obviously be evaluated in the same frame, here we choose in the $p_1 - p_2$ centre of mass frame. Note that the vector $\vec{p}_+$ up to now is in the dilepton rest frame, we need to perform Lorentz transformation, which is between two frames of reference moving with the momentum $\vec{q}$ along the $\hat{k}$ direction.

In the dilepton rest frame, the dilepton has energy M, and $E_+ = E_-$ =M/2, $|\vec{p_+}| = |\vec{p_-} = \sqrt{\frac{M^2}{4} - \mu^2}$. In the c.m. of $p_1 + p_2$ frame,$|\vec{p_1}| = \vec{p_2}| = p = \sqrt{\frac{s}{4} - m_\pi^2}, E_1 = E_2 = E = \frac{\sqrt{s}}{2}$,and the dilepton has energy q_0, then

$$\gamma = \frac{q_0}{M}, \qquad \beta = \frac{\sqrt{\gamma^2 - 1}}{\gamma} \tag{4.53}$$

After performing the Lorentz transformation, we have in the pion-pion c.m. frame($\vec{p_1} + \vec{p_2} = 0$)

$$\begin{aligned} \vec{p_+} &= \frac{M}{2}[(\gamma\beta + \gamma\cos\theta)\hat{k} + \sin\theta\sin\phi\hat{j} + \sin\theta\cos\phi\hat{i}] \\ E_+ &= \frac{M}{2}(1 + \beta\cos\theta) \end{aligned}$$

$$
\begin{aligned}
\vec{p_-} &= \frac{M}{2}[(\gamma\beta - \gamma\cos\theta)\hat{k} - \sin\theta\sin\phi\hat{j} - \sin\theta\cos\phi\hat{i}] \\
E_- &= \frac{M}{2}(1 - \beta\cos\theta) \qquad (4.54)
\end{aligned}
$$

The electron mass has been set $\mu = 0$. Therefore, all the scalar products $(p_i \cdot p_j)$, $(p_i \cdot p_+)$, and $(p_i \cdot p_-)$ implied by Eq. (4.50) can be expressed in term of the integrating variables of Eq. (4.49). Write

$$S = \frac{d^2\sigma^{e^+e^-}}{dM^2 d\cos\theta}. \qquad (4.55)$$

We are finally able to calculate the anisotropy parameter B, which is defined as

$$B = \frac{S(M, \theta = 0)}{S(M, \theta = 90^o)} - 1 \qquad (4.56)$$

Fig. 4.7 presents the so-called anisotropy parameter B against the invariant mass M of the lepton pairs at the system effective energy $\sqrt{s}$=0.35, 0.6 and 0.8 GeV, respectively. The solid lines represent our exact result while the dotted lines are for SPA $K^\mu(s,t)$ results. At $\sqrt{s}$=0.35 GeV, we also show the SPA results up to subleading-order. The contribution of the subleading-order slightly reduce the parameter B from the SPA leading order. At small invariant mass M of the lepton pairs, the exact results are very different from those in the SPA approach. Once the effective energy becomes high, the anisotropy coefficient B stays at around zero for large M of dileptons.

4.9 Dilepton Rates and Yields

We now seek a simple framework for the application of the method developed up to now. Since we know that ultrarelativistic heavy ion collisions are meson-dominated, we concentrate on that area. Bear in mind that the following calculations are done for comparison purposes mostly and we do not attempt to model any data. Rather, we have looked for a somewhat idealized and simple environment.

In ultrarelativistic nuclear collisions, the dilepton emission may serve as a very important probe for the QCD phase transition [2]. The low invariant mass(M < 0.5 GeV)

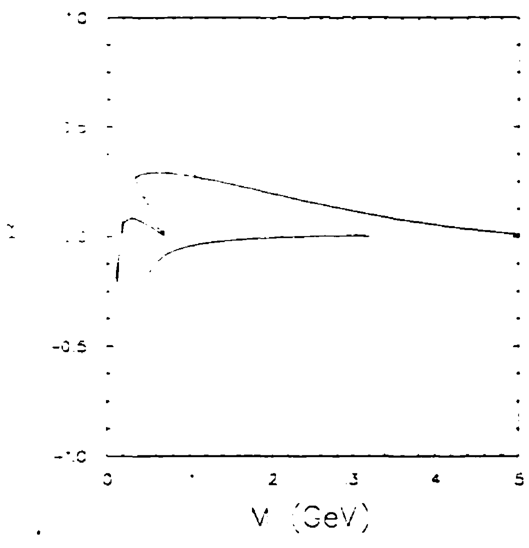

Figure 4.7: The polar anisotropy coefficient, as defined in the text, against the lepton pair invariant mass M for invariant energies of $\pi^+\pi^-$ system 0.36, 0.6 and 0.8 GeV, respectively. The solid lines represent the exact calculations; the dotted lines are for the $K^\mu(s,t)$ scheme soft-photon leading-order approximations. At invariant energy 0.36 GeV, the dashed-dot line is the result up to subleading-order with the $K^\mu(s,t)$ scheme.

dilepton spectrum may be sensitive to the quark and the pion dispersion relations in the high-temperature medium [131]. The virtual bremsstrahlung in pion-pion and quark-quark collisions should also contribute to the spectrum in this mass range. Such rates have been evaluated by Haglin et al [91] with a SPA approach. We use kinetic theory for the processes $p_1 + p_2 = p_1' + p_2' + e^+e^-$:

$$\frac{dN_{12}^{e^+e^-}}{d^4x dM^2} = g_{12}\int ds \int \frac{d^3p_1}{(2\pi)^3}\frac{d^3p_2}{(2\pi)^3} e^{-\beta(E_1+E_2)}\frac{d\sigma^{e^+e^-}}{dM^2}v_{rel} \tag{4.57}$$

where $v_{rel} = \frac{\sqrt{(p_1\cdot p_2) - m_1^2 m_2^2}}{E_1 E_2}$, $\beta = \frac{1}{kT}$, and $g_{12} = (2s_1+1)(2s_2+1)$ is the spin degeneracy. Any modification of $\frac{d\sigma^{e^+e^-}}{dM^2}$ will change the reaction rates $\frac{N_{12}^{e^+e^-}}{d^4x dM^2}$. Integrating over the momenta in Eq. (4.57),

$$\frac{dN_{12}^{e^+e^-}}{d^4x dM^2} = \frac{T^6 g_{12}}{16\pi^4}\int_{z_{min}} dz \frac{\lambda(z^2T^2, m_1^2, m_2^2)}{T^4}\kappa_1(z)\frac{d\sigma^{e^+e^-}}{dM^2}(z), \tag{4.58}$$

where $z = \frac{\sqrt{s}}{T}$, $z_{min} = (m_1 + m_2 + M)/T$, and κ_1 is a modified Bessel function.

Now we further evaluate the dilepton yields from two different scenarios of collision dynamics based on Bjorken's relativistic hydrodynamic model [126]. At first, we assume that the collisions lead to the formation of a thermalized QGP at initial time t_i, and the initial temperature T_i. Before time t_i, a very complicated initial stage might be simulated by the Parton Cascade model [132, 133, 134]. Then QGP expands and the temperature decreases until a critical temperature T_c. At T_c, QGP enters a mixed phase. We are assuming a first order phase transition. After the QGP is converted into hadronic matter, the hadron matter will cool down and reach a temperature T_f to freeze out. Another scenario is no QGP formation and the hadronic matter expands and cools, going from an initial temperature T_i to freeze-out temperature T_f.

Note $d^4x = \pi R_A^2 dytdt$, and $T(t) = T_i(t_0/t)^{\frac{1}{3}}$ based on hydrodynamic model [126], the dilepton yields can be directly written for the second scenario as

$$\frac{dN_\pi^{e^+e^-}}{dydM^2} = 3\pi R_A^2 T_i^6 t_i^2 \int_{T_f}^{T_i} \frac{dT}{T^7} \frac{dN^{e^+e^-}}{d^4xdM^2} \tag{4.59}$$

For the first scenario, there is a mixed phase contribution [130]. The dilepton yields from pion processes can be calculated as

$$\frac{dN_\pi^{e^-e^-}}{dydM^2} = 3\pi R_A^2 T_i^6 t_i^2 \int_{T_f}^{T_c} \frac{dT}{T^7} \frac{dN^{e^+e^-}}{d^4xdM^2} + \frac{\pi R_A^2}{2} (\frac{T_i}{T_c})^6 t_i^2 r(r-1) \frac{dN^{e^+e^-}}{d^4xdM^2}. \tag{4.60}$$

Here r is ratio of number of degrees of freedom in QGP to hadron phase($r \approx 12$). Note that here we do not calculate yields from the quark phase. We simply seek to compare the effect of different approximations to the pion rate, in a simple dynamical model.

In Fig. 4.8(a), we present the lepton pair rates from pion virtual bremsstrahlung at temperature T=200 MeV under three different approaches. While this figure illustrates that the SPA method is a good approximation for the dilepton rate's calculations, we add that rates should perhaps not be used to test the bremsstrahlung formalism, as the integration over a range of temperatures may change cohensions based on rates. After integrating the time evolution in the Bjorken's model, the resulting invariant-mass spectra through virtual bremsstrahlung are plotted in Fig. 4.8(b). From this figure, it is clear that the SPA is finally a reasonable approach. Note if we assume that there is no phase transition, the initial temperature has to be set unreasonably high (360 MeV), in order to reproduce the yield with a QGP phase transition and initial temperature T=200 MeV. From a purely theoretical point of view, this tells us that the mixed phase has significant contribution to the dilepton spectra.

4.10 Summary

With a One-Boson-Exchange model for $\pi^+\pi^-$ interactions, we have presented results of various soft-photon approximations and also of exact calculations. Our case study shows that at relative small energy system, the SPA amplitudes $K^\mu(s,t)$ or $K^\mu(u,t)$, can be used to evaluate the differential cross section for dilepton emission. The subleading-order formula should only be applied for small energy (compared with the energies of the particles in the system) lepton pair production. This formula should improve the precision of the calculations over the leading SPA approach. For hadron-hadron bremsstrahlung, the advantage of using SPA amplitudes can be easily seen. Such amplitudes depend only on the corresponding elastic amplitude and electromagnetic constants of the participating particles.

We may extend our approach to other charged pion contributions, for example, to $\pi^+\pi^+$ and $\pi^-\pi^-$ collisions. When the exchange mesons have charge (e.g. $\pi^0\pi^+$, or $\pi^0\pi^-$ collisions). internal radiation will also contribute to the exact amplitudes. Also a more precise evaluation is possible by considering the f-meson exchange [135], for example.

Starting from our dielectron rates, we have evaluated yields based on Bjorken's hydrodynamical model. We show that the soft-photon-approximation (SPA) is in fact not a bad approach to such calculations.

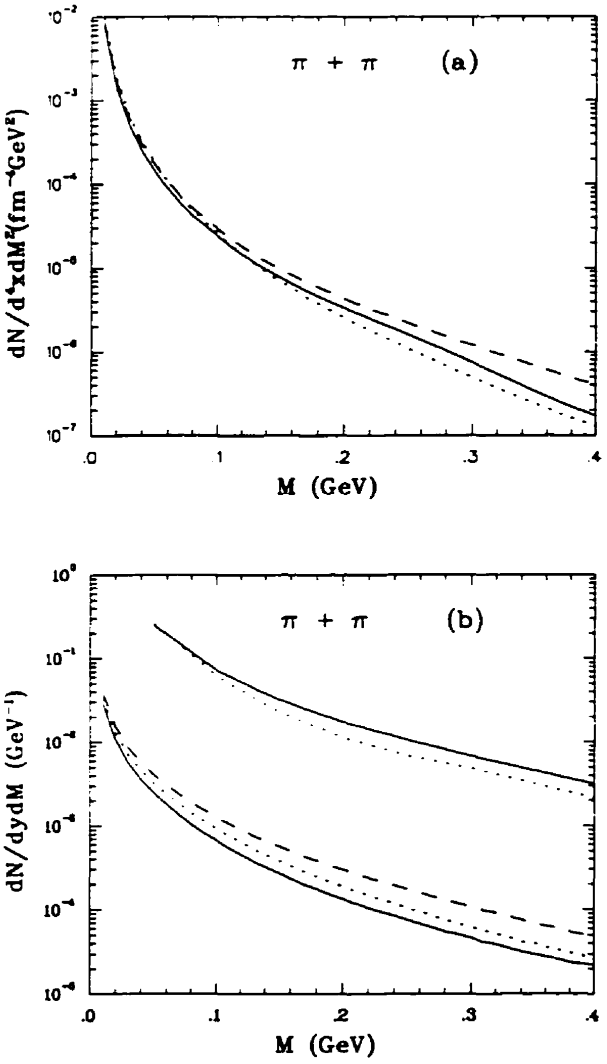

Figure 4.8: (a) The dielectron rates from pion virtual bremsstrahlung at temperature T=200 MeV under (i) solid line: the exact calculations, (ii) dotted line: only using approximation I (see text), called $K^{\mu}(s,t)$ scheme, (iii) using both approximation I and II, or called Rückl approach. (b)The dielectron yields from pion virtual bremsstrahlung. The bottom three lines are under the same three different approaches as in (a) with T_i=200 MeV, T_f = 140 MeV without QGP formation. The upper two lines are (i) solid line: T_i = 200 MeV, T_c = 160 MeV, T_f = 140 MeV with QGP formation, (ii) dotted line: T_i = 360 MeV, T_f = 140 MeV without QGP formation.

Conclusion

We have used the Boltzmann-Uehling-Uhlenbeck equation to simulate nucleus-nucleus collision dynamics at the intermediate energy regime. The transverse flow has been shown dependent on the nonlinear combinations of nucleon-nucleon cascade collisions and nuclear mean field. Concentrating on the momentum–dependent features of the one–body self–consistent nuclear mean field, we have seen that the precise functional dependence on momentum of the interaction was important. Taking two phenomenological potentials with the exact same characteristics at saturation density and zero temperature (NGBD and NMDYI), we have shown that their behavior in situations removed from equilibrium could be quite different. The relative importance of Coulomb potential has been shown dependent on the projectile kinetic energy as well as impact parameter. We have also verified the importance of angular momentum conservation on the generation of transverse momentum in high energy heavy ion collisions. Relaxing the conservation law lead to a very slight variation in the flow parameter in BUU collisions.

By performing calculations to address data on symmetric and asymmetric systems at intermediate energies, we have shown that one can indeed assess the importance of the density–dependent and momentum–dependent terms in the nuclear equation of state, separately. We have, for the first time in a comparative study, considered Streamer Chamber, Plastic Ball, DIOGENE, EOS TPC and E848H flow data and BUU calculations. We find that all the flow data we have considered in this work can be reproduced with a momentum–dependent-Yukawa interaction with a nuclear compressibility coefficient of K = 210 MeV, which is consistent with the analysis of giant monopole resonance. As BUU being a one-body theory, we have applied a simple coalescence prescription to restrict the analysis to *free* neutrons for simulating the E848H measurements. Comparison with the data reveals that the *free* neutron symmetric system data is insensitive to the nuclear compressibility K of the EOS. This is an important piece of information, as the previous calculations of flow in the collision of symmetric systems exhibit considerable structure and sensitivity to K. We have provided an explanation for such an apparent discrepancy. This involved emphasizing the role played by the nuclear composite fragments and their participation in the collective nuclear flow. Because of the large sensitivity of the composite flow to the nuclear EOS, we have shown that a quantitative connection between the composite flow and the K can be established. The tests of BUU accuracy provided by the simultaneous comparison to double and triple differential cross sections and flow data is completely unprecedented.

Then we turned to dielectron production at Bevalac energies. We have analyzed the production mechanisms in nucleus-nucleus collisions. These include delta and eta Dalitz decay, nucleon-nucleon bremsstrahlung, and pion-pion annihilation and bremsstrahlung. We have included the exact real-photon electromagnetic current and considered the effect of an asymmetric parametrization for p-n elastic differential cross section and found that these two aspects have significant effects on the dielectron yields. The relative importance of p-p and n-p bremsstrahlung has been shown dependent on the kinetic energy and p-p bremsstrahlung becomes more and more important as the energy increases. This invalidates the classic multipole argument at high energies. We have also calculated the angular distribution of the bremsstrahlung dielectrons. The angular anisotropy of the dielectron spectrum has been shown dependent on the details of the calculations. Thus some caution must be taken before such observable can be put forward as a means of distinguishing between competing lepton pair production sources. We have also examined the nuclear EOS effects on the dielectron spectrum. Comparing to the re-analyzed DLS Ca−Ca dielectron data at 1.05 GeV/nucleon, we have shown that this data can also accommodate a nuclear compressibility K=210MeV with momentum dependent feature.

Our calculation shows that the η-meson Dalitz decay dominates the dilepton spectra for the invariant masses $0.2 < M < 0.5GeV$. A precise measurement of eta production could be used to normalize the dielectron spectrum in this invariant mass region. In the intermediate mass region, the delta Dalitz decay defines the spectrum shape, and vector dominance improves the fit. The bremsstrahlung contributions are insignificant at such energy and the pion-pion annihilation determines the shape of the spectrum at high invariant masses.

Finally, based on one-boson-exchange model, we have done a full T-matrix calculation of pion-pion bremsstrahlung. The formalism has been clearly developed, and the assumptions and approximations used to recover the soft-photon approximation(SPA) formulae in the literature have also been clearly stated. The calculation results are compared to each other. We have shown that the SPA approach is in fact not a bad approximation for evaluating the bremsstrahlung contributions to the dilepton rate and yields in ultra-relativistic heavy ion collisions.

Appendix A

Nuclear Mean Field Potentials

In this appendix, we show how to adjust various sets of parameters for three different potentials used in the text. We assume that there exists a Hamiltonian giving the energy of the system in term of the phase space distribution $f(\vec{r},\vec{p})$

$$H = \int d^3\vec{r}[\int \frac{p^2}{2m} f(\vec{r},\vec{p})d^3\vec{p}] + \int d^3\vec{r}V[f] \tag{A.1}$$

here $\int \frac{p^2}{2m} f(\vec{r},\vec{p})d^3\vec{p} = E_{kin}(\rho)$ is the kinetic energy density, and $V[f]$ is the potential energy density.

Consider the single particle potential $U(\rho,\alpha)$, where ρ is the nuclear matter density $\rho = \int d^3\vec{p}f(\vec{r},\vec{p})$, and α represents the other quantities on which the potential may depend. As stressed by Bertsch and Das Gupta [8], $U(\rho,\alpha)$ is not the same as $V[f]$, but they are related

$$V(\rho,\alpha) = \int_0^\rho U(\rho',\alpha)d\rho' \tag{A.2}$$

The total energy density is then

$$\rho E_B(\rho,\alpha) = \int_0^\rho \frac{p^2(\rho')}{2m} d\rho' + V(\rho,\alpha) \tag{A.3}$$

where $p(\rho)$ is the Fermi momentum corresponding to the density ρ of particles in the system, E_B is the binding energy per particle of nuclear matter, at the equilibrium conditions for the ground state, which has the empirical value $E_B = -16$ MeV.

Now we follow the well-known procedure to calculate the pressure P of nuclear matter. If we hold the number of particles N fixed in the system, the thermodynamics gives

$$P(\rho, \alpha) = -\frac{dE_B}{dv} \tag{A.4}$$

where v is the volume of the system.

With the fact that $\frac{d}{dv} = \frac{d}{d\rho}\frac{d\rho}{dv} = -\rho^2\frac{d}{d\rho}$, we can rewrite

$$P(\rho, \alpha) = \rho^2\frac{dE_B}{d\rho} \tag{A.5}$$

At equilibrium, the pressure should vanish. Another equivalent way is to use the pressure tensor(also called the momentum current) as defined in the Appendix E of Ref. [8]

$$\Pi_{ij} = \int d^3\vec{p}\vec{p}_i(\frac{\vec{p}_j}{m} + \nabla_p^j U)f(\vec{r}, \vec{p}) + \delta_{ij}(\int d^3\vec{p}Uf(\vec{r}, \vec{p}) - V[f] \tag{A.6}$$

This expression does not assume equilibrium, and thus is general. But in equilibrium, the appendix of Ref. [34] has demonstrated that $\Pi_{ij} = \delta_{ij}P$. The disappearance of the pressure then is equivalent to the momentum current vanishing.

Another very important quantity of nuclear matter is the nuclear compressibility coefficient K, which is defined as

$$K = \frac{9k}{\rho} = 3\sum_i \frac{\partial \Pi_{ii}}{\partial \rho} \tag{A.7}$$

where k is the bulk modulus. The derivative here is taken under adiabatic conditions.

A.1 Momentum-independent Potential

The single-particle potential has the form

$$U(\rho) = A(\frac{\rho}{\rho_0}) + B(\frac{\rho}{\rho_0})^\sigma \tag{A.8}$$

and

$$V(\rho) = \frac{A}{2}\frac{\rho^2}{\rho_0} + \frac{B}{\sigma + 1}\frac{\rho^{\sigma+1}}{\rho_0^\sigma} \tag{A.9}$$

With the Fermi momentum $p_F(\rho) = (\frac{3\pi^2}{2}\rho)^{\frac{1}{3}}$, Eq. (A.3), Eq (A.5) and Eq. (A.7) yield

$$E_B = \frac{3p_F^2}{10m} + \frac{A}{2}\frac{\rho}{\rho_0} + \frac{B}{\sigma+1}\frac{\rho^\sigma}{\rho_0^\sigma} \tag{A.10}$$

$$P = \frac{p_F^2}{5m}\rho + \frac{A}{2}\frac{\rho^2}{\rho_0} + \frac{B\sigma}{\sigma+1}\frac{\rho^{\sigma+1}}{\rho_0^\sigma} \tag{A.11}$$

$$K = 9[\frac{p_F^2}{3m} + A\frac{\rho}{\rho_0} + B\sigma\frac{\rho^\sigma}{\rho_0^\sigma}] \tag{A.12}$$

The parameters (A.B.σ) of the potential should be chosen to satisfy $(i)E_B = -16$ MeV, (ii) P=0 and (iii) a specified value K, *e.g.* K=210 MeV, at the saturation density ρ_0, say $\rho_0 = 0.15 fm^{-3}$. This system of equations can be solved analytically.

A.2 GBD Momentum-dependent Potential

With the single-particle potential

$$\begin{aligned} U(\rho,\vec{p}) &= A\left(\frac{\rho(\vec{r})}{\rho_0}\right) + B\left(\frac{\rho(\vec{r})}{\rho_0}\right)^\sigma + \frac{C}{\rho_0}\int d^3p' \frac{f(\vec{r},\vec{p}')}{1+\left[\frac{\vec{p}'-<\vec{p}>}{\Lambda}\right]^2} \\ &+ \frac{C}{\rho_0}\frac{\rho}{1+\left[\frac{\vec{p}-<\vec{p}>}{\Lambda}\right]^2} \end{aligned} \tag{A.13}$$

and the potential energy density

$$V(\rho,\vec{p}) = \frac{A}{2}\frac{\rho^2(\vec{r})}{\rho_0} + \frac{B}{\sigma+1}\frac{\rho^{\sigma+1}(\vec{r})}{\rho_0^\sigma} + \frac{C\rho(\vec{r})}{\rho_0}\int d^3p \frac{f(\vec{r},\vec{p})}{1+\left[\frac{\vec{p}-<\vec{p}>}{\Lambda}\right]^2}, \tag{A.14}$$

Eq. (A.3) leads to

$$E_B = \frac{3p_F^2}{10m} + \frac{A}{2}\frac{\rho}{\rho_0} + \frac{B}{\sigma+1}\frac{\rho^\sigma}{\rho_0^\sigma} + \frac{C}{\rho_0}\int d^3p' \frac{f(\vec{r},\vec{p}')}{1+\left[\frac{\vec{p}'-<\vec{p}>}{\Lambda}\right]^2} \tag{A.15}$$

For static nuclear matter , the average value of $\vec{p}$ is zero, $<\vec{p}>= 0$. The integral thus

$$\int_0^{p_F} d^3p' \frac{f(\vec{r},\vec{p}')}{1+\left[\frac{\vec{p}'-<\vec{p}>}{\Lambda}\right]^2} = 3\rho(\frac{\Lambda}{p_F})^3[\frac{p_F}{\Lambda} - \tan^{-1}(\frac{p_F}{\Lambda})] \tag{A.16}$$

Where $f(\vec{r},\vec{p})$ is a zero temperature Fermi distribution

$$f(\vec{r},\vec{p}) = \frac{4}{h^3}\Theta(p_F - \vec{p}) \tag{A.17}$$

The factor "4" is the spin-isospin degeneracy, h is Planck's constant, and $\Theta(x)$ is the normal step function. The total energy E_B can be written as

$$E_B = \frac{3p_F^2}{10m} + \frac{A}{2}\frac{\rho}{\rho_0} + \frac{B}{\sigma+1}\frac{\rho^\sigma}{\rho_0^\sigma} + 3C\frac{\rho}{\rho_0}(\frac{\Lambda}{p_F})^3[\frac{p_F}{\Lambda} - \tan^{-1}(\frac{p_F}{\Lambda})] \tag{A.18}$$

Note

$$\frac{d}{d\rho}\int_0^{p_F} d^3p' \frac{f(\vec{r},\vec{p}')}{1+\left[\frac{\vec{p}'-<\vec{p}>}{\Lambda}\right]^2} = \frac{1}{1+(\frac{p_F}{\Lambda})^2}, \tag{A.19}$$

We readily obtain the pressure P from Eq. (A.5) and Eq. (A.18)

$$P = \frac{p_F^2}{5m}\rho + \frac{A}{2}\frac{\rho^2}{\rho_0} + \frac{B\sigma}{\sigma+1}\frac{\rho^{\sigma+1}}{\rho_0^\sigma} + C\frac{\rho^2}{\rho_0}\frac{1}{1+(\frac{p_F}{\Lambda})^2}, \tag{A.20}$$

and the nuclear compressibility coefficient K from Eq. (A.7) and Eq. (A.20)

$$\begin{aligned} K &= 9[\frac{p_F^2}{3m} + A\frac{\rho}{\rho_0} + B\sigma\frac{\rho^\sigma}{\rho_0^\sigma} + 2C\frac{\rho}{\rho_0}\frac{1}{1+(\frac{p_F}{\Lambda})^2} \\ &\quad - \frac{2C}{3}\frac{\rho}{\rho_0}(\frac{p_F}{\Lambda})^2\frac{1}{(1+(\frac{p_F}{\Lambda})^2)^2}] \end{aligned} \tag{A.21}$$

After applying the integral Eq. (A.16), the single-particle potential Eq. (A.13) for static nuclear matter at T=0 turns out to be

$$\begin{aligned} U(\rho,\vec{p}) &= A(\frac{\rho}{\rho_0}) + B(\frac{\rho}{\rho_0})^\sigma + C\frac{\rho}{\rho_0}\frac{1}{1+\frac{p^2}{\Lambda^2}} \\ &\quad + 3C\frac{\rho}{\rho_0}(\frac{\Lambda}{p_F})^3(\frac{p_F}{\Lambda} - \tan^{-1}(\frac{p_F}{\Lambda})) \end{aligned} \tag{A.22}$$

Now we evaluate the nuclear effective mass m*

$$\frac{m*}{m} = \frac{1}{1+\frac{m}{p}\nabla_{\vec{p}}U} \tag{A.23}$$

With the identities

$$\frac{\partial}{\partial\rho}\frac{1}{1+(\frac{p_F}{\Lambda})^2} = \frac{\partial p_F}{\partial\rho}\frac{\partial}{\partial p_F}\frac{1}{1+(\frac{p_F}{\Lambda})^2}, \quad \frac{\partial p_F}{\partial\rho} = \frac{1}{3}\frac{p_F}{\rho}, \tag{A.24}$$

Eq. (A.23) can be thus simplified,

$$\frac{m*}{m} = \frac{1}{1-2C\frac{\rho}{\rho_0}\frac{m}{\Lambda^2}\frac{1}{(1+(\frac{p_F}{\Lambda})^2)^2}}. \tag{A.25}$$

A.3 MDYI Momentum-dependent Potential

Substituting this type of single-particle potential

$$U(\rho(\vec{r}), \vec{p}) = A\left(\frac{\rho(\vec{r})}{\rho_0}\right) + B\left(\frac{\rho(\vec{r})}{\rho_0}\right)^{\sigma} + 2\,\frac{C}{\rho_0}\int d^3p'\,\frac{f(\vec{r},\vec{p}')}{1+\left[\frac{\vec{p}-\vec{p}'}{\Lambda}\right]^2}\,; \tag{A.26}$$

which leads to the potential energy density

$$V(\rho(\vec{r}) = \frac{A}{2}\frac{\rho^2(\vec{r})}{\rho_0} + \frac{B}{\sigma+1}\frac{\rho^{\sigma-1}(\vec{r})}{\rho_0^{\sigma}} + \frac{C}{\rho_0}\int\int d^3p\,d^3p'\frac{f(\vec{r},\vec{p})f(\vec{r},\vec{p}')}{1+\left[\frac{\vec{p}-\vec{p}'}{\Lambda}\right]^2}, \tag{A.27}$$

into Eq. (A.3), we readily obtain

$$E_B = \frac{3p_F^2}{10m} + \frac{A}{2}\frac{\rho}{\rho_0} + \frac{B}{\sigma+1}\frac{\rho^{\sigma}}{\rho_0^{\sigma}} + C\frac{\rho}{\rho_0}\int\int d^3p\,d^3p'\frac{f(\vec{r},\vec{p})f(\vec{r},\vec{p}')}{1+\left[\frac{\vec{p}-\vec{p}'}{\Lambda}\right]^2}. \tag{A.28}$$

Using the Fermi distribution Eq. (A.17), the integral

$$\begin{aligned}\int_0^{p_F}\int_0^{p_F} d^3p\,d^3p'\frac{f(\vec{r},\vec{p})f(\vec{r},\vec{p}')}{1+\left[\frac{\vec{p}-\vec{p}'}{\Lambda}\right]^2} &= 6\rho^2\frac{\Lambda^2}{p_F^2}[\frac{3}{8} - \frac{\Lambda}{2p_F}\tan^{-1}\frac{2p_F}{\Lambda} - \frac{\Lambda^2}{16p_F^2} \\ &\quad + (\frac{3}{16}\frac{\Lambda^2}{p_F^2} + \frac{1}{64}\frac{\Lambda^4}{p_F^4})\ln(1+\frac{4p_F}{\Lambda^2})]\end{aligned} \tag{A.29}$$

and

$$\begin{aligned}\int_0^{p_F} d^3p'\,\frac{f(\vec{r},\vec{p}')}{1+\left[\frac{\vec{p}-\vec{p}'}{\Lambda}\right]^2} &= \frac{\Lambda^3}{2\pi}[\frac{p_F^2+\Lambda^2-p^2}{2p\Lambda}\ln\frac{(p+p_F)^2+\Lambda^2}{(p-p_F)^2+\Lambda^2} + \frac{2p_F}{\Lambda} \\ &\quad - 2(\tan^{-1}\frac{p+p_F}{\Lambda} - \tan^{-1}\frac{p-p_F}{\Lambda})]\end{aligned} \tag{A.30}$$

With Eq. (A.5) and Eq. (A.28), the pressure can be expressed as

$$\begin{aligned}P &= \frac{p_F^2}{5m}\rho + \frac{A}{2}\frac{\rho^2}{\rho_0} + \frac{B\sigma}{\sigma+1}\frac{\rho^{\sigma+1}}{\rho_0^{\sigma}} - \frac{C}{\rho_0}\int\int d^3p\,d^3p'\frac{f(\vec{r},\vec{p})f(\vec{r},\vec{p}')}{1+\left[\frac{\vec{p}-\vec{p}'}{\Lambda}\right]^2} \\ &\quad + C\frac{\rho}{\rho_0}\frac{d}{d\rho}\int\int d^3p\,d^3p'\frac{f(\vec{r},\vec{p})f(\vec{r},\vec{p}')}{1+\left[\frac{\vec{p}-\vec{p}'}{\Lambda}\right]^2}.\end{aligned} \tag{A.31}$$

Note

$$\frac{d}{d\rho}\int\int d^3p\,d^3p'\frac{f(\vec{r},\vec{p})f(\vec{r},\vec{p}')}{1+\left[\frac{\vec{p}-\vec{p}'}{\Lambda}\right]^2} = \int_o^{p_F} d^3p\frac{f(\vec{r},\vec{p})}{1+\left[\frac{\vec{p}-\vec{p}'}{\Lambda}\right]^2} \tag{A.32}$$

we finally obtain

$$
\begin{aligned}
P &= \frac{p_F^2}{5m}\rho + \frac{A}{2}\frac{\rho^2}{\rho_0} + \frac{B\sigma}{\sigma+1}\frac{\rho^{\sigma+1}}{\rho_0^\sigma} + \frac{3C}{4}\frac{\rho^2}{\rho_0}\frac{\Lambda^2}{p_F^2}[1 + \frac{1}{6}\frac{\Lambda^2}{p_F^2} \\
&\quad - (\frac{1}{2}\frac{\Lambda^2}{p_F^2} + \frac{1}{8}\frac{\Lambda^4}{p_F^4})\ln(1 + \frac{4p_F^2}{\Lambda^2}) + (\frac{4}{3} + \frac{1}{3}\frac{\Lambda^2}{p_F^2})\frac{1}{1 + \frac{4p_F^2}{\Lambda^2}}]
\end{aligned}
\tag{A.33}
$$

The nuclear compressibility coefficient K can be calculated from Eq. (A.7) and Eq. (A.31)

$$
\begin{aligned}
K &= 9\left[\frac{p_F^2}{3m} + A\frac{\rho}{\rho_0} + B\sigma\frac{\rho^\sigma}{\rho_0^\sigma} + C\frac{\rho}{\rho_0}\frac{d^2}{d\rho^2}\int\int d^3p\, d^3p'\frac{f(\vec{r},\vec{p})f(\vec{r},\vec{p}')}{1+\left[\frac{\vec{p}-\vec{p}'}{\Lambda}\right]^2}\right] \\
&= 9\left[\frac{p_F^2}{3m} + A\frac{\rho}{\rho_0} + B\sigma\frac{\rho^\sigma}{\rho_0^\sigma} + C\frac{\rho}{\rho_0}\right].
\end{aligned}
\tag{A.34}
$$

By performing the integral Eq (A.30), we are able to express the single-particle potential for the static nuclear matter here

$$
\begin{aligned}
U(\rho(\vec{r}),\vec{p}) &= A\left(\frac{\rho(\vec{r})}{\rho_0}\right) + B\left(\frac{\rho(\vec{r})}{\rho_0}\right)^\sigma + \frac{3C}{2}\frac{\rho}{\rho_0}\frac{\Lambda^3}{p_F^3}[\frac{p_F^2+\Lambda^2-p^2}{2p\Lambda}\ln\frac{(p+p_F)^2+\Lambda^2}{(p-p_F)^2+\Lambda^2} \\
&\quad + \frac{2p_F}{\Lambda} - 2(\tan^{-1}\frac{p+p_F}{\Lambda} - \tan^{-1}\frac{p-p_F}{\Lambda})].
\end{aligned}
\tag{A.35}
$$

Then,

$$
\vec{\nabla}_{\vec{p}}U = \frac{3C}{2}\frac{\Lambda^3}{p_F^3}\frac{\rho}{\rho_0}\left[\frac{2}{\Lambda} - \frac{2p_F^2+\Lambda^2}{2p_F^2}\ln\frac{4p_F^2+\Lambda^2}{\Lambda^2}\right].
\tag{A.36}
$$

Now, we can immediately write out the effective mass m*

$$
\frac{m*}{m} = \frac{1}{1 + \frac{3mC}{2}\frac{\rho}{\rho_0}\frac{\Lambda^2}{p_F^4}\left[2 - \frac{2p_F^2+\Lambda^2}{2p_F^2}\ln\frac{4p_F^2+\Lambda^2}{\Lambda^2}\right]}
\tag{A.37}
$$

As in the GBD potential, there are five parameters $(A, B, C, \sigma, \Lambda)$ in this MDYI potential. To set these five parameters in both GBD and MDYI potentials, respectively, we need to define five equations, which should come from the empirical nuclear matter properties at the ground state. The two equations $(i)E_B = -16$ MeV, (ii) P=0 at the saturation density ρ_0 ($e.g.$ $0.15fm^{-3}$) are essential conditions. Another three equations can be chosen by specifying three quantities from $U(\rho_0,\vec{p})$, $\frac{m*}{m}$ and K. We could choose $U(\rho_0, 0) = -75MeV, U(\rho_0, \frac{p^2}{2m}$ = 300 MeV)=0, and K=200 MeV; or

$\frac{m_*}{m} = 0.67, U(\rho_0, \infty) = 30.5$ MeV and K=200 MeV. These conditions stem from static nuclear matter properties and from features of the nuclear optical potential. Then we have five non-linear equations for the five parameters. This system of equations can be solved numerically with Newton-Raphson method [136, 137], for example.

Appendix B

Derivation of Δ Dalitz Decay Width

Now we evaluate the Δ Dalitz decay width for $\Delta \to N\gamma$. Write A_μ, Ψ_N, and Ψ_Δ as the usual expansions of Dirac spinors and creation/annihilation operators

$$\begin{aligned}
A_\mu &= \sum_{\lambda=\pm1} \int \frac{d^3q}{(2\pi)^{\frac{3}{2}}}[\frac{\epsilon_\mu(q,\lambda)}{\sqrt{2q_0}}e^{iq\cdot x}a_{q\lambda} + \frac{\epsilon_\mu(q,\lambda)}{\sqrt{2q_0}}e^{-iq\cdot x}a^*_{q\lambda}] \\
\Psi_N &= \sum_{\sigma=\pm\frac{1}{2}} \int \frac{d^3p_N}{(2\pi)^{\frac{3}{2}}}[u(p_N,\sigma)e^{ip_N\cdot x}b_{p_N\sigma} + v(p_N,\sigma)e^{-ip_N\cdot x}\overline{b}^*_{p_N\sigma}] \\
\Psi^\beta_\Delta &= \sum_{\xi=\pm\frac{1}{2},\pm\frac{3}{2}} \int \frac{d^3p_\Delta}{(2\pi)^{\frac{3}{2}}}[u^\beta(p_\Delta,\xi)e^{ip_\Delta\cdot x}b_{p_\Delta\xi} + v^\beta(p_\Delta,\xi)e^{-ip_\Delta\cdot x}\overline{b}^*_{p_\Delta\xi}] \\
\overline{\Psi}^\beta_\Delta &= \sum_{\xi=\pm\frac{1}{2},\pm\frac{3}{2}} \int \frac{d^3p_\Delta}{(2\pi)^{\frac{3}{2}}}[\overline{v}^\beta(p_\Delta,\xi)e^{ip_\Delta\cdot x}\overline{b}_{p_\Delta\xi} + \overline{u}^\beta(p_\Delta,\xi)e^{-ip_\Delta\cdot x}b^*_{p_\Delta\xi}]
\end{aligned} \tag{B.1}$$

Thus, the amplitude for the process $\Delta \to N\gamma$ can be expressed as

$$\begin{aligned}
A &= <\Delta| - \mathcal{L}_{int}|\gamma N> \\
&= -e\frac{f}{(2\pi)^{\frac{9}{2}}}\frac{1}{\sqrt{2q_0}}\epsilon^\mu(q,\lambda)\overline{u}^\beta(p_\Delta,\xi)E_{\beta\mu}u(p_N,\sigma)\,.
\end{aligned} \tag{B.2}$$

One needs to average over the spins of the incoming particles and sum over the spins of the particles in the final state. We then obtain

$$\begin{aligned}
\overline{A}^2 &= \frac{1}{4}\sum_{spins} A^2 \\
&= \frac{1}{4}\frac{f^2e^2}{(2\pi)^9}\frac{1}{2q_0}Tr[\sum_\lambda \epsilon^{*\mu}(q,\lambda)\epsilon^\nu(q,\lambda)\sum_\sigma u(p_N,\sigma)\overline{u}(p_N,\sigma) \\
&\quad \gamma_0 E^+_{\beta\mu}\gamma_0\sum_\xi u^\beta(p_\Delta,\xi)\overline{u}^\alpha(p_\Delta,\xi)E_{\alpha\nu}]
\end{aligned} \tag{B.3}$$

Note the sum over the polarizations of the virtual-photon vectors and Dirac spinors

$$\begin{aligned} \sum_{\lambda} \epsilon^{*\mu}(q,\lambda)\epsilon^{\nu}(q,\lambda) &= -g^{\mu\nu} + \frac{q^{\mu}q^{\nu}}{q^2} \\ \sum_{\sigma=\pm\frac{1}{2}} u(p_N,\sigma)\overline{u}(p_N,\sigma) &= \frac{m_N + \gamma\cdot p_N}{2E_{p_N}} \,, \end{aligned} \tag{B.4}$$

and with the Rarita-Schwinger formalism for the spin $\frac{3}{2}$ particles [103]

$$\begin{aligned} \sum_{\xi=\pm\frac{3}{2},\pm\frac{1}{2}} u^{\alpha}(p_{\Delta},\xi)\overline{u}^{\beta}(p_{\Delta},\xi) &= \frac{m_{\Delta}+\gamma\cdot p_{\Delta}}{2m_{\Delta}}(g^{\alpha\beta} - \frac{2p_{\Delta}^{\alpha}p_{\Delta}^{\beta}}{3m_{\Delta}} \\ &\quad - \frac{\gamma^{\alpha}\gamma^{\beta}}{3} + \frac{p_{\Delta}^{\alpha}\gamma^{\beta} - p_{\Delta}^{\beta}\gamma^{\alpha}}{3m_{\Delta}}), \end{aligned} \tag{B.5}$$

we use Mathematica to simplify Eq.(B.3) to be

$$\begin{aligned} \overline{A}^2 &= \frac{1}{4}\frac{f^2e^2}{(2\pi)^9}\frac{1}{2E_{p_N}2q_0 2m_{\Delta}}\frac{16}{3}m_{\Delta}^3(-m_{\Delta}M^3 + 3m_N M^2 \\ &\quad + 3q_0M^2 + 3m_N q_0^2 - 5m_{\Delta}q_0^2 + 3q_0^3) \end{aligned} \tag{B.6}$$

The differential width takes the following form:

$$d\Gamma(\Delta \to N\gamma) = (2\pi)^7\overline{A}^2\delta^4(p_{\Delta} - p_N - q)d^3p_N d^3q \tag{B.7}$$

using the identities:

$$\begin{aligned} \frac{d^3p}{2E} &= \int d^4p\delta(p^2 - m^2)\Theta(p^0)\,; \\ R_2(p^2, m_1^2, m_2^2) &= \int d^4p_1 d^4p_2\delta(p_1^2 - m_1^2)\delta(p_2^2 - m_2^2)\delta^4(p - p_1 - p_2) \\ \textit{and} \quad R_2(s, m_1^2, m_2^2) &= \frac{\pi\lambda^{\frac{1}{2}}(s, m_1^2, m_2^2)}{2s}\,, \end{aligned} \tag{B.8}$$

we finally get the the total width Γ_0 of Δ into a virtual photon with invariant mass M as

$$\Gamma_0(m_{\Delta}, M^2) = \frac{1}{4\pi^2}\bar{A}^2\frac{R_2(m_{\Delta}^2, m_N^2, M^2)}{2m_{\Delta}} \tag{B.9}$$

where R_2 is the two-particle phase space integral.

Appendix C

Electromagnetic Current $(-J^2)$

For the virtual photon current J of Eq. (4.27), we evaluate the $(-J^2)$. Define

$$\tilde{\beta}_i = \hat{\beta}_i \frac{|\vec{q}|}{q_0} = \frac{\vec{p}_i}{E_i} \frac{|\vec{q}|}{q_0}, \qquad \vec{n} = \frac{\vec{q}}{|\vec{q}|} \tag{C.1}$$

Then

$$p_i \cdot q = E_i q_0 (1 - \tilde{\beta}_i \cdot \vec{n}) \tag{C.2}$$

Since $p_i^2 = m_i^2$, with the aid of the virtual photon current conservation $J^\mu q_\mu = 0$, a formal exercise will lead to

$$\begin{aligned}
-J^2 \;=\; & -\frac{Q_1^2(m_1^2 - \frac{M^2}{4})}{E_1^2 q_0^2 (1 - \tilde{\beta}_1 \cdot \vec{n} - \frac{M^2}{2E_1 q_0})^2} - \frac{Q_2^2(m_2^2 - \frac{M^2}{4})}{E_2^2 q_0^2 (1 - \tilde{\beta}_2 \cdot \vec{n} - \frac{M^2}{2E_2 q_0})^2} \\
& - \frac{Q_1'^2(m_1'^2 - \frac{M^2}{4})}{E_1'^2 q_0^2 (1 - \tilde{\beta}_1' \cdot \vec{n} + \frac{M^2}{2E_1' q_0})^2} - \frac{Q_2'^2(m_2'^2 - \frac{M^2}{4})}{E_2'^2 q_0^2 (1 - \tilde{\beta}_2' \cdot \vec{n} - \frac{M^2}{2E_2' q_0})^2} \\
& - \frac{2Q_1Q_2(1 - \frac{M^2}{4E_1E_2} - \hat{\beta}_1 \cdot \hat{\beta}_2)}{q_0^2(1 - \tilde{\beta}_1 \cdot \vec{n} - \frac{M^2}{2E_1 q_0})(1 - \tilde{\beta}_2 \cdot \vec{n} + \frac{M^2}{2E_2 q_0})} \\
& + \frac{2Q_1Q_1'(1 + \frac{M^2}{4E_1E_1'} - \hat{\beta}_1 \cdot \hat{\beta}_1')}{q_0^2(1 - \tilde{\beta}_1 \cdot \vec{n} - \frac{M^2}{2E_1 q_0})(1 - \tilde{\beta}_1' \cdot \vec{n} + \frac{M^2}{2E_1' q_0})} \\
& + \frac{2Q_1Q_2'(1 + \frac{M^2}{4E_1E_2'} - \hat{\beta}_1 \cdot \hat{\beta}_2')}{q_0^2(1 - \tilde{\beta}_1 \cdot \vec{n} - \frac{M^2}{2E_1 q_0})(1 - \tilde{\beta}_2' \cdot \vec{n} + \frac{M^2}{2E_2' q_0})} \\
& + \frac{2Q_2Q_1'(1 + \frac{M^2}{4E_2E_1'} - \hat{\beta}_2 \cdot \hat{\beta}_1')}{q_0^2(1 - \tilde{\beta}_2 \cdot \vec{n} - \frac{M^2}{2E_2 q_0})(1 - \tilde{\beta}_1' \cdot \vec{n} + \frac{M^2}{2E_1' q_0})}
\end{aligned}$$

$$
+\frac{2Q_2Q_2'(1+\frac{M^2}{4E_2E_2'}-\hat{\beta}_2\cdot\hat{\beta}_2')}{q_0^2(1-\bar{\beta}_2\cdot\vec{n}-\frac{M^2}{2E_1q_0})(1-\bar{\beta}_2'\cdot\vec{n}+\frac{M^2}{2E_2'q_0})}
-\frac{2Q_1'Q_2'(1-\frac{M^2}{4E_1'E_2'}-\hat{\beta}_1'\cdot\hat{\beta}_2')}{q_0^2(1-\bar{\beta}_1'\cdot\vec{n}-\frac{M^2}{2E_1'q_0})(1-\bar{\beta}_2'\cdot\vec{n}+\frac{M^2}{2E_2'q_0})} \qquad (C.3)
$$

We can see that no terms in Eq. (C.3) are directly proportional to $1/q$ since those terms are canceled exactly due to the charge conservation.

Since the elastic differential cross section $d\sigma^{12\to 1'2'}/dt$ only depends on the momentum transfer t, for simplicity, we take an angular average for the squared current $(-J^2)$, in Rückl's approach. Recall the two parameter Feynman integral

$$
\frac{1}{ab}=\int_0^1\frac{dz}{[az+b(1-z)]^2}, \qquad (C.4)
$$

in our case,

$$
\begin{aligned}
F(\vec{x},\vec{y}) &= \int\frac{d\Omega_q}{4\pi}\frac{1}{(1-\vec{x}\cdot\vec{n})(1-\vec{y}\cdot\vec{n})}\\
&= \int_0^1 dz\int\frac{d\Omega_q}{4\pi}\frac{1}{(1-\vec{n}\cdot[\vec{x}z+\vec{y}(1-z)])^2}\\
&= \frac{1}{2\sqrt{R}}ln\left|\frac{[\vec{x}\cdot\vec{y}-x^2-\sqrt{R}][\vec{x}\cdot\vec{y}-y^2-\sqrt{R}]}{[\vec{x}\cdot\vec{y}-x^2+\sqrt{R}][\vec{x}\cdot\vec{y}-y^2+\sqrt{R}]}\right|, \qquad (C.5)
\end{aligned}
$$

with the scalar

$$
R=(1-\vec{x}\cdot\vec{y})^2-(1-x^2)(1-y^2), \qquad (C.6)
$$

then we obtain

$$
\begin{aligned}
\int\frac{d\Omega_q}{4\pi}|-J^2| &= \frac{1}{q_0^2}\Big\{-[\lambda_1^2(Q_1^2+Q_2^2)\frac{4m_\pi^2-M^2}{s(1-\beta_1^2)}+\lambda_2^2(Q_1'^2+Q_2'^2)\frac{4m_\pi^2-M^2}{s(1-\beta_1'^2)}]\\
&-2\lambda_1^2Q_1Q_2(2-\frac{M^2}{s}-\frac{4m_\pi^2}{s})F(\vec{\beta}_1,\vec{\beta}_2)\\
&-2\lambda_2^2Q_1'Q_2'(2-\frac{M^2}{s}-\frac{4m_\pi^2}{s})F(\vec{\beta}_1',\vec{\beta}_2')\\
&+2\lambda_1\lambda_2(Q_1Q_1'+Q_2Q_2')\frac{4m_\pi^2+M^2-2t}{s}F(\vec{\beta}_1,\vec{\beta}_1')\\
&+2\lambda_1\lambda_2(Q_1Q_2'+Q_2Q_1')\frac{4m_\pi^2+M^2-2t}{s}F(\vec{\beta}_1,\vec{\beta}_2')\Big\}, \qquad (C.7)
\end{aligned}
$$

To make the formula more compact, we have introduced the variables

$$\lambda_1 = \frac{1}{1 - \frac{M^2}{\sqrt{s} q_0}}, \quad \lambda_2 = \frac{1}{1 + \frac{M^2}{\sqrt{s} q_0}}, \quad \gamma = 1 - \frac{M^2}{q_0^2}. \tag{C.8}$$

The βs are related to the dilepton invariant mass M, energy q_0 and the above definitions through

$$\begin{aligned}
&\beta_1^2 = \beta_2^2 = \lambda_1^2 \gamma (1 - \frac{4m_\pi^2}{s}), \quad \beta_1'^2 = \beta_2'^2 = \lambda_2^2 \gamma (1 - \frac{4m_\pi^2}{s}),\\
&\vec{\beta}_1 \cdot \vec{\beta}_2 = -\lambda_1^2 (1 - \frac{4m_\pi^2}{s}), \quad \vec{\beta}_1' \cdot \vec{\beta}_2' = -\lambda_2^2 (1 - \frac{4m_\pi^2}{s}),\\
&\vec{\beta}_1 \cdot \vec{\beta}_1' = -\vec{\beta}_1 \cdot \vec{\beta}_2' = \lambda_1 \lambda_2 \gamma (1 - \frac{4m_\pi^2}{s} + \frac{2t}{s})
\end{aligned} \tag{C.9}$$

Suppose we set $M = 0$. the formulas from Eq. (C.7) recovers Eq. (3.18), which is for the squared real photon current.

For the complete phase space approach, we can rewrite the current squared term $(-J^2)$ Eq. (C.3) in term of ten scalar products $p_i \cdot p_j$, which is

$$\begin{aligned}
-J^2 = & -\frac{Q_1^2(4m_\pi^2 - M^2)}{(2p_1 \cdot q - M^2)^2} - \frac{Q_2^2(4m_\pi^2 - M^2)}{(2p_2 \cdot q - M^2)^2}\\
& - \frac{Q_1'^2(4m_\pi^2 - M^2)}{(2p_1' \cdot q + M^2)^2} - \frac{Q_2'^2(4m_\pi^2 - M^2)}{(2p_2' \cdot q + M^2)^2}\\
& - \frac{2Q_1Q_2(4p_1 \cdot p_2 - M^2)}{(2p_1 \cdot q - M^2)(2p_2 \cdot q - M^2)} + \frac{2Q_1Q_1'(4p_1 \cdot p_1' + M^2)}{(2p_1 \cdot q - M^2)(2p_1' \cdot q + M^2)}\\
& + \frac{2Q_1Q_2'(4p_1 \cdot p_2' + M^2)}{(2p_1 \cdot q - M^2)(2p_2' \cdot q + M^2)} + \frac{2Q_2Q_1'(4p_2 \cdot p_1' + M^2)}{(2p_2 \cdot q - M^2)(2p_1' \cdot q + M^2)}\\
& + \frac{2Q_2Q_2'(4p_2 \cdot p_2' + M^2)}{(2p_2 \cdot q - M^2)(2p_2' \cdot q + M^2)} - \frac{2Q_1'Q_2'(4p_1' \cdot p_2' - M^2)}{(2p_1' \cdot q + M^2)(2p_2' \cdot q + M^2)}
\end{aligned} \tag{C.10}$$

In the center of mass 1+2 frame, the ten scalar products $p_i \cdot p_j$ can be expressed in term of the integral variables in Eq. (4.39). Suppose that the magnitude of the initial particle momenta $|\vec{p_1}| = |\vec{p_2}| = p = \sqrt{s/4 - m_\pi^2}$, and the energy $E_1 = E_2 = E = \sqrt{s}/2$, then

$$p_1 \cdot p_2 = E^2 + p^2,$$

$$p_1 \cdot q = E q_0 - p|\vec{q}| \cos\theta_{p_1 q},$$

$$
\begin{aligned}
&p_1 \cdot p_2' = EE_2' - p|\vec{p_2'}|(\cos\theta_{p_1q}\cos\theta_{p_2'q} + \sin\theta_{p_1q}\sin\theta_{p_2'q}\sin\phi),\\
&p_2 \cdot q = 2Eq_0 - p_1 \cdot q,\\
&p_2 \cdot p_2' = 2EE_2' - p_1 \cdot p_2',\\
&p_2' \cdot q = E_2'q_0 - |\vec{p_2'}||\vec{q}|\cos\theta_{p_2'q}\\
&p_1 \cdot p_1' = m_1^2 + p_1 \cdot p_2 - p_1 \cdot p_2' - p_1 \cdot q\\
&p_1' \cdot p_2' = p_1 \cdot p_2' + p_2 \cdot p_2' - m_2'^2 - p_2' \cdot q\\
&p_1' \cdot q = p_1 \cdot q + p_2 \cdot q - p_2' \cdot q - M^2\\
&p_2 \cdot p_1' = p_1 \cdot p_2 + m_2^2 - p_2 \cdot p_2' - p_2 \cdot q
\end{aligned}
\tag{C.11}
$$

Bibliography

[1] See, for example, Proceedings of the Twelfth, Eleventh and Tenth International Conference on Ultra-Relativistic Nucleus-Nucleus Collisions, Heidelberg, Germany, May 20-24, 1996; Monterey, California, USA, January 9-13, 1995, Nucl. Phys. **A590** (1995); and Borlänge, Sweden, June 20–24, 1993, Nucl. Phys. **A566** (1994).

[2] J.W. Harris and B. Müller, hep-ph/9602235 (1996).

[3] G.E. Brown and M. Rho, Phys. Rep. **269**, 333 (1996).

[4] See, for example, Proceedings of the NATO ASI on Hot and Dense Nuclear Matter, Bodrum, Turkey 1994, W. Greiner and H. Stöcker ed., NATO ASI Series, in press;Proceedings of the NATO ASI on the Nuclear Equation of State, Peñiscola, Spain 1989, W. Greiner and H. Stöcker ed., NATO ASI Series B: Physics Vols. 216A and 216B, and references therein.

[5] J.P. Blaizot, D. Gogny and B. Grammaticos, Nucl. Phys. **A265**, 315 (1976).

[6] J. M. Pearson, Phys. Lett. **B271**, 12 (1991).

[7] J. Zhang, S. Das Gupta, and C. Gale, Phys. Rev. **C 50**, 1617 (1994).

[8] G. F. Bertsch and S. Das Gupta, Phys. Rep. **160**, 189 (1988).

[9] J. Cugnon, T. Mizutani, and J. Vandermeulen, Nucle. Phys. **A352**, 505 (1981).

[10] W. Cassing, V. Metag, U. Mosel and K. Niita, Phys. Rep. **188**, 363 (1990).

[11] G.Q. Li, Amand Faessler and S.W. Huang, Prog. Part. Nucl. Phys. , **Vol. 31**, 159 (1993).

[12] Jim Carroll, private communications.

[13] L. Xiong, Z.G. Wu, C.M. Ko and J.Q. Wu, Nucl. Phys. **A512**, 772 (1990).

[14] Gy. Wolf, G. Batko, W. Cassing, U. Mosel, K. Niita and M. Schäfer, Nucl. Phys. **A517**, 615 (1990) .

[15] Gy. Wolf, W. Cassing, W. Ehehalt and U. Mosel, Prog. Part. Nucl. Phys.,**Vol.30**, 273 (1993) and reference therein.

[16] E. Shuryak, Phys. Lett. **B 79**, 135 (1978).

[17] A. Shor, Phys. Lett. **B 233**, 231 (1989).

[18] C. Gale and P. Lichard, Phys. Rev. **D 49**, 3338 (1994).

[19] P. Lichard, Phys. Rev **D 49**, 5812 (1994).

[20] E. Shuryak, Phys. Rep. **67**, 71 (1980).

[21] for example, see P. Lichard, Phys. Rev **D 51**, 6017 (1995), and references therein.

[22] R. Rückl, Phys. Lett. **B 64**, 39 (1976).

[23] J. Zhang, R. Tabti, C. Gale, and K. Haglin, "Another look at lepton pair production in nucleon-nucleon collisions", Int. J. Mod. Phys. E, in press.

[24] Kevin Haglin, Joseph Kapusta, and Charles Gale, Phys Lett. **B224**, 433 (1989).

[25] M. Schäfer, T. S. Biro, W. Cassing, and U. Mosel, Phys. Lett. **B221**, 1 (1989).

[26] Kevin L. Haglin, Ann. Phys. (N. Y.) **212**, 84 (1991).

[27] For a review, see H.H. Gutbrod, A.M. Poskanzer, and H.G. Ritter, Rep. Prog. Phys. **52**, 1267(1989); K.H. Kampert, Ann. Rev. Nucl. Part. Phys. **15** , 691 (1989).

[28] P. Danielewicz and G. Odyniec, Phys. Lett. **B 157**, 146 (1985) .

[29] K.G.R. Doss et al., Phys.Rev. Lett. **57**, 302 (1986) .

[30] H.A. Gustafsson et al., Phys. Rev. Lett. **52**, 1590 (1984).

[31] H. Stöcker and W. Greiner, Phys. Rep. **137**, 277 (1986), and references therein.

[32] C. Gale, G. Bertsch and S. Das Gupta, Phys. Rev. **C 35**, 1666 (1987) .

[33] J. Aichelin, A. Rosenhauer, G. Peilert, H. Stöcker and W. Greiner, Phys. Rev. Lett. 58, 1926 (1987) .

[34] C. Gale, G.M. Welke, M. Prakash, S.J. Lee and S. Das Gupta, Phys. Rev. **C 41**, 1545 (1990) .

[35] Q. Pan and P. Danielewicz, Phys. Rev. Lett. **70**, 2062 (1993); Phys. Rev. Lett. **70**, 3523 (1993).

[36] J.P. Jeukenne, A. Lejeune, and C. Mahaux, Phys. Rep. **25**, 83 (1976).

[37] G.M. Welke, M.Prakash, T.T.S. Kuo, S. Das Gupta and C. Gale, Phys. Rev. **C 38**, 2101 (1988) .

[38] V. de la Mota, F. Sébille, B. Remaud and P. Schuck, Phys. Rev. C **46**, 667 (1992).

[39] V. Koch, Proceedings of the NATO ASI on Nuclear Matter and Heavy Ion Collisions, Les Houches 1989, M. Soyeur, H. Flocard, B. Tamain, and M. Portneuf ed., NATO ASI Series B: Physics Vols. 205B.

[40] M. Elaasar, R. Madey, W. M. Zhang, J. Schambach, D. Keane, B. D. Anderson, A. R. Baldwin, J. W. Watson, G. D. Westfall, G. Krebs, H. Wieman, C. Gale, and K. Haglin, Phys. Rev. **C49**, R10 (1994).

[41] S. Wang,Y.Z. Jiang, Y.M. Liu, D. Keane, D. Beavis, S.Y. Chu, S.Y. Fung, M. Vient, C. Hartnack and H. Stöcker, Phys. Rev. **C44**, 1091 (1991).

[42] W. M. Zhang, R. Madey, J. Schambach, M. Elaasar, D. Keane, B. D. Anderson, A. R. Baldwin, J. W. Watson, G. D. Westfall, G. Krebs, H. Weiman, J. Zhang, and C. Gale, Phys. Rev. **C52**, 2643 (1995).

[43] M. Elaasar, R. Madey, W. M. Zhang, J. Schambach, D. Keane, B. D. Anderson, A. R. Baldwin, J. W. Watson, G. D. Westfall, G. Krebs, H. Wieman, C. Gale, and K. Haglin, preprint KSUCNR-003-94, McGill/94-31.

[44] M.M. Htun, R. Madey, M. Elaasar, D. Keane, B. D. Anderson, A. R. Baldwin, J. Jiang, A. Scott, Y. Shao, J. W. Watson, K. Frankel, L. Heilbronn, G. Krebs, M.A. McMahan, W. Rathbun, J. Schambach, G. D. Westfall, S. Yennello, C. Gale and J. Zhang, to be published.

[45] R.J. Lenk and V.R. Pandharipande, Phys. Rev. C **39**, 2242 1989.

[46] Jianming Zhang *et al.*, unpublished.

[47] G.M. Welke, Ph.D Thesis, SUNY at Stony Brook, (1990).

[48] L. P. Csernai, G. Fai, C. Gale, and E. Osnes, Phys. Rev. C **46**, 736 (1992).

[49] R.B. Wiringa, Phys. Rev. **C 38**, 2967 (1988) .

[50] H. Feldmeier and P. Danielewicz, Preprint MSUCL-833, 1992.

[51] M. Demoulins, Ph.D. Thesis, University Paris Sud, 1989 (unpublished);J. Gosset et al., in The Nuclear Equation of State, edited by W. Greiner and H. Stöcker, NATO ASI Series (Plenum, N.Y., 1989) Vol. 216A;M. Demoulins et al., Phys. lett. **B 241**, 479 (1990) .

[52] D. Beavis et al., Phys. Rev. **C 45**, 299 (1992) .

[53] H. Ströbele *et al.*, Phys. Rev. Lett. **49**, 1236(1982);J. J. Molitoris, H. Stöcker, and B. L. Winer, Phys. Rev. C **36**, 220(1987);D. Keane *al.*, *ibid.* **37**, 1447(1988);C. Cavata *et al.*, *ibid.* **42**, 1760(1990).

[54] D. Keane *et al.*, Proceedings of the NATO ASI on Hot and Dense Nuclear Matter, Bodrum, Turkey, W. Greiner and H. Stöcker, eds., (Plenum, NY) 1994.

[55] David E. Kahana, Declan Keane, Yang Pang, Tom Schlagel, and Shan Wang, Phys. Rev. Lett. **74**, 4404 (1995).

[56] C. Gale and S. Das Gupta, Phys. Rev. C **42**, 1577 (1990).

[57] T. J. Shlagel and V. R. Pandharipande, Phys Rev. C **44**, 1601 (1991).

[58] G. F. Bertsch, H. Kruse, and S. Das Gupta, Phys. Rev. C 29 (1984) 673.

[59] W. Bauer, G. F. Bertsch, and S. Das Gupta, Phys. Rev. Lett. **58**, 863 (1987).

[60] S. Ayik and G. Grégoire. Phys. Lett. **B212**, 269 (1988); Nucl. Phys. **A513**, 187 (1990).

[61] J. Randrup and B. Remaud, Nucl. Phys. **A514**, 339 (1990).

[62] F. Chapelle, G. F. Burgio, Ph. Chomaz, and J. Randrup. Nucl. Phys. **A540**, 227 (1992).

[63] P. Danielewicz and G. F. Bertsch, Nucl. Phys. **A353**, 712 (1991).

[64] Pawel Danielewicz and Qiubao Pan, Phys. Rev. **C46**, 2002 (1992).

[65] S. T. Butler and C. A. Pearson, Phys. Rev. **129**, 836 (1963);A. Schwartzchild and C. Zupancic, Phys. Rev. **129**, 854 (1963); J. Gosset, H. H. Gutbrod, W. G. Meyer, A. M. Poskanzer, A. Sandoval, R. Stock, and G. D. Westfall, Phys. Rev. **C16**, 629 (1977).

[66] K. G. R. Doss *et al.*, Phys. Rev. **C37**, 163 (1988).

[67] V. Koch, Bernhard Blättel, Wolfgang Cassing, Ulrich Mosel, and Klaus Weber, Phys. Lett. **B241**, 174 (1990).

[68] H. Kruse *et al.*, Phys. Rev. **C31**, 1770 (1985).

[69] P. Danielewicz *et al.*, Phys. Rev. **C38**, 120 (1988).

[70] H. Å. Gustafsson, H. H. Gutbrod, K. H. Kampert, B. W. Kolb, A. M. Poskanzer, H. G. Ritter, and H. R. Schmidt, Mod. Phys. Lett. **A3**, 1323 (1988).

[71] H. G. Baumgardt, J. U. Schott, Y. Sakamoto, E. Schopper, H. Stöcker, J. Hofmann, W. Scheid, and W. Greiner, Z. Phys. **A273**, 359 1975).

[72] H. Stöcker, A. A. Oglobin, and W. Greiner, Z. Phys. **A303**, 259 (1981).

[73] L. P. Csernai, H. Stöcker, P. R. Subramanian, G. Buchwald, G. Graebner, A. Rosenhauer, J. A. Maruhn, and W. Greiner, Phys. Rev. **C28**, 2001 (1983).

[74] L. P. Csernai, G. Fai, and J. Randrup, Phys. Lett. **B140**, 149 (1984).

[75] G. Peilert, H. Stöcker, W. Greiner, A. Rosenhauer, A. Bohnet, and J. Aichelin, Phys. Rev. **C 39**, 1402 (1989).

[76] R. Madey *et al.*, Nucl. Phys. **A553**, 779c (1993).

[77] K. G. R. Doss *al.*, Phys. Rev. Lett. **59**, 2720 (1987).

[78] See, for example, J. Gosset *et al.*, in the Proceedings of t he NATO ASI on the Nuclear Equation of State, Peñiscola, Spain 1989, W. Greiner and H. Stöcker ed., NATO ASI Series B: Physics Vols. 216A and 216B, and references therein.

[79] J. Aichelin *et al.*, Phys. Rev. Lett. **62**, 1461 (1989).

[80] D. Keane, Private Communications.

[81] W. Bauer, Phys. Rev. Lett. **61**, 2534 (1988) .

[82] T.J. Schlagel, Ph.D thesis, University of Illinois at Urbana-Champaign, 1990 (unpublished).

[83] H.A. Gustafsson et al., Mod. Phys. Lett. **A 3**, 1323 (1988) .

[84] See, for example, Proceedings of the Workshop on Dilepton Production in Relativistic Heavy Ion Collisions, March 2-4, 1994, GSI, Darmstadt, Germany; edited by H. Bokemeyer.

[85] G. Roche *et al.*, Phys.Rev.Lett. **61**, 1069 (1988);G. Roche *et al.*, Phys. Lett. **B 226**, 228 (1989);C. Naudet et al., Phys. Rev. Lett. **62**, 2652 (1989).

[86] Kevin Haglin and Charles Gale, Phys. Rev. **C 49**, 401 (1994).

[87] W.K. Wilson et al., Phys. Lett. **B 316**, 245 (1993).

[88] D. Persram, M.Sc. Thesis.

[89] L.A. Winckelmann, H. Stöcker and W. Greiner, Phys. Lett. **B 298**, 22 (1993).

[90] See, for example, J. D. Bjorken and S. D. Drell, *Relativistic Quantum Mechanics* (McGraw-Hill, New York, 1964).

[91] K. Haglin, C. Gale, and V. Emel'yanov, Phys. Rev. **D 47**, 973 (1993).

[92] V. Balek, N. Pišúova and J. Pišút, Acta Phys. Slovaca **41**, 224 (1991).

[93] E. Byckling and K. Kajantie, Particle Kinematics(Wiley, New York, 1973).

[94] C. Gale and J. Kapusta, Phys Rev. **C 40**, 2397 (1989) .

[95] P.F.Shepard, T.J.Devlin, R.E.Mischke and J.Solomon, PPAR10, Princeton-Pennsylvania Accelerator,1989; P.F.Shepard, T.J.Devlin, R.E.Mischke and J.Solomon,Phys. Rev. **D 10**, 2735 (1974); J.A.Edgington in Polarization Phenomena in Nuclear Physics, 84 (1980); M.L.Perl,J.Cox,M,J.Longo and M.N.Kreisler, Phys. Rev. **D 1**, 1857 (1970); G.Bizard et al, Nucl. Phys. **B 85**, 14 (1975); J.L.Friedes et al, Phys. Rev. Lett. **15**, 38 (1965); E.L.Miller et al, Phys. Rev. Lett. **26**, 984 (1971); J.L.Stone et al,Phys. Rev. Lett. **38**, 1315 (1977).

[96] J.F.Marshall, C.N.Brown and F.Lobkowicz,Phys. Rev. **150**, 1119 (1966); A.Konradi, Thesis, University of Rochester, 1961; D.Aeischer et al, Phys. Rev. **D 13**, 2478 (1976);

M.G.Albrow et al, Nucl. Phys. **B 23**, 445 (1970); V.M.Guzhavin et al, JETP(USSR) **47**, 1228 (1964) and translation Soviet Physics JETP **20**, 830 (1965); H.Palevsky et al, Report BNL 11360; R.C.Kammerud et al,Phys. Rev. **D 4**, 1309 (1971); I.Ambats et al,Phys. Rev. **D 9**, 1179 (1974); B.B.Brabson et al, Phys. Rev. Lett. **23**, 1306 (1969); A.R.Clyde, Thesis, UCRL-16275, Berkeley, 1966; C.M.Ankenbrandt et al,Phys. Rev. **170**, 1223 (1968).

[97] E.L. Bratkovskaya, O.V. Teryaev, and V.D. Toneev, Phys. Lett. **348 B**, 283 (1995).

[98] E.L. Bratkovskaya, M. Schäfer, W. Cassing, U. Mosel, O.V. Teryaev, and V.D. Toneev. Phys. Lett. **348 B**. 325 (1995).

[99] J.J Sakurai. Currents and Mesons (University of Chicago Press, 1969).

[100] C. Gale and J. Kapusta, Phys. Rev. **C35**, 2107 (1987).

[101] S. Huber and J. Aichelin, Nucl. Phys. **A 573**, 587 (1994).

[102] H.F. Jones and M.D. Scadron, Ann. Phys. **81**, 1 (1973) .

[103] P.A.Carruthers, Spin and Isospin in Particle Physics (Gordon and Breach press, 1971).

[104] M. Schäfer, H.C. Dönges, A. Engel and U. Mosel, Nucl. Phys. **A 575**, 429 (1994).

[105] M. Jetter and H.W. Fearing, TRIUMF preprint TRI-PP-94-90.

[106] V. Flaminio et al.. CERN-HERA 79-03 (1979); E. Chiavassa et al., Phys. Lett **B337**. 192 (1994).

[107] A.L. De Paoli, K, Niita, W. Cassing, U. Mosel and C.M. Ko, Phys. Lett. **B219**, 194 (1989).

[108] D.H. Perkins, Introduction to High Energy Physics, (Addison Wesley, 3rd ed., 1987) p134.

[109] F.D. Berg et al., Phys. Rev. Lett. **72**, 977 (1994).

[110] E. Chiavassa et al., Z. Phys. **A342**, 107 (1992); Nucl. Phys. **A538**, 121c (1992).

[111] Ye.S. Golubeva, A.S. Iljinov and I.A. Pshenichnov, Nucl. Phys. **A562**, 389 (1993).

[112] W. Cassing, G. Batko, T. Vetter and Gy. Wolf, Z. Phys. **A 340**, 51 (1991).

[113] F. Plouin, P. Fleury and C. Wilkin, Phys. Rev. Lett. **65**, 690 (1990); also Baldini et al., *Landolt – Brnstein* Vol. **12**, Springer, Berlin (1987).

[114] V. Metag, Proceedings of the VI international Conference on Nuclear Reaction Mechanisms; Varenna(edited by E. Gadidi, 1991) 683.

[115] R.J. Cence, Pion-Nucleon Scattering (Princeton University Press, Princeton, New Jersey, 1969).

[116] L.G. Landsberg, Phys. Rep. **128**, 301 (1985).

[117] C. Gale. Phys. Rev. **C 36**, 2152 (1988).

[118] J. Cleymans. K. edlich. and H. Satz. Z. Phys. **C 53**, 517 (1991).

[119] V.R. Brown and J. Franklin, Phys. Rev. **C8**, 1706 (1973).

[120] K. Nakayama, Phys. Rev. **C39**, 1475 (1989).

[121] F. de Jong, K. Nakayama, and T.-S.H. Lee, Phys. Rev. **C51**, 2334 (1995).

[122] F.E. Low, Phys. Rev. **110**, 974 (1958).

[123] C. Gale and J. Kapusta, Nucl. Phys. **B357**, 65 (1991).

[124] M.K. Liou, D. Lin and B.F. Gibson, Phys. Rev. **C47**, 973 (1993).

[125] J.F. Donoghue, C. Ramirez, and G. Valencia, Phys. Rev. **D 39**, 1947 (1989).

[126] J.D. Bjorken, Phys. Rev. **D27**, 140 (1983).

[127] V. Srinivasan *etal.*, Phys. Rev. **D12**, 681 (1976).

[128] S.D. Protopopescu *etal.*, Phys. Rev. **D7**, 1279 (1973).

[129] J.D. Bjorken and S.D. Drell, Relativistic Quantum Fields, (Mcgraw-Hill, 1965).

[130] K. Kajantie, J. Kapusta, L. Mclerran and A. Mekjian, Phys. Rev. **D34**, 2746 (1986).

[131] J. Kapusta, Phys. Lett **136B**, 201, (1984).

[132] K. Geiger and B. Müller, Nucl. Phys. **B369**, 600 (1992).

[133] K. Geiger, Phys. Rep. **258**, 237 (1995).

[134] K.J. Eskola and X.N. Wang, Phys. Rev. **D 49**, 1284 (1994).

[135] H.C. Eggers, R. Tabti, C. Gale and K. Haglin, Phys. Rev. **D 53**, 4822 (1996).

[136] J. Ortega and W. Rheinboldt, Iterative Solution of Nonlinear Equations in Several Variables, (New York, Academic Press, 1970).

[137] W.H. Press, B.F. Flannery, S.A. Teukosky and W.T. Vetterling, Numerical Recipes: The Art of Scientific Computering, (Cambridge University Press, 1986).

IMAGE EVALUATION TEST TARGET (QA-3)

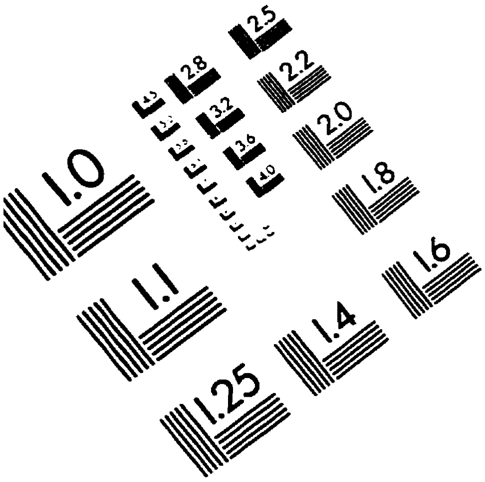

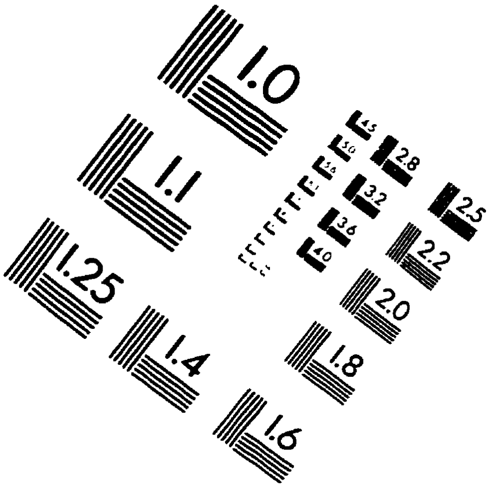

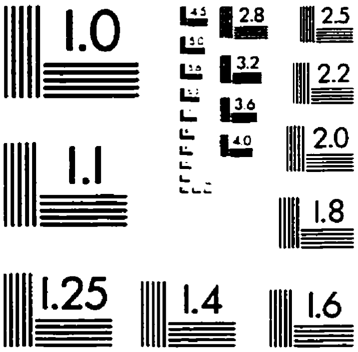

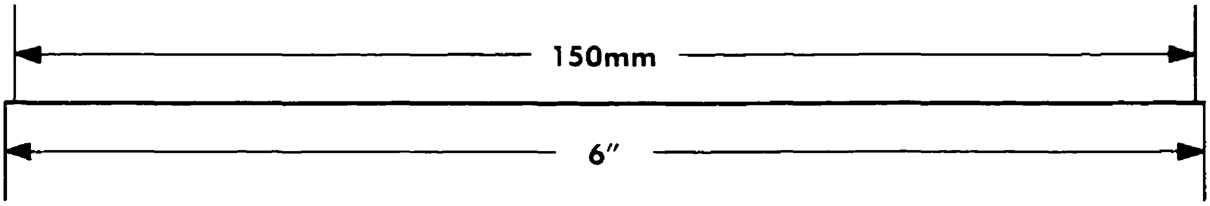

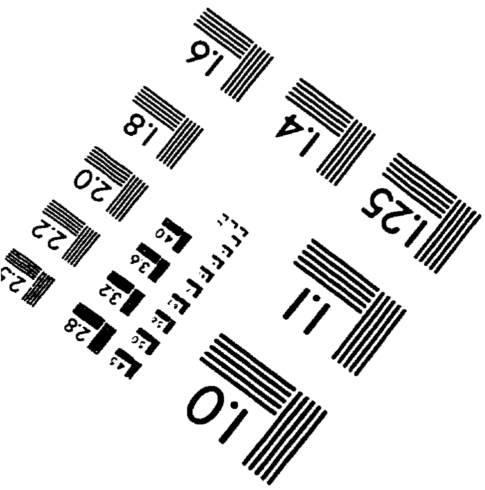

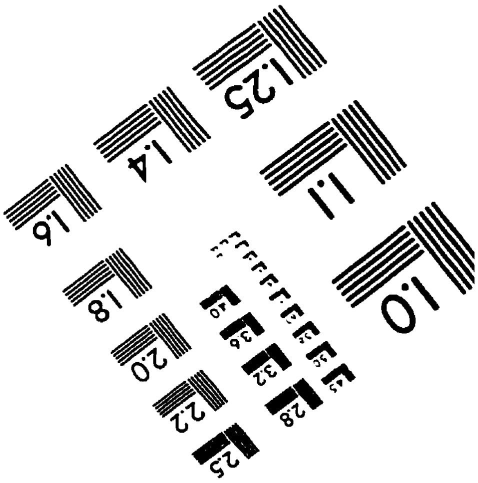

APPLIED IMAGE . Inc
1653 East Main Street
Rochester, NY 14609 USA
Phone: 716/482-0300
Fax: 716/288-5989